Integration of Physical and Chemical Approaches in a Microhand System for a Single-Cell Analysis Platform

MASAHIRO KAWAKAMI

MARCH 2026

Integration of Physical and Chemical Approaches in a Microhand System for a Single-Cell Analysis Platform

A dissertation submitted to

THE GRADUATE SCHOOL OF ENGINEERING SCIENCE

The University of Osaka

in partial fulfillment of the requirements for the degree of

DOCTOR OF PHILOSOPHY IN ENGINEERING

BY

MASAHIRO KAWAKAMI

MARCH 2026

Preface

This dissertation summarizes the research conducted under the supervision of Professor Shinji Sakai at the Division of Chemical Engineering, Graduate School of Engineering Science, The University of Osaka, from 2021 to 2026.

The objective of this dissertation study was to develop a microhand-based platform for analyzing the single-cell stiffness and behavior under large deformation. First, the influence of the end-effector shape on the measurement stability and automation of force sensor calibration were investigated. The validity of the measurement system was demonstrated through the evaluation of various cell types, drug effects, and nuclear stiffening in a Hutchinson–Gilford Progeria Syndrome model. Furthermore, the development of a fully automated system from cell detection to stiffness measurement to enhance the throughput and reproducibility is reported. Finally, a method for photocontrolling cell adhesion is proposed to enable higher-dimensional cell manipulation.

This research is expected to contribute to the elucidation of cellular mechanobiology and pathogenesis by providing a robust platform for precise single-cell mechanical characterization.

Masahiro Kawaakami

Division of Chemical Engineering

Graduate School of Engineering Science

The University of Osaka

Toyonaka, Osaka, 560-8531, Japan

Abstract

This dissertation presents the development of an integrated platform based on a microhand system to measure the whole-cell stiffness and analyze the cellular behavior under large deformations.

Chapter 1 outlines the significance of cell stiffness measurement in cell mechanobiology and limitations of existing methodologies. In particular, it emphasizes the necessity of whole-cell measurement for understanding the changes in mechanical properties associated with cellular homeostasis and pathogenesis. Furthermore, it identifies the lack of throughput and reproducibility in conventional methods as critical issues, thereby clarifying the objectives of this research.

Chapter 2 discusses the establishment of measurement precision for the microhand system and its performance validation through biological applications. First, an automated calibration method for microforce sensors was introduced to overcome the limitations of conventional manual processes, and the influence of the end-effector geometry on the measurement stability was evaluated, demonstrating the superiority of the plate-shaped end-effectors. This established system was used to quantitatively detect the stiffness reductions in cells treated with actin polymerization inhibitors and histone deacetylase inhibitors, demonstrating the capability of the system to assess the contributions of the cytoskeleton and chromatin structure. Furthermore, in the analysis of Hutchinson–Gilford progeria syndrome (HGPS) model cells, a distinct high-stiffness cell population was successfully detected, capturing disease-derived mechanical alterations. Additionally, it was demonstrated that the mechanical properties of the cytoplasm and nucleus could be independently characterized by controlling the indentation speed and depth.

Chapter 3 discusses the construction of an automated system to overcome the dependency on manipulation skills and throughput limitations inherent in the microhand system.

Conventional manual measurement imposes a significant burden on the experimenter and limits the number of cells that can be analyzed in a short timeframe. To resolve these issues, a simultaneous observation system using microscopes of different magnifications and optical tweezers was introduced, achieving full automation of the process from cell detection to grasping and stiffness measurement. Evaluation experiments confirmed that the automated system maintains a speed and measurement accuracy equivalent to that of a skilled operator. Consequently, it enables stable and efficient cell characterization, independent of the skill level of the experimenter.

Chapter 4 describes the development of fundamental technologies for the further advancement of the microhand system. Despite the effectiveness of the physical grasping mechanism discussed in the previous chapters, challenges regarding the risk of mechanical damage to cells and difficulty in holding non-adherent (floating) cells persist. To address these issues, a cell-type independent, light-responsive cell adhesion control system was developed as a chemical grasping foundation for future implementation on end-effectors. In this chapter, the testing of adhesion control based on the host–guest interaction between azobenzene-conjugated lipids and cyclodextrin-functionalized substrates by using glass substrate as a model for the end-effector surface is discussed. Experiments using human chronic myelogenous leukemia (K562) cells successfully demonstrated reversible adhesion and detachment control via light irradiation, verifying the applicability of this principle to non-adherent cells. Furthermore, the optimization of the PEG linker length revealed an inverse correlation between adhesion efficiency and adhesion force. These results establish molecular design guidelines for imparting new active grasping and releasing functions to the microhand via light.

In conclusion, the platform developed in this dissertation study provides an effective tool for single-cell analysis, facilitating the detection of subtle disease-related changes and offering

insights into the mechanical contributions of intracellular structures. The findings of this research are expected to make significant contributions to the advancement of mechanobiology and understanding of disease pathogenesis.

Table of Contents

Chapter I

General Introduction

1. Mechanical Environment Surrounding Cells

1.1 Cells and the Physical Environment

Cells are the fundamental units of biological organisms and are characterized by a highly concentrated and ordered arrangement of DNA, proteins, and organelles within a lipid bilayer. Beyond their internal complexity, cells act as active mechanical systems that acutely sense and respond to external physical environments, including elasticity [1], viscosity [2], curvature [3, 4], geometry [5, 6], and shear stress [7, 8]. The viscoelastic properties of the extracellular matrix (ECM) are critical factors determining the cell behavior [9]. For instance, vascular endothelial cells align in response to the shear stress from blood flow [7], and many cells regulate their migration modes and differentiation fates according to the ECM stiffness [10]. Thus, the cellular mechanical properties and environmental adaptation are deeply correlated; a disruption of this balance contributes to pathogenesis in conditions such as tumorigenesis and multi-organ fibrosis [11]. Therefore, a quantitative understanding of the cellular mechanical properties is vital not only for elucidating biological phenomena but also for medical applications.

1.2 Structural Support: Cytoskeleton and Focal Adhesions

The cytoskeleton is the primary structure responsible for sensing external forces, maintaining cell shape, and generating force [12, 13]. Mechanical information from the ECM is transmitted via integrins, which are receptors on the cell membrane, to focal adhesions, and subsequently to the connected cytoskeleton [14].

The cytoskeleton is primarily composed of three types of filaments that coordinate to

provide mechanical support [15]. First, actin protein dynamically alters its structure through repeated polymerization and depolymerization of monomers (G-actin) into filaments (F-actin). They are responsible for forming the actin cortex beneath the cell membrane, as well as lamellipodia and filopodia during migration [16]. Furthermore, their interaction with myosin generates contractile forces, providing tension to the cell [17]. Second, microtubules act as intracellular struts that resist compressive forces, maintaining the cell morphology by forming a tensegrity structure in balance with the tension generated by actin [18]. Third, intermediate filaments, characterized by high tensile strength, provide mechanical stability to the cell and serve as cables physically linking the cytoskeleton to the nuclear membrane [19].

The dynamics of these cytoskeletal components exhibit complex rheological properties, with the physical behavior varying significantly depending on the observation time scale. At short time scales (fractions of a second to tens of seconds), the cells behave primarily as elastic materials; however, at time scales exceeding 30 s, they demonstrate active responses, such as viscous relaxation due to cytoskeletal remodeling [20].

1.3 Mechanical Properties of the Cell Nucleus

Located deep within the cell, the nucleus possesses unique mechanical properties. Nuclear DNA exists as chromatin wrapped around histones, supporting the nucleus like a spring [21]. Although conventionally discussed as a polymer gel (viscoelastic material) [22], recent studies report that chromatin entanglement is minimal, and viscous properties may predominate depending on the measurement conditions [23, 24]. The current understanding suggests that nuclear "stiffness" is determined primarily by the nucleoplasm and chromatin condensation state (heterochromatin levels), whereas the resistance to and protection against large deformations are mediated by the nuclear lamina lining the nuclear membrane [25]. Interestingly, observations indicate a protective response wherein tensile stimuli cause a rapid reduction in heterochromatin to increase the nuclear flexibility, thereby dissipating mechanical

stress [26]. Thus, the nucleus is not merely a protected entity but a dynamic organelle that alters its physical properties in response to the environment.

1.4 Mechanotransduction and Functional Control

Changes in the extracellular environment are transmitted to the nucleus via focal adhesions and the cytoskeleton. The LINC complex, which spans the nuclear membrane to connect the cytoskeleton and nucleoskeleton, plays a central role in this transmission [27]. For example, under cyclic cell stretching, force is transmitted from actin to the LINC complex and transmembrane actin-associated nuclear (TAN) lines, causing nuclear pore complexes to accumulate and align [28]. Furthermore, this mechanical load directly regulates the chromatin structure and gene expression, facilitating environmental adaptation [29, 30].

This balance between the "mechanical environment" and "cellular stiffness/structure" is crucial for cell fate determination. In addition to endothelial alignment [31] and stem cell differentiation, reports suggest that the ability to transmit force between cells determines the outcome of cell competition [32]. In summary, cellular mechanical properties are not merely parameters for structural maintenance but play a central role in controlling biological functions, ranging from gene expression to the maintenance of homeostasis at the organismal level.

1.5 Biological Significance of Cell Stiffness

Cellular mechanical properties, such as stiffness and viscosity, are closely associated with the physiological state and pathological conditions of cells, making them potential biomarkers of significant importance. In cancer research, it is well established that cells from many solid tumors—including breast, lung, and prostate cancer—are softer than their healthy counterparts [33-35]. This cellular softening correlates strongly with increased malignancy (metastatic potential) [36, 37] and is considered to facilitate the invasion and metastasis process by allowing cells to squeeze through narrow spaces such as interstitial tissue gaps. Indeed, reports indicating that artificial stiffening of the cell membrane suppresses metastatic potential [38],

as well as the discovery of a distinct power-law scaling between cancer cell invasiveness and stiffness [33], substantiate the premise that physical properties are governing factors in cancer behavior.

Furthermore, recent studies have reported intriguing findings regarding organotropism, where a positive correlation exists between the stiffness of the cancer cell and that of the target organ for metastasis (e.g., stiffer cancer cells tend to metastasize to rigid bone, whereas softer cells tend to migrate to the softer brain) [39]. Additionally, changes in mechanical properties associated with the acquisition of drug resistance [40, 41] have been reported, suggesting promising applications in drug discovery and diagnostics.

Alterations in mechanical properties are also decisive in genetic diseases originating from defects in the cytoskeleton or nuclear structure. In Hutchinson-Gilford Progeria Syndrome (HGPS), caused by mutations in the nuclear lamin gene, the accumulation of the mutant protein progerin leads to marked stiffening of the cell nucleus [42]. This is believed to induce structural changes in chromatin and reduce nuclear responsiveness to shear and compressive stresses, ultimately leading to cellular dysfunction [43]. Conversely, in Duchenne Muscular Dystrophy (DMD), the deficiency of dystrophin, which links the cytoskeleton to the cell membrane, results in reduced mechanical strength of the cell membrane. In fact, such as erythrocytes and myocytes, derived from DMD patients, are known to be fragile against osmotic pressure and tensile stimulation, rendering them susceptible to membrane damage and cell death [44]. These findings demonstrate that maintaining the appropriate stiffness of the cell nucleus and membrane is essential for cell survival.

Mechanical properties also play a critical role in cell differentiation and aging processes. For instance, mesenchymal stem cells sense the stiffness of their scaffold material and are directed toward specific lineage differentiation according to the mechanical properties of their environment—differentiating into bone on rigid scaffolds and nerve tissue on soft scaffolds

[45-47]. In addition, a general trend toward whole-cell stiffening with increasing passage number or organismal aging has been reported [48]. However, research focusing on the ratio of nuclear to cytoplasmic stiffness suggests that aging disrupts this balance, thereby altering the efficiency of force transmission to the nucleus and attenuating mechanotransduction (mechanical response) [49]. Thus, mechanical changes associated with aging are complex and must be understood not merely as simple stiffening or softening, but as alterations in intracellular mechanical heterogeneity.

In the functional expression of immune cells, mechanical property changes associated with cytoskeletal remodeling are also a subject of discussion [50]. It is known that macrophages and dendritic cells undergo a significant increase in the cell stiffness upon activation by inflammatory stimuli to facilitate phagocytosis and antigen presentation [51]. In contrast, T cells exhibit a different behavior; naïve T cells are relatively stiff, whereas activated effector T cells are believed to remodel their cytoskeleton to enhance the deformability (flexibility), thereby improving their ability to infiltrate tissues [52].

As demonstrated by these examples, cellular mechanical properties are sensitive parameters that reflect both internal structural changes and adaptation to the external environment. Therefore, the quantification of these properties is extremely useful as a novel, label-free diagnostic and analytical tool.

2. Existing Techniques for Mechanical Characterization

Based on the differences in cellular mechanical properties discussed previously, various techniques have been developed to manipulate individual cells and measure their mechanical characteristics. Representative methods are introduced below.

Approaches to cellular mechanics can be broadly categorized into "passive measurements," which quantify the traction forces generated by the cell itself, and "active measurements," which evaluate the deformation characteristics (stiffness and viscosity) by applying external

forces. Because this study aimed to evaluate the structural properties and responsiveness to the external environment, this section focuses on the latter: active measurement and manipulation techniques. Active measurement methods cover a wide range of scales, from the molecular to the whole-cell level, with force magnitudes ranging from fN to μN. Therefore, the appropriate method must be selected based on the specific force range and biological application (Figure 1-1).

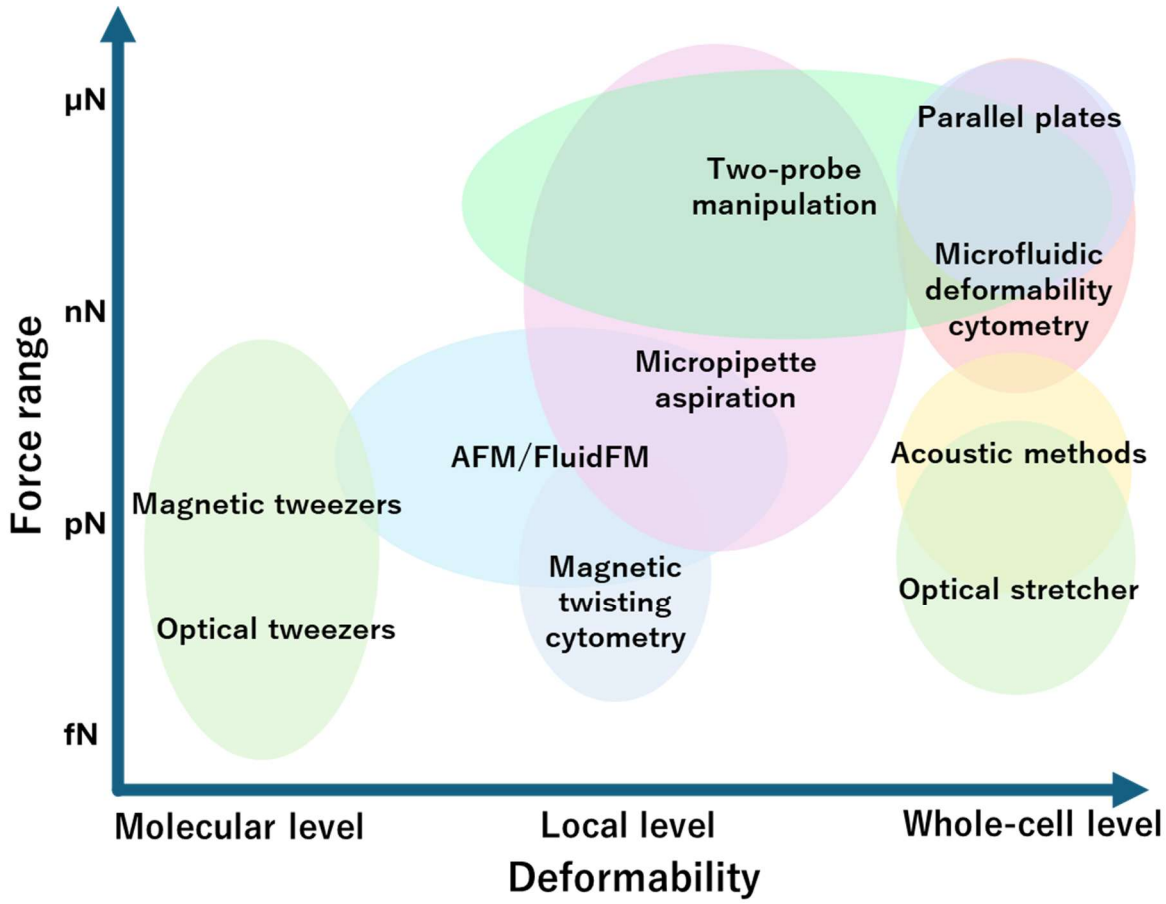

Figure 1-1. Operating ranges of representative active measurement techniques. Comparison of force ranges and spatial scales for molecular, local, and whole-cell manipulation methods.

2.1 Micropipette Aspiration

Micropipette aspiration (MPA) is a method for evaluating the mechanical properties by applying negative pressure to a cell using a glass pipette with an inner diameter of approximately 1–100 μm and analyzing its deformation behavior [53]. Owing to the simplicity

of the apparatus, it has a long history in the field of cell mechanics and is known as one of the most reliable techniques. In this method, a cell larger than the pipette diameter is aspirated via negative pressure, and properties such as elasticity and viscosity are calculated from the relationship between the aspiration length and applied pressure. A distinct feature of MPA is its ability to apply forces over a wide range (from a few piconewtons to several micronewtons), allowing for large deformations not only of the cell membrane and cytoplasm but also of deep intracellular structures like the nucleus [25, 43, 54]. In particular, MPA offers a significant advantage over other methods in its ability to evaluate the contribution of internal nuclear structures without the need for nuclear isolation [25]. Applications include the measurement of membrane tension through deformation analysis and quantification of adhesion forces by detaching substrate-adhered cells via aspiration [55, 56]. Furthermore, techniques have been established to investigate whole-cell rheological properties by capturing a cell from both sides using two pipettes to perform tensile testing [57, 58].

However, the following challenges remain. The measurement throughput is generally very low (≤10 cells/h) owing to the requirement for manual operation, making it time-consuming to acquire statistical data. Additionally, the setup and operation require a high level of technical proficiency. Furthermore, because MPA principally measures the average stiffness of the entire cell, it is unsuitable for detecting local stiffness variations, and the analysis of rapid deformation responses remains difficult.

2.2 Atomic Force Microscopy

Atomic Force Microscopy (AFM) evaluates the surface topography and mechanical properties with nanometer-scale resolution by scanning and contacting a sample surface with a fine probe (cantilever). Various tip geometries, such as colloidal, pyramidal, and flat tips, are utilized to measure the local cellular stiffness [59]. Indentation testing is the most common application in cell mechanics. The local Young's modulus of the cell can be calculated by

recording the relationship between the applied force and indentation depth and analyzing it using contact mechanics models such as the Hertz or Sneddon model [39]. The primary advantage of this method is its high spatial resolution, which enables the elucidation of the stiffness differences across distinct subcellular regions. By leveraging this high spatial and force resolution, it is possible to map the actin cortex and height profile of the adherent cells [60]. Direct mechanical characterization of the cell nucleus using needle-shaped cantilevers has also been reported [61].

Furthermore, by modifying the cantilever, AFM has been applied to measure the cell adhesion forces and perform tensile tests. Numerous studies have reported measuring the adhesion forces at the single-molecule or whole-cell level by functionalizing the cantilever tip with extracellular matrix proteins or antibodies to bind specific cell surface receptors. For instance, G. Weder et al. evaluated the cell adhesion responses to the substrate geometry and temperature (using PNIPAM) by employing fibronectin-coated probes [62, 63]. In a more advanced manipulation, Kawamura et al. successfully measured the adhesion forces using physical interlocking by processing the tip into arrow or needle shapes using a Focused Ion Beam (FIB) [64]. The same group achieved pioneering results, such as measuring the cell–cell adhesion forces by capturing cells with cap-shaped cantilevers [65] and measuring strong adhesion forces without cell rupture by reinforcing the binding via layer-by-layer deposition of fibronectin and gelatin on the cell surface [66, 67].

Despite these advances, AFM-based cell stiffness measurement faces significant challenges. First, the measurements are hindered by observational constraints. Owing to the structural design of AFM, which approaches the cell under examination from above, the direct observation of the cell from the side during indentation or tensile deformation is extremely difficult. Solutions using micromirrors have been reported [68-70], but they complicate the setup and limit the working range. Although confocal microscopy can be used for visualization,

a detailed analysis is often hindered by low z-axis resolution. Second, the throughput is very low because it requires targeting and manipulating single cells, making it unsuitable for efficient statistical data acquisition. Third, standard AFM is applicable only to substrate-adhered cells; measuring the stiffness of suspended cells requires additional methods to immobilize them on a substrate [71, 72]. Consequently, there is a demand for the development of new measurement techniques that enable tensile testing with high efficiency and detailed observation under uniform conditions.

2.3 Fluid Force Microscopy

Fluid Force Microscopy (FluidFM) is a technology that integrates microfluidics into an AFM cantilever by incorporating a microchannel and an aperture at the tip, enabling the dispensing and aspiration of liquids [73]. This integration allows for the physical immobilization of a cell using negative pressure (suction) generated by a pump, enabling the measurement of maximum adhesion force by detaching the cell [73, 74]. Conventional AFM-based adhesion measurements (e.g., using protein-functionalized cantilevers) require complex preparation and struggle to quantify the strong adhesion forces, whereas FluidFM has overcome these issues. Recently, this method was used to report dynamic changes in the cell adhesion force throughout the cell cycle [75]. Although many reports regarding the stiffness changes during the cell cycle are available, the advent of FluidFM has enabled a detailed analysis of the correlation with adhesion force, highlighting the high interest in and utility of this technique.

Beyond adhesion measurement, diverse applications utilizing the hollow tip structure are being developed. For example, it is possible to locally stain specific target cells on a substrate by dispensing the reagent from the tip [73], or to aspirate and extract cytoplasm or DNA. Such capabilities are expected to contribute significantly to fields such as single-cell sequencing (Live-seq) [76].

The greatest advantage of this method lies in its high versatility: it allows for the manipulation and measurement of targets using physical suction force without complex chemical modification processes, while maintaining the high-precision position and force control of AFM. However, as it is based on the same fundamental principles as those of AFM, it shares similar limitations, such as low measurement throughput and difficulty in observing the area directly beneath the cantilever owing to visual obstruction. Additionally, the high cost of the equipment poses a barrier to easy implementation.

2.4 Microfluidic Deformability Cytometry

Microfluidics-based techniques estimate the cellular mechanical properties (such as stiffness and viscoelasticity) by analyzing various parameters, including the deformation magnitude, shape recovery, and transit time of cells passing through a microchannel [77, 78]. The primary advantage of this approach lies in its overwhelming throughput. In comparison with single-cell measurement methods such as MPA, microfluidics enables the analysis of massive cell populations in orders of magnitude less time (processing over 100–1,000 cells per second), yielding highly reliable statistical data. Furthermore, the precise design of channel structures using the MEMS technology allows for the physical separation of cells based on differences in the mechanical properties, leading to high expectations for applications in label-free diagnosis.

Measurement principles generally involve theories based on hydrodynamic models that calculate the elastic modulus from the cell size and deformation rates [79]. Typically, high-speed cameras are employed to capture and analyze the deformation and velocity of flowing cells via image processing. Multiple approaches have been proposed regarding channel structures and deformation mechanisms. These can be broadly categorized into contact-based methods, where the cells are compressed by physical contact with the channel walls (constriction) [80], and non-contact methods, where the cells are deformed by hydrodynamic

forces originating from velocity gradients or extensional flow [81, 82]. Examples of the latter include techniques that stretch cells at the intersection of a cross-shaped channel [82].

Recently, systems utilizing electrical properties instead of image analysis have also been developed. Examples include methods that simultaneously monitor the size and stiffness via the amplitude of the voltage signals as the cells pass through electrodes within the channel [83], and high-speed analysis systems that simultaneously measure the cell deformation and membrane properties from the impedance changes by using orthogonal and parallel electric fields [84].

Thus, microfluidic devices represent one of the most promising approaches for clinical applications owing to their ability to acquire statistical data and perform cell separation efficiently. However, to deepen the understanding of the fundamental mechanobiology and cellular phenomena, several challenges must be resolved. First, because the cells pass through the channel at high speeds, it is difficult to observe minute changes or remodeling of the intracellular structures (such as the cytoskeleton and nucleus) in real-time with high resolution. Second, because these are passive measurements dependent on fluid flow, it is structurally difficult to apply active and complex mechanical stimuli, such as repeated application of force to a specific cell or stepwise change in the strain magnitude. Third, although this is an excellent approach for the statistical handling of thousands of cells, it is unsuitable for targeting, holding, and tracking a specific single cell over a long period to analyze the individual differences or temporal changes in detail.

2.5 Optical Tweezers

Optical tweezers manipulate micro-objects using the change in momentum (radiation pressure) of the focused laser light, a technique originally developed by Arthur Ashkin et al. [85]. By focusing light through an objective lens with a high numerical aperture (NA), a gradient force is generated on particles with refractive indices different from that of the

surrounding medium, such as cells or beads, allowing them to be trapped.

The primary advantage of optical tweezers lies in their ability to measure extremely minute forces, ranging from sub-piconewtons (sub-pN) to several hundred pN, owing to their very low spring constants. This high resolution makes them an invaluable tool for single-molecule measurements of molecular motors such as kinesin and myosin [86, 87], viscoelastic measurements of cell membranes [88], and manipulation of intracellular materials [89]. Furthermore, the ability to manipulate objects in a non-contact manner within closed environments, such as microfluidic channels, is a significant benefit.

However, the process of applying optical tweezers for whole-cell mechanical characterization has several limitations. The first limitation is the force limit. The maximum generatable force is typically around 100 pN, which is insufficient for deforming stiff cells that require forces in the range of nN to μN. The second limitation is the risk of phototoxicity and thermal damage. Although high-intensity lasers are required to achieve strong trapping forces, localized heating and photochemical reactions at the focal point can damage cells or alter their physiological activities [90, 91]. The third limitation is the complexity of calibration. Because the trap stiffness depends on the refractive index and shape of the object as well as the laser focal position, it is difficult to calculate the accurate forces by directly trapping heterogeneous cells. Consequently, measurements typically require the attachment of beads with known properties to the cell surface.

2.6 Optical Stretcher

The optical stretcher is a technique in which two opposing optical fibers are arranged on the sides of a microchannel [92]. By irradiating laser light from the fiber tips, forces are applied to cells, which have a different refractive index than that of the surrounding medium, via the surface stress generated by photon momentum transfer (refraction), thereby stretching the cells laterally [93]. Although difficult to parallelize to the extent possible with microfluidic devices,

this technology allows for the assessment of cell stiffness with relatively higher efficiency than that of probe-based methods.

As an advanced application, the simultaneous measurements of cellular mechanical and electrical properties has been achieved by placing electrodes around the optical fibers [94]. Furthermore, by utilizing an asymmetric optical mode to rotate trapped cells during observation, it is possible to overcome the low z-axis resolution inherent in confocal microscopy [95].

This method applies forces in the piconewton order, inducing deformations of a few percent, and evaluates the mechanical properties by comparing the responses under different conditions. However, the method has certain limitations. Although near-infrared light is used, to which biological tissues are relatively transparent, the irradiation of focused laser light raises concerns about local heating of the cell interior, which may cause cell damage or induce temperature-dependent changes in stiffness. Additionally, the small magnitude of the generated force limits its application to stiff cells or studies requiring large deformations.

2.7 Acoustic Methods

Acoustic (ultrasonic) methods have garnered significant attention in recent years owing to their ability to manipulate cells and analyze the mechanical properties in a non-invasive and non-contact manner [96]. The fundamental principle relies on the acoustic radiation force (ARF) exerted on cells within a sound field. This force depends not only on the cell size but also on the acoustic contrast factor, which is determined by the differences in density and compressibility between the cell and surrounding medium. A major feature of this approach is its label-free nature, requiring no antibodies or chemical markers.

One primary application is cell trapping and sorting using standing waves. By generating three-dimensional vortices or standing waves using ultra-high frequencies, it is possible to trap or separate cells with specific mechanical properties. Indeed, devices using this principle to separate circulating tumor cells (CTCs) from the blood of cancer patients [97], as well as to

detach and trap adherent cells to achieve three-dimensional manipulation, have been reported [98]. Systems capable of precisely manipulating organisms as large as *C. elegans* (approx. 1 mm in length) have also been developed [99].

Beyond separation, acoustic methods are applied to cell stiffness measurement. For instance, studies have successfully quantified cell compressibility and viscoelasticity by irradiating cells with Surface Acoustic Waves (SAWs) to induce deformation and analyzing the deformation magnitude and recovery behavior [100]. The relative evaluation of the cell stiffness based on the deformation induced by a single acoustic beam has also been reported [101].

Furthermore, Scanning Acoustic Microscopy (SAM) enables intracellular imaging. By irradiating cells with GHz-band ultra-short ultrasonic pulses and analyzing the reflected and transmitted waves, researchers can map the distribution of the sound speed and acoustic impedance within the cell. This allows for the non-destructive visualization of the local elastic modulus distributions and mechanical properties inside the cell, which is difficult to achieve with AFM [102].

Thus, acoustic methods are distinct from other optical and mechanical techniques, as they offer the ability to analyze the mechanical properties based on difference in the physical properties and to access internal structures with high biopermeability. They are also highly useful for manipulation owing to their non-contact nature and low cytotoxicity. However, unlike in the case of direct contact methods, significant challenges remain in the investigation of detailed changes attributed to specific structures; for example, the tracking of detailed stimulus responsiveness or cytoskeletal remodeling at a high resolution is not yet possible.

2.8 Magnetic Tweezers and Twisting Cytometry

Representative methods utilizing magnetic fields for cell stiffness measurement, such as Magnetic Tweezers and Magnetic Twisting Cytometry (MTC), evaluate the cellular mechanical properties by applying strain to the cells via magnetic beads and analyzing the resulting

deformation. Owing to the simplicity of their underlying mechanisms, these methods have been studied for a long time [103]. The primary advantage of these techniques over optical tweezers lies in their ability to apply a wide range of forces, spanning from a few piconewtons to hundreds of nanonewtons. This capability has overcome long-standing difficulties in investigating the effects of forces within living cells.

Tethering of magnetic nanoparticles (MNPs) enables the generation of minute forces. Attaching microbeads to specific molecules, such as chromatin [23] or integrins [104], allows for the investigation of local mechanical properties. Furthermore, studies evaluating the viscoelasticity of the cytoplasm through the spontaneous uptake of beads have been reported [105]. MTC, in particular, can apply a uniform strain to hundreds or thousands of cells on a substrate simultaneously using a uniform magnetic field, enabling high-efficiency acquisition of global data [104].

However, intrinsic limitations exist. Measurements require the adhesion of magnetic beads to the cell surface or their internalization via endocytosis, that is, the method is not label-free. Variations in the bead adhesion states or uptake positions cause significant heterogeneity in the measurement results. Furthermore, these methods lack operational degrees of freedom and struggle with precise measurements under complex experimental conditions. Although MTC excels at batch operations, manipulating a specific single cell three-dimensionally (e.g., grasping, transporting, or rotating) is extremely difficult owing to the spatially spreading nature of magnetic fields. Despite the theoretical possibility of three-dimensional manipulation using advanced multipolar coil systems [106], such systems are extremely complex, and achieving a balance between analytical efficiency and operability remains a challenging issue.

2.9 Two-probe Manipulation / Microplate Stretcher

Methods utilizing two glass probes (needles or plates) to sandwich and manipulate cells have been extensively employed owing to their intuitive operation and ease of observation. The

fundamental principle involves driving one probe using a piezo actuator to apply deformation, while measuring the deflection of the other flexible probe to calculate the force exerted on the cell [107, 108].

Needle-shaped end-effectors offer high flexibility in shape application. Research utilizing needles has included tensile testing of whole cells suspended via adhesives, as well as the direct manipulation of intracellular structures [107, 109, 110].

Conversely, methods using flat glass plates (Microplate Stretcher) offer the advantage of uniformly compressing or stretching the entire cell owing to their simple geometry. Techniques have also been proposed to measure the dynamic viscoelasticity (rheology) by sandwiching cells between two oscillating plates [51, 111]. The greatest advantage of this approach lies in its ability to evaluate the "whole-cell" mechanical properties, which cannot be captured by local measurement techniques such as AFM. Indeed, cases with inverse correlations between local and global cell stiffnesses have been reported [112], suggesting that separating the whole-cell deformation characteristics—including the contribution of the nucleus—is necessary to fully understand the cancer tissue invasion potential [113].

Despite providing critical insights into the cell mechanics, the widespread adoption of these two-probe methods faces challenges. The measurement throughput is extremely low (~10 cells/h) owing to the requirement for advanced manipulation skills. Additionally, the limited degrees of freedom (DoF) in operation have prevented these methods from becoming standard tools for efficient statistical data acquisition. Given that the measured cellular mechanical properties are known to vary significantly not only by cell type but also by the methodology and operator employed, there is a critical need for a system that is both versatile and capable of high-efficiency stiffness characterization [114].

3. Micro-manipulation Technology and its Challenges

3.1 Micromanipulation Technology

The development of microgrippers has been actively pursued as a technology for handling microscopic objects such as cells.

A representative mechanism involves arranging two piezoelectric elements to amplify their displacement vertically, thereby gripping a micro-object. Studies using this mechanism have reported achieving both pushing and rotational manipulation [115], as well as successfully gripping microbeads with a diameter of 14 μm by optimizing the tip geometry [116]. Although these systems enable intricate manipulation, their primary purpose is gripping and transport; they lack the functionality to quantitatively measure the stiffness of the gripped object or struggle with high-sensitivity force sensing in liquid environments.

Alternative approaches utilizing magnetic driving principles have also been proposed. For example, systems that mount a magnetically driven Magnetic Microgripper (MMG) on an AFM cantilever tip to perform manipulation with piconewton-order forces have been reported [117]. Additionally, a Microknife has been developed to grip and immobilize oocytes via magnetic control for the excision of cellular parts [118]. However, these systems face challenges in efficiency and versatile whole-cell stiffness measurement, as mentioned earlier.

Conversely, some grippers integrated with force-sensing capabilities have been reported. One such system converts the pushing force into a gripping force via a linkage mechanism, utilizing microstructures fabricated on an optical fiber tip via two-photon polymerization [119]. By employing optical interferometry, this method successfully measures the gripping force while holding a 50 μm object. However, because this mechanism relies on a compliant mechanism that closes using the reaction force against the object, "active manipulation" with independent control of the gripping force and position is not feasible. Furthermore, the force measurement resolution is approximately 0.8 μN, which is insufficient for evaluating the subtle

mechanical properties of cells.

Thus, a platform that achieves both "high DOFs and operability" and "high-throughput, precise mechanical characterization" is yet to be established using existing technologies.

3.2 Evolution and Challenges of the Microhand System

Arai et al. have been developing a microhand system that manipulates microscopic objects using a two-fingered end-effector since the 1990s [120, 121]. By integrating the MEMS technology, this system achieved high-precision force measurement with a theoretical resolution of 0.5 nN and measurement range of ~600 μN [122].

Initially, the system employed needle-shaped end-effectors equipped with force sensors to conduct indentation tests on oocytes [123] and hardness evaluations using Meyer hardness [124]. Furthermore, the group established a foundation for automation technologies, including automatic calibration via tip recognition from microscope images [125], autofocusing on manipulation targets [126, 127], and recognition of microbead gripping states [128]. Shape optimization of the end-effector has also been conducted; plate-shaped end-effectors were proposed for achieving a more stable contact during cell stiffness measurement [129], and the successful control of micro-object release in both air and liquid was achieved by vibrating the end-effector [130, 131]. By integrating these micromanipulation and image recognition technologies, the high-speed assembly (alignment into arbitrary shapes) of microbeads and cells has been realized [132, 133].

In recent years, approaches applying soft robotics have been deployed to enhance the low invasiveness of cells. For instance, end-effectors using hydrogels incorporating magnetic particles were developed to suppress vibration during actuation and reduce the risk of cell damage, thus successfully achieving microbead gripping and manipulation [134]. Additionally, gripping mechanisms utilizing the volume change (swelling/shrinking) of thermo-responsive gels (pNIPAAm) via temperature control [135], as well as magnetic soft microrobots

leveraging high operability and precision, have been developed [136].

However, challenges remain in the application of these soft material-based methods. For example, magnetic gel-based methods require AFM for calibration, and there are intrinsic difficulties in miniaturization and free shape design, rendering them unsuitable for precise manipulation at the single-cell level.

3.3 Objectives of This Study

Therefore, this study aimed to further refine the precision of cell measurement based on the microhand system developed by Arai et al., which excels in positioning accuracy and operability, and optimize it. However, applying the existing system to cell measurement requires overcoming the following unresolved issues.

First, there are challenges related to the validity of measurement and automation. Although the end-effector shapes (needle vs. plate) have been comparatively evaluated, the validity of cell stiffness measurement using plate-shaped end-effectors has not been sufficiently examined. Furthermore, automation has progressed for tasks such as assembly, but the stiffness measurement process remains largely dependent on manual operation, leading to issues related to operator-dependent variability and low reproducibility. Second, the evaluation model has a challenge. Previous studies utilized Meyer hardness, which assumes plastic deformation, as an index; however, this is intrinsically unsuitable for evaluating cells, which are viscoelastic bodies. Therefore, it is essential to introduce a new mechanical evaluation model capable of correctly describing the cellular properties. Third, there are challenges in the functionalization of the end-effector for advanced cell manipulation. Although the physical grasping mechanisms described in previous chapters are effective, they entail the risk of mechanical damage to fragile targets and face difficulties in stably holding non-adherent (floating) cells. To overcome these limitations, it is necessary to control the interfacial chemical properties to enable chemical grasping mediated by specific molecular interactions rather than relying solely on physical

force. However, current approaches often lack the reversibility and precise controllability required for dynamic manipulation. Consequently, we proposed the implementation of a light-responsive adhesion control system as a non-invasive strategy to overcome these limitations, thereby imparting active grasping and releasing capabilities to the end-effector.

Based on this background, this study constructed a platform for precise single-cell mechanical characterization by integrating appropriate evaluation models, complete automation of measurement, and chemical approaches necessary for precise end-effector fabrication.

4. Overview

The objective of this study was to advance the microhand technology into a versatile and robust platform through the systematic optimization of the end-effector geometry, automation of manipulation processes, and functionalization of contact interfaces, enabling precise whole-cell mechanical characterization under large deformation.

In Chapter II, the foundation of the microhand system for stable cell stiffness measurement is established. First, the calibration of the micro-force sensor was automated to improve the experimental efficiency. Next, the influence of the end-effector geometry on the measurement stability was investigated, demonstrating the superiority of plate-shaped end-effectors over conventional needle-shaped ones. To validate the sensitivity of the system, the mechanical properties of cells treated with cytoskeleton-modulating drugs were measured. Furthermore, the system was applied to HGPS model cells. The results revealed a distinct high-stiffness cell population in progerin-overexpressing cells, capturing disease-derived mechanical alterations. Finally, by controlling the indentation speed and depth, the mechanical properties of the cytoplasm and nucleus were separately evaluated.

In Chapter III, the automation of the microhand system to overcome the dependence on operator skill and limited throughput is discussed. Conventional manual measurement imposes

a significant burden on the experimenter. To address this, a simultaneous observation system using microscopes of different magnifications and optical tweezers was introduced to facilitate cell handling. The entire process, from cell detection to grasping and stiffness measurement, was fully automated. Evaluation experiments confirmed that the automated system maintains a speed and measurement accuracy equivalent to that of a skilled operator, enabling robust and efficient data collection.

In Chapter IV, a cell-type independent photocontrollable adhesion system to address the challenges in physical grasping, such as mechanical stress and difficulty in holding non-adherent cells, is presented. This system utilizes host–guest interactions between an azobenzene-conjugated lipid (AzoBAM) and a cyclodextrin-functionalized substrate. Using human chronic myelogenous leukemia (K562) cells as a model for non-adherent cells, adhesion and detachment were successfully demonstrated via light irradiation. Furthermore, the effect of the PEG linker length on the adhesion was quantitatively analyzed. The results revealed an inverse correlation between the adhesion efficiency and adhesion force, providing critical design guidelines for the future implementation of this chemical grasping mechanism on microhand end-effectors.

The results of this study are summarized in Chapter V General Conclusions. Suggestions for the application of this system are presented in Future Works.

Chapter II

Probing Intracellular Contributions to Cell Mechanics using a Microhand with Plate-Shaped End-Effectors

1. Introduction

This chapter presents a robust platform for whole-cell mechanical characterization using a microhand system. Specifically, it addresses the optimization of the end-effector geometry for stable grasping, automation of force sensor calibration, and validation of the biological applicability of the system using disease model cells [137].

As discussed in Chapter 1, cell mechanical properties are intrinsically linked to biological processes and pathological conditions [25, 138-140]. This link is particularly prominent in genetic disorders affecting the nuclear envelope, such as Hutchinson–Gilford progeria syndrome (HGPS). In HGPS, the accumulation of abnormal lamin A (progerin) leads to nuclear stiffening and increased mechanosensitivity[141, 142]. The investigation of such nuclear-related phenomena requires the application of significant strain to the entire cell to elicit a mechanical response reflecting the internal structural changes. Various techniques have been developed to study the cell mechanics [143, 144]. However, existing methods have limitations that prevent the realization of the objectives of this study. For instance, atomic force microscopy (AFM) necessitates cell adhesion to a substrate, hindering the measurement of suspended cells [145]. Optical tweezers, although non-invasive, operate on the piconewton scale and cannot generate sufficient force to induce the substantial deformation necessary to probe the nuclear mechanics [146, 147]. Among alternative approaches, techniques that use two probes to manipulate cells have attracted considerable attention because of their versatility and ability to induce significant deformations [148, 149]. However, conventional two-probe

systems often suffer from low degrees of freedom, which restricts the precise positioning and orientation of the end-effectors, making controlled and targeted measurements challenging.

To overcome these limitations, Arai et al. developed the microhand system [150]. The microhand is a high-resolution micromanipulator featuring a 3-DoF parallel link mechanism driven by piezoelectric actuators. This system operates two chopstick-like end-effectors integrated with microforce sensors capable of nN-order force measurement. This approach enables the direct grasping and stiffness measurement of single cells [151]. Furthermore, because the reaction force is measured directly by the integrated sensor, the direction of force application can be set arbitrarily, eliminating the need for visual monitoring of the end-effector deflection. Despite these advantages, previous iterations of the system faced practical challenges. First, replacing an end-effector necessitates replacing the sensor unit, which requires time-consuming manual recalibration. Second, earlier studies primarily employed needle-shaped end-effectors, which hindered stable whole-cell grasping and deformation, often resulting in localized damage or slippage.

Therefore, in this chapter, we first address the automation of microforce sensor calibration to improve the experimental efficiency and subsequently discuss the importance of the end-effector shape. Specifically, we compare how needle- and plate-shaped end-effectors affect the measured stiffness of human embryonic kidney (HEK293A) cells. Our results reveal that the larger contact area of the plate-shaped end-effectors enables both substantial deformation and stable measurements. We used the optimized plate-shaped end-effectors to evaluate the effects of cytoskeletal treatments on the cell stiffness and characterize the viscoelastic properties of HEK293A cells. Furthermore, we employed the system to assess the stiffness of HGPS model cells, revealing significant differences in the stiffness distribution when compared with that of healthy cells. Finally, we conducted cell indentation tests to demonstrate the capability of a separate evaluation of the mechanical properties of the cytoplasm at small indentation depths

and of the nucleus at large depths. These findings collectively demonstrate that our microhand system is a versatile and valuable platform for the detailed evaluation of whole-cell mechanical properties.

2. Materials and Methods

2.1 System Configuration

We constructed a dual-finger microhand system utilizing plate-shaped end-effectors (Figure 2-1(a,b)). The system adopts an asymmetric configuration: one finger is an active unit equipped with an actuator and a microforce sensor, whereas the opposing finger serves as a passive support without actuation or sensing capabilities (Figure 2-1(c)). The actuation mechanism employs a parallel-link structure driven by three piezoelectric elements, each integrated with two strain sensors to enable closed-loop feedback control. Together, these components facilitate precise 3-DoF manipulation. The system is controlled through sensor data acquisition and voltage regulation of the piezoelectric elements, managed by a microcontroller via an AD/DA board. The driving voltage is boosted to a 0–150 V range using a piezoelectric amplifier (HJPZ-0.15Px3, Matsusada Precision Inc., Shiga, Japan), and the signals from the strain gauges and microforce sensors are processed through a strain amplifier (MCD-16A, DPM-71A, Kyowa Electronic Instruments Co., Ltd., Tokyo, Japan). The optical setup comprises a confocal scanner unit (CSU-X1, Yokogawa Electric Corporation, Tokyo, Japan) attached to an inverted microscope (IX-73, Olympus Corporation, Tokyo, Japan). To enable simultaneous dual-channel observations, an image-splitting device (W-VIEW GEMINI, Hamamatsu Photonics K.K., Shizuoka, Japan) directs fluorescent and bright-field signals to an EM-CCD camera (Andor iXon Life 888, Oxford Instruments, Abingdon, UK). The entire microhand assembly is mounted on a motorized 3D stage (SGSP-25ACT-B0, Sigmakoki Co., Ltd., Tokyo, Japan) for coarse positioning (Figure 2-1(d)).

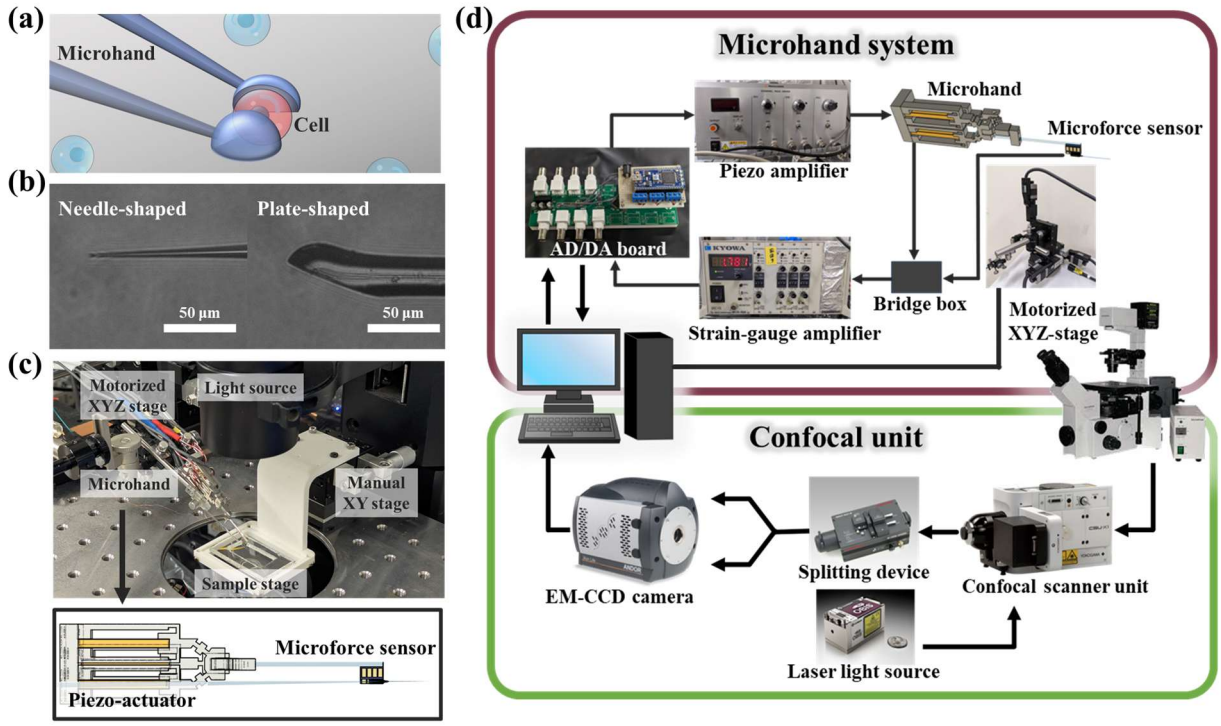

Figure 2-1. (a) Schematic representation of the cell manipulation concept. (b) Side-profile micrographs comparing the needle- and plate-shaped end-effectors. (c) Perspective view of the experimental setup alongside a detailed CAD cross-section of the microhand unit. (d) Block diagram illustrating the system configuration.

2.2 Fabrication of End-Effectors and Microforce Sensors, Actuator

A systematic protocol was employed for the fabrication of the end-effectors, as illustrated in Figure 2-2(a). Initially, needle-shaped end-effectors were generated by elongating heated glass rods (G-1000) using a puller (PC-100). These needles were processed with a microforge (MF2) to form spherical tips. Subsequently, plate-shaped end-effectors were produced by grinding both lateral surfaces of the spherical tips using a micropipette grinder (EG-402) (all equipment manufactured by Narishige Co., Ltd., Tokyo, Japan) (Figure 2-2(a), top panels).

To achieve precise 3-DOF manipulation and amplification of displacement, a parallel link mechanism was constructed using three piezo actuators (AE0203D16DF, TOKIN Corp., Miyagi, Japan). To eliminate the effect of hysteresis inherent in piezoelectric materials, a closed-loop control system was implemented using strain gauges. Specifically, two foil strain gauges (KFG-02-120-C1-11N15C2, Kyowa Electronic Instruments Co., Ltd., Tokyo, Japan)

were bonded to each piezo actuator: one aligned longitudinally to detect extension and another oriented transversely for temperature compensation.

The microforce sensors were constructed using originally designed semiconductor strain gauges bonded onto a substrate (AE-SMDPROTO127-C, Akizuki Denshi Tsusho Co., Ltd., Tokyo, Japan), followed by wire bonding using a manual wire bonder (4524A, Kulicke & Soffa, Singapore) (Figure 2-2(a), bottom panels). A tapered geometry was adopted for the strain gauge region to ensure high-sensitivity force detection (Figure 2-2(b)). To provide structural stability, the wiring connections were encased in epoxy resin. The prepared needle- or plate-shaped end-effector was then attached to the tip of the strain gauge. The assembly was coated with an adhesive and allowed to cure for 24 h. Finally, a glass rod serving as a handle was attached to facilitate the mounting of the sensor onto the manipulator.

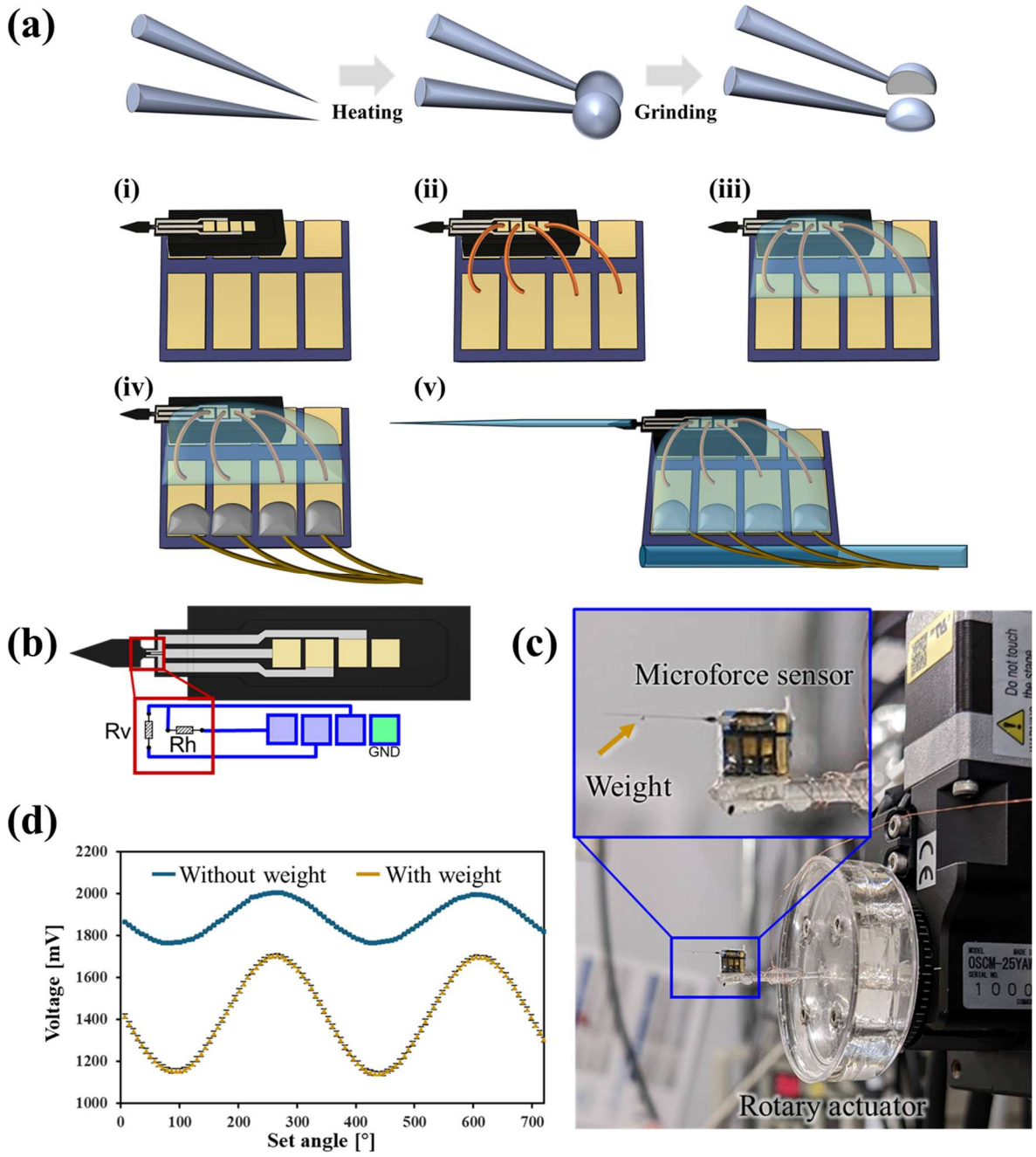

Figure 2-2. (a) *Top panels:* Schematic of the end-effector fabrication procedure. *Bottom panels:* Fabrication process of the microforce sensor. The procedure comprises: (i) mounting a semiconductor strain gauge onto the substrate; (ii) performing electrical wiring; (iii) securing the wiring area with epoxy resin; (iv) soldering wires to the connection points; and (v) bonding a glass needle to the sensor tip and glass rod handle to the substrate, followed by resin encapsulation of the exposed area. (b) Structural design of the microforce sensor and strain gauges. (c) Photograph of the assembled sensor unit. (d) Calibration plot showing the analog-to-digital (A/D) converter output values. Error bars indicate standard error (n = 50).

2.3 Automated Calibration Method for Microforce Sensors

Prior to experimentation, each microforce sensor underwent an automated calibration

procedure. The sensor was secured to a polydimethylsiloxane (SILPOT 184, Dow Toray Co., Ltd., Tokyo, Japan) fixture installed on a motorized rotary actuator (OSCM-25YAW, Sigmakoki Co., Ltd., Tokyo, Japan). To introduce a gravitational load, a chrome steel sphere (3.27×10^{-5} g) was positioned at the sensor tip (Figure 2-2(c)). Data acquisition was conducted under two distinct conditions—with and without an applied weight—to mitigate noise and correct phase discrepancies (Figure 2-2(d)).

To evaluate the calibration accuracy, we compared two processing protocols: a basic single-scan method (Automated 1) and an optimized multi-scan method (Automated 2). In the Automated 1 protocol, data were derived from a single revolution without phase compensation. In contrast, for the Automated 2 protocol (the finalized method used in this study), the sensor was rotated continuously for three complete revolutions. Post-processing involved baseline correction of the sinusoidal signals, averaging across rotations, and phase shift adjustment between the loaded and unloaded states. The revolution cycle exhibiting the minimal error was then isolated from the dataset. Using this optimal dataset, the gravitational force component acting along the sensitive axis of the sensor was computed at each angle to derive the force-to-signal conversion coefficient. The sensor resolution was subsequently determined following the methodology detailed in reference [124].

2.4 Materials

Cytochalasin D (CD), trichostatin A (TSA), L-glutamine, and streptomycin were acquired from FUJIFILM Wako Pure Chemical Co., Ltd. (Osaka, Japan). The stock solutions were prepared by dissolving CD in 1 mL of dichloromethane (1.97 mM) and TSA in 1 mL of dimethyl sulfoxide (DMSO) (1.00 mM). Lipofectamine™ 3000 was obtained from Thermo Fisher Scientific Inc. (Waltham, MA, USA). Cell culture reagents, namely, Dulbecco's modified Eagle's medium (DMEM), RPMI 1640 medium, and fetal bovine serum (FBS), were supplied by Shimadzu Diagnostics Co., Ltd. (Tokyo, Japan) and Peak Serum Inc. (Wellington,

CO, USA), respectively. Temperature-responsive culture dishes (UpCell®), capable of modulating the surface hydrophilicity at 32 °C, were procured from CellSeed Inc. (Tokyo, Japan). Fluorescent probes, specifically Nuclear Green LCS1 (ab138094) and Phalloidin-iFluor™ 680, were sourced from Abcam (Cambridge, UK), and daunorubicin was purchased from Tokyo Chemical Industry (Tokyo, Japan).

2.5 Cell Culture Condition

Six cell lines were employed in this study. Human embryonic kidney (HEK293A), mouse myoblast (C2C12), human cervical cancer (HeLa), mouse embryonic fibroblast (10T1/2), and human bone marrow-derived stromal (UE7T-13) cells were maintained in DMEM. Human chronic myelogenous leukemia (K562) cells were cultured in RPMI 1640 medium. Both media were supplemented with 10% FBS, 2 mM L-glutamine, and 100 U/mL streptomycin. All cultures were incubated at 37 °C in a humidified atmosphere containing 5% CO_2 and 95% air.

To investigate the mechanical contribution of the cytoskeleton, the cells were treated with CD at 1 or 2 μM for 30 min. Separately, the cells were incubated with TSA at 250 or 500 nM for 3 h to assess the influence of the chromatin structure.

2.6 Cell Staining Protocols

Nuclear labeling was performed using Nuclear Green LCS1. A working solution was prepared by diluting the stock (5 mM in DMSO) 1:1000 in phosphate-buffered saline (PBS), and 1 mL was applied to the culture dish for 20 min incubation. For cytoskeletal imaging, F-actin was stained following fixation. The cells were rinsed three times with PBS, fixed with paraformaldehyde for 30 min, and subsequently incubated in HEPES buffer for 10 min. After a final PBS rinse, staining was performed for 90 min using 1 μL of Phalloidin-iFluor™ 680 diluted in 1 mL of PBS containing 1% bovine serum albumin (BSA).

2.7 Overexpression of Lamin A and Progerin

Expression vectors encoding human lamin A and progerin were designated as pEGFPC1-

wt human lamin A (Lamin A OX) and pEGFPC1-human progerin (Progerin OX), respectively. These plasmids were constructed via PCR amplification, with the target genes cloned into the pEGFP-C1 vector (Clontech) to generate N-terminal EGFP fusion proteins. Transfection into the cells was achieved using Lipofectamine™ 3000 in accordance with the protocol provided by the manufacturer. For stiffness comparisons, measurements were conducted on normal HEK293A cells and Lamin A OX cells. To ensure validity, only cells displaying EGFP fluorescence were selected for the analysis. The transfection efficiencies were determined to be approximately 85% for Lamin A OX and 76% for Progerin OX.

2.8 Single-Cell Stiffness Characterization

Prior to the measurements, the end-effectors were coated with a BSA solution (1% w/v in PBS) to prevent non-specific cell adhesion. Cells grown to subconfluence were harvested through trypsinization, centrifuged at 1000 rpm for 2 min, and gently resuspended in PBS. Individual cells were then grasped with the microhand system. A compression test was performed over a duration of one second, during which both the reaction force and a video of the deformation were recorded (Figure 2-3(a)). Finally, the applied stress was calculated by integrating the force data with the contact area derived from the microscopic images.

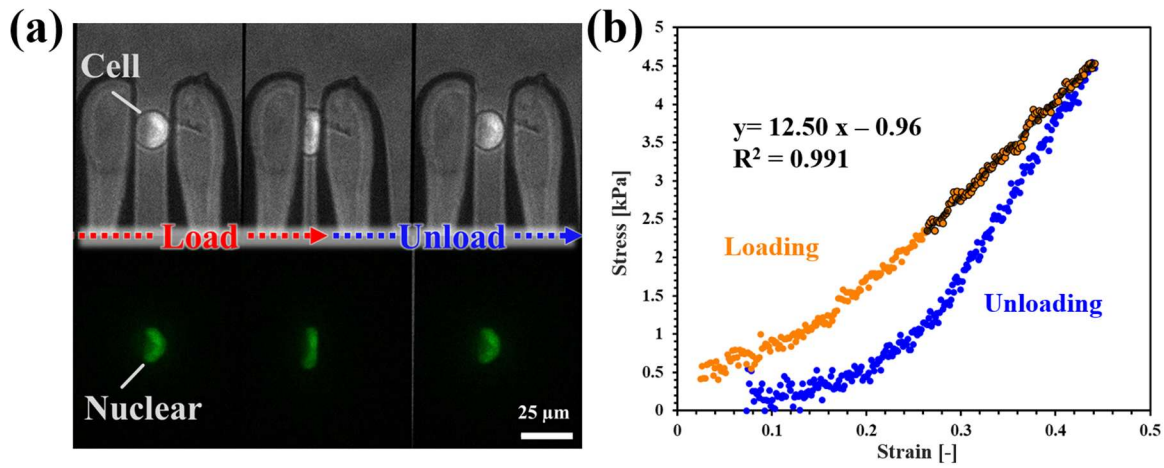

Figure 2-3. (a) Representative images of a cell indentation test conducted using the microhand system. (b) Typical stress–strain curve recorded during the indentation process (orange: loading phase; blue: unloading phase). The elastic modulus was derived from the linear slope observed in the high-strain region.

Geometric parameters, specifically contact length (D_t) and cell width (L_t), were quantified via image analysis (Figure 2-4). For calculation purposes, the contact area (S_t) was modeled as a circle.

$$S_t = \frac{\pi {D_t}^2}{4}$$

The stress σ_t was calculated based on the recorded reaction force F_t relative to the contact area:

$$\sigma_t = \frac{F_t}{S_t}$$

The strain ε_t was determined by normalizing the deformation against the initial cell width L_0:

$$\varepsilon_t = \frac{L_0 - L_t}{L_0}$$

To quantify the elastic modulus, linear regression analysis was applied to the high-strain portion of the stress–strain curve, where the data demonstrated distinct linearity (Figure 2-3(b)).

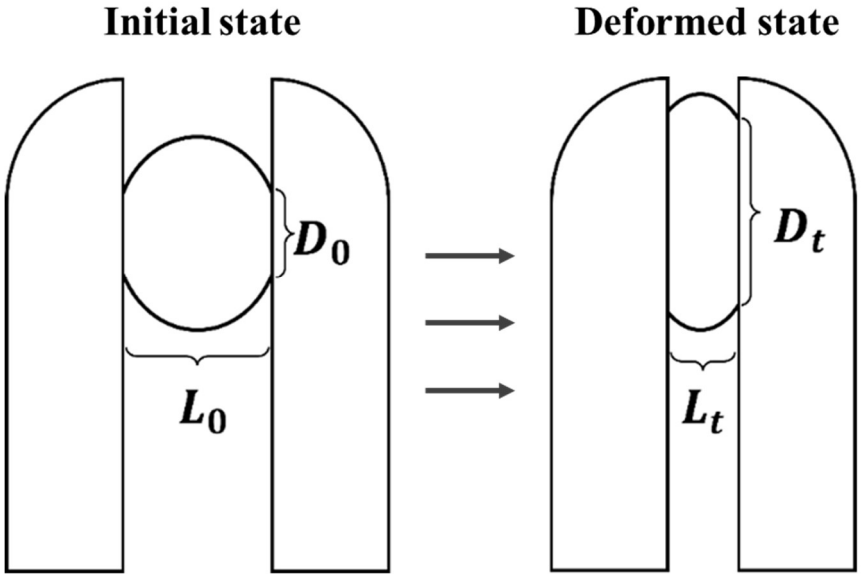

Figure 2-4. Diagrammatic representation of the geometric parameters utilized in the stress and strain computations. The illustration contrasts the initial state (left; t=0)—defined by the initial cell width (L_0) and contact length (D_0)—with the deformed state (right), characterized by the compressed width (L_t) and contact length (D_t) on the end-effector.

2.9 Statistical Analysis

Quantitative data are expressed as mean ± standard deviation (SD). Statistical comparisons were performed using Student's t-test, with statistical significance established at a *p*-value of less than 0.05.

3. Results and Discussion

3.1 Automation of Microforce Sensor Calibration

In a previous study, we presented a manual protocol for evaluating microforce sensors [124], where the A/D converter output values were recorded at 36° intervals using a manual rotary manipulator. However, this approach suffered from inherent limitations, specifically the lack of precise angular control and low data density (10 points per revolution). Notably, owing to the sinusoidal nature of the response, constant angular sampling results in a sparse distribution of data points near the zero-crossings where the force gradient is the steepest, which could compromise the calibration accuracy.

To overcome these drawbacks, we implemented an automated system utilizing a motorized rotary stage to enable high-resolution sampling (50 angular positions per revolution). We assessed two iterations of this process: a basic protocol (Automated 1) and an optimized version (Automated 2). As detailed in the methods, Automated 2 incorporates a noise-reduction strategy that averages the signals across three consecutive rotations and corrects for phase shifts between the loaded and unloaded states.

Table 2-1 presents a comparative accuracy analysis. Although Automated 1 improved the sampling density, it yielded a higher Root Mean Squared Error (RMSE of 9.49 nN) than that of the manual method (3.87 nN). In contrast, the advanced signal processing in Automated 2 successfully lowered the RMSE (5.38 nN), a value comparable to the manual technique. Notably, Automated 2 demonstrated the highest reliability by achieving the lowest maximum error (10.7 nN), a significant improvement over both the manual (25.4 nN) and Automated 1

(24.7 nN) methods (Figure 2-5(a,b)). Across nine sensors that were tested, the average force resolution was calculated as 1.88 ± 0.28 nN (n = 9). These results demonstrate that the refined automated calibration method not only streamlines the workflow but also substantially improves the reliability by minimizing detection errors.

Table 2-1. Root mean squared error (RMSE) and maximum error of the microforce sensor obtained by the manual method [124], Automated 1 (basic automation), and Automated 2 (refined automation with phase/noise correction).

	Manual Method [124]	**Automated 1**	**Automated 2**
RMSE [nN]	3.87	9.49	5.38
Maximum error [nN]	25.4	24.7	10.7

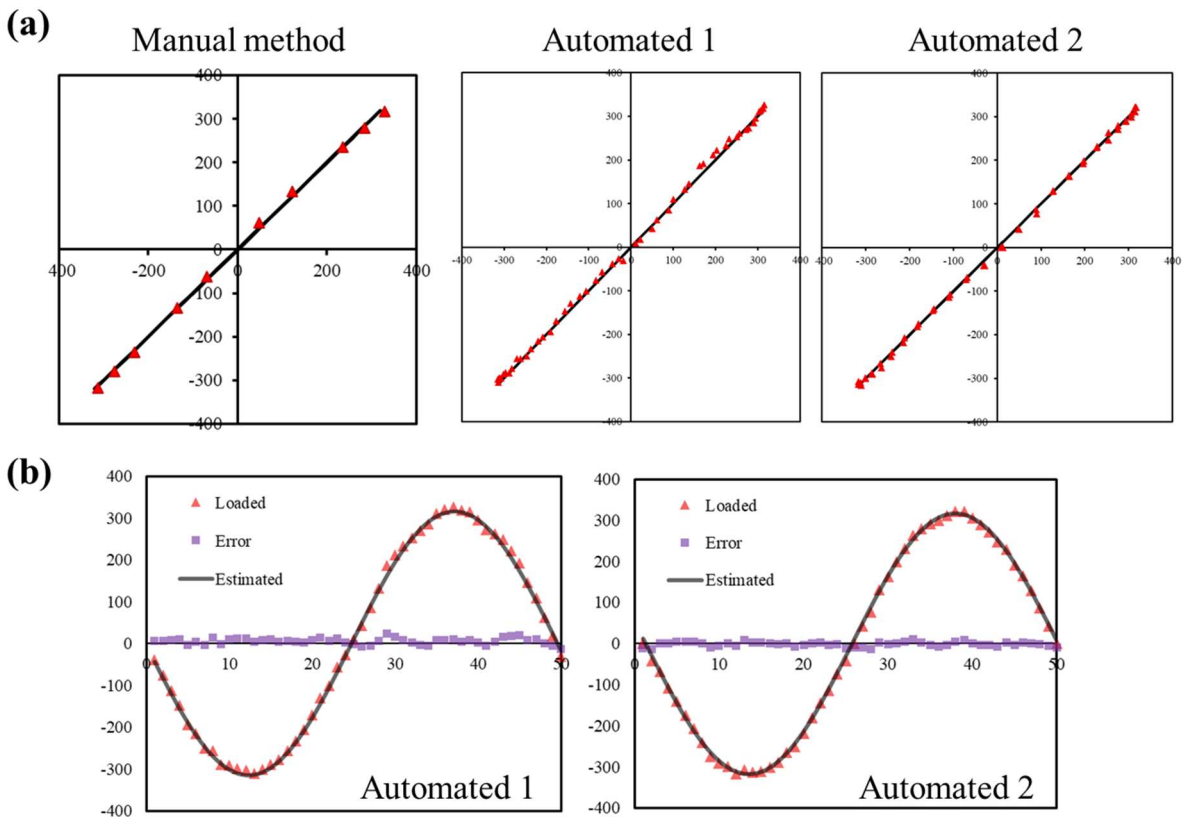

Figure 2-5. Comparison of calibration accuracy. (a) Scatter plot of predicted versus measured force values for the Manual Method, Automated 1 (basic automation), and Automated 2 (refined automation with phase/noise correction). Data alignment along the y = x line indicates the prediction accuracy. (b) Sinusoidal output curves and residual errors for Automated 1 and Automated 2. The refined processing in Automated 2 significantly reduces the error amplitude.

3.2 Impact of End-Effector Geometry on Cell Stiffness Measurement

In our previous study, we employed needle-shaped end-effectors for precision manipulation [152]. Although these tools are simple to fabricate, they suffer from inherent limitations related to the tip alignment and ability to induce substantial whole-cell deformations. To overcome these challenges, we transitioned to a plate-shaped end-effector design. Using HEK293A cells as a model, we applied large deformations to validate the efficacy of the new geometry. We hypothesized that the increased contact area of the plate-shaped tip would facilitate significant compression of the cell nucleus. This hypothesis was corroborated by fluorescence imaging, which demonstrated a distinct nuclear deformation under plate compression (Figure 2-6(a,b)). The quantitative analysis of the peak compression forces revealed a stark contrast between the two designs: the needle-shaped effector produced a wide variance in the force data, whereas the plate-shaped design yielded a much narrower and more consistent distribution (Figure 2-6(c)). Given that the nucleus is estimated to be approximately ten times stiffer than the cytoplasm (0.5–3.0 kPa) [153, 154], the variability observed in the case of the needle tips likely stems from instability when compressing the rigid nucleus. The direct observation of the stained nuclei further supported this interpretation (Figure 2-6(b)). The plate-shaped end-effector successfully deformed the nucleus in 95.0% of the trials (n = 20), whereas the success rate for the needle-shaped counterpart was only 27.3% (n = 11). These results indicate that plate-shaped end-effectors provide superior stability for indentation, leading to greater reliability of the mechanical characterization. Consequently, this geometry is better suited for investigating the mechanical contributions of the cytoskeleton and intracellular structures, particularly under large deformation regimes.

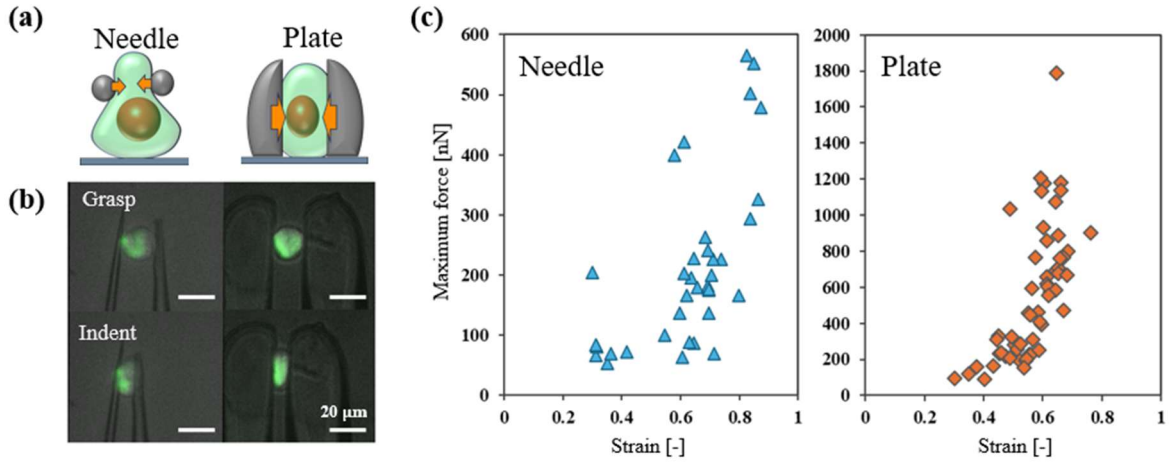

Figure 2-6. (a) Schematic and (b) corresponding fluorescence micrographs of cell compression utilizing needle-shaped (left) and plate-shaped (right) end-effectors (nuclei are stained green). (c) Comparative plot of the maximum force exerted on HEK293A cells by the needle-shaped (n = 30) and plate-shaped (n = 57) end-effectors.

3.3 Mechanical Properties of Different Cell Types

In addition to HEK293A cells, we characterized the stiffness of four additional cell lines: C2C12, HeLa, 10T1/2, UE7T-13, and K562. The quantified stiffness values were: C2C12, 6.55 ± 2.46 kPa (n = 23); HEK293, 2.85 ± 1.15 kPa (n = 57); HeLa, 5.08 ± 1.47 kPa (n = 16); 10T1/2, 6.36 ± 1.96 kPa (n = 31); UE7T-13, 5.90 ± 1.60 kPa (n = 31), and K562, 1.75 ± 0.82 kPa (n = 9) (Figure 2-7(a,c)).

Prior investigations utilizing AFM with conical probes have documented stiffness values of approximately 3.0 kPa for C2C12 cells, 1.9 kPa for HEK293 cells [155], and 2.48 kPa for HeLa cells [156]. These precedents establish a trend indicating that C2C12 cells exhibit the highest stiffness, whereas HEK293 cells are the softest among the studied cohorts. Although the absolute stiffness moduli are inherently sensitive to the experimental parameters (e.g., indenter geometry, indentation depth, instrumentation, and analytical models), the relative hierarchy of the cell stiffness observed in our study is concordant with that reported in previous literature. This consistency suggests that our microhand system reliably captures the qualitative mechanical differences across diverse cell lines.

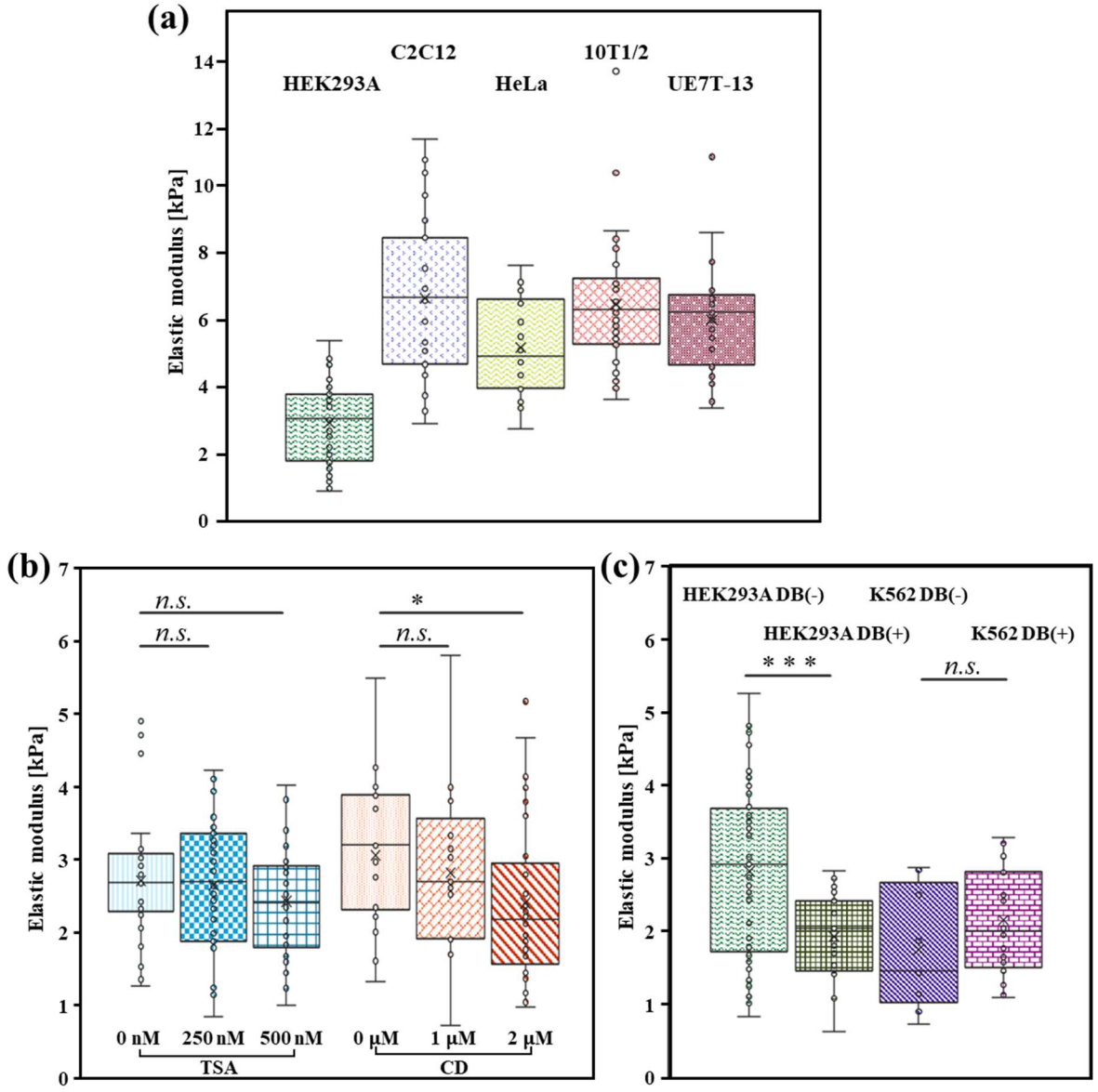

Figure 2-7. (a) Variation in single-cell stiffness across diverse cell types. (b) Reduction in cell stiffness induced by trichostatin A and cytochalasin D. (c) Differential effects of daunorubicin treatment: softening in HEK293A cells versus stiffening in K562 cells. Statistical significance was evaluated using Student's t-test (* $p < 0.05$, *** $p < 0.001$, *n.s.* = not significant). Box plot definitions: the '×' symbol denotes the mean, central line indicates the median, box boundaries represent the 25th and 75th percentiles, and whiskers extend to 1.5 times the interquartile range. Individual data points are plotted as dots.

3.4 Comparison of HEK293A Cell Stiffness under Pharmacological Treatment

To examine the contributions of specific intracellular components to the global cell mechanics, we first focused on F-actin, a primary determinant of cellular stiffness. We measured the stiffness of individual cells following treatment with cytochalasin D (CD), an actin polymerization inhibitor (Figure 2-7(b)). Because F-actin disruption is known to diminish

intracellular contractile tension and impair cell spreading [157], we anticipated a corresponding mechanical softening. Indeed, our results demonstrated a concentration-dependent reduction in the elastic moduli. The stiffness of the untreated HEK293A cells was 3.05 ± 0.99 kPa (n = 26); the treatment with 1 μM CD reduced the stiffness to 2.81 ± 1.16 kPa (n = 17), and that with 2 μM CD caused a further decline to 2.39 ± 1.10 kPa (n = 29). These data confirm that F-actin plays a pivotal role in sustaining the mechanical integrity, even in a suspended state. Although direct quantitative comparisons are complicated by variations in the experimental protocols, the qualitative trend of softening aligns well with that mentioned in prior studies using 5 μM CD [72].

Next, we investigated the impact of chromatin organization using trichostatin A (TSA), a histone deacetylase inhibitor (Figure 2-7(b)). Chromatin interacts closely with the nuclear envelope and is integral to nuclear stability [158]. Theoretically, the inhibition of histone deacetylation promotes a relaxed, open chromatin structure, rendering the nucleus more deformable [30, 159]. In our experiments, the TSA treatment induced a downward trend in the stiffness as the concentration increased (Control: 2.70 ± 0.86 kPa, n = 30; 250 nM: 2.64 ± 0.92 kPa, n = 31; 500 nM: 2.42 ± 0.76 kPa, n = 26). However, because these differences were not statistically significant, we infer that contribution of chromatin to the global cell stiffness is minor relative to that of the actin cytoskeleton under a large deformation.

Following the assessment of structural inhibitors, we explored the effects of the chemotherapeutic agent daunorubicin. Daunorubicin isreported to induce a drastic increase in leukemic cell stiffness via actin remodeling. To verify this, we compared the mechanical responses of K562 and HEK293 cells. In our study, K562 cells exhibited a modest increase in stiffness (Figure 2-7(c)). This trend is qualitatively consistent with the reported stiffening, but the magnitude is significantly lower than the 14- to 91-fold increase observed in Ref. [41].

This quantitative discrepancy is likely attributable to differences in the probing depth and

measurement scale. The previous study utilized AFM, which typically indents the cell surface at the nanometer-to-micrometer scale, making it highly sensitive to the local mechanics of the actin cortex lying immediately beneath the plasma membrane. In contrast, our microhand system induces large whole-cell deformations to evaluate the global mechanical properties. Therefore, our results suggest that although the daunorubicin treatment triggers significant stiffening of the cortical actin shell (as detected by AFM), the change in the bulk viscoelasticity of the deep cytoplasm and nucleus is less pronounced. Consequently, the stiffening appears more modest when averaged over the entire cell volume. Conversely, the significant softening observed in the HEK293 cells under identical conditions highlights a fundamental difference: unlike K562 cells, which reinforce their cortex, HEK293 cells undergo global structural loss.

To evaluate the potential effect of enzymatic harvesting, we addressed the concern that trypsinization—the standard method used in our earlier measurements—might alter the cell surface properties [160-162]. We conducted a comparative stiffness analysis between trypsinized and non-trypsinized HEK293A cells. Although untreated (non-trypsinized) cells exhibited a slightly higher mean stiffness (3.21 ± 1.09 kPa, $n = 36$) than that of their trypsinized counterparts (2.84 ± 1.15 kPa, $n = 57$), this difference did not reach statistical significance. This finding suggests that, within the sensitivity range of our microhand system, the degradation of membrane proteins or loss of extracellular matrix (ECM) components associated with 2D culture has a negligible effect on the global stiffness of HEK293A cells in suspension (Figure 2-8). Nevertheless, the stiffness histogram for non-trypsinized cells displays a discernible shift toward higher values. These observations demonstrate that the microhand system is capable of detecting subtle mechanical variations, validating its utility in detailed investigations of the cell–ECM interactions across various experimental conditions.

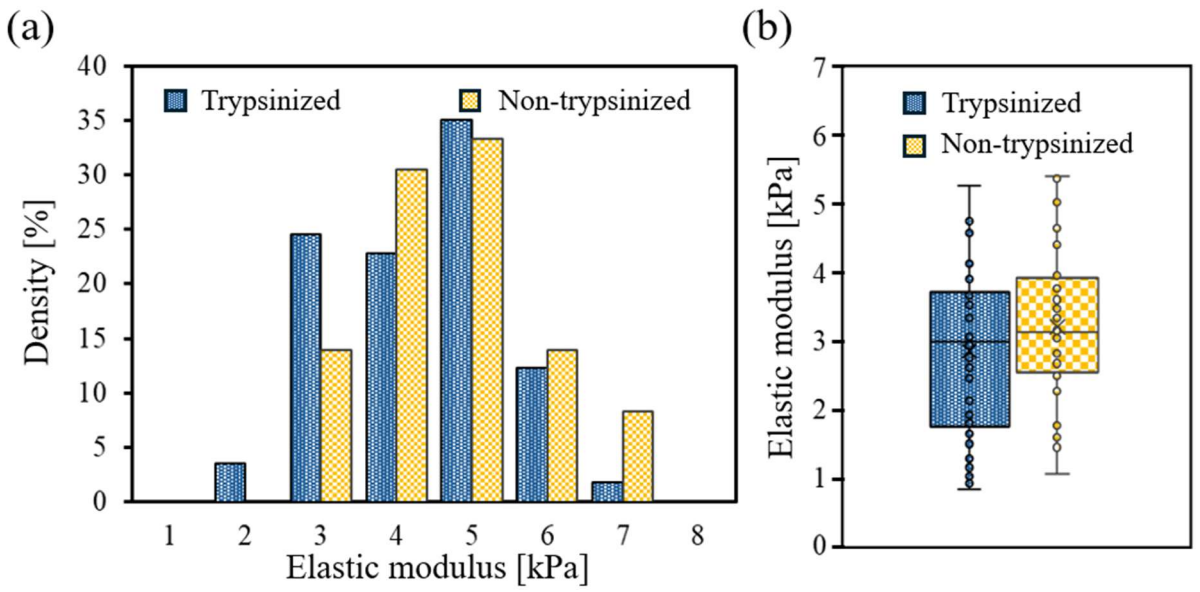

Figure 2-8. Comparative analysis of cell stiffness in trypsinized (n = 57) and non-trypsinized (n = 36) populations. (a) Histogram illustrating the stiffness distribution overlap between the two conditions. (b) Box plot revealing that non-trypsinized cells possess a marginally higher stiffness than that of the trypsinized group.

3.5 Altered Mechanical Characterization in HGPS Model Cells

HGPS stems from mutations in the *LMNA* gene, which disrupt the proper assembly of the nuclear lamina. This genetic defect results in the accumulation of a farnesylated prelamin A variant, termed progerin, in the inner nuclear membrane, preventing the formation of a functional lamina network [163, 164]. Consequently, this accumulation drives nuclear deformation, sclerosis (hardening), and loss of mechanical resilience [165].

To establish a pathological model of HGPS, we transfected HEK293A cells with an EGFPC1-human progerin plasmid. Successful transfection was verified via Green Fluorescent Protein (EGFP) expression (Figure 2-9(a,b)). Morphological analysis revealed that the nuclear shape of Lamin A OX cells was indistinguishable from that of wild-type cells, whereas Progerin OX cells displayed distinct surface wrinkling (Figure 2-9(c): left). This phenotype is consistent with the established characteristics of HGPS cellular models [166]. Notably, prior studies suggest that progerin expression causes a reduction in nuclear F-actin, thereby altering the nuclear shape [167] while concurrently increasing cytoplasmic F-actin and altering

mechanotransduction responses [168]. To investigate this, we examined the F-actin cytoskeleton. However, under our experimental conditions, no significant morphological reorganization of the F-actin network was observed across the different cell types (Figure 2-10).

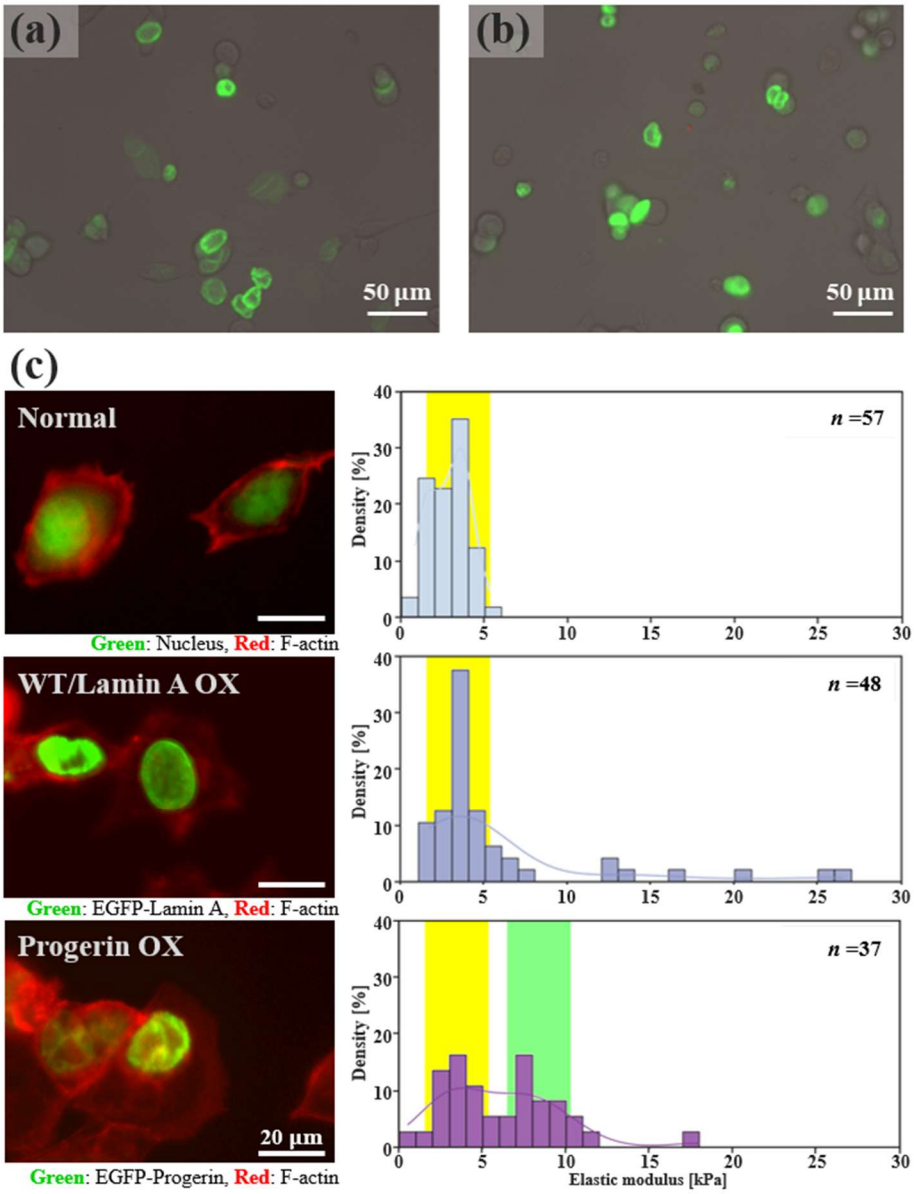

Figure 2-9. Modulation of HEK293A morphology and stiffness via Lamin A and progerin overexpression. (a,b) Fluorescence micrographs confirming the expression of EGFP-tagged wild-type lamin A and progerin in transfected populations. (c) Left: Comparative morphology and actin cytoskeletal organization in wild-type, Lamin A OX, and Progerin OX cells. Right: Histograms displaying the distribution of cellular elastic moduli for each condition. The y-axis denotes density (fraction of cells per 1 kPa bin). The yellow shaded region indicates the contribution of native lamin A, whereas the green shaded region reflects the influence of progerin.

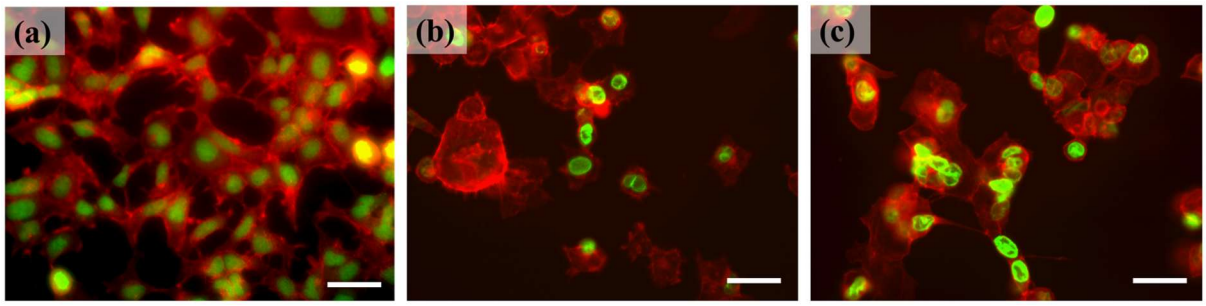

Figure 2-10. Fluorescence micrographs of transfected HEK293A cells. (a) Control group. (b, c) Cells overexpressing EGFP-tagged lamin A and progerin, respectively. Red fluorescence indicates F-actin, whereas green fluorescence indicates the nucleus. Scale bar: 50 μm.

Subsequently, cellular elastic moduli were quantified using the microhand system. Both Progerin OX and Lamin A OX populations demonstrated a wider distribution of the stiffness values than that of normal cells (Figure 2-9(c): right). The histograms for all groups displayed a dominant peak in the 2–4 kPa range, which we attribute primarily to the mechanical contribution of the endogenous cytoskeleton. Notably, the Progerin OX group exhibited an additional distinct peak at 6–8 kPa. In the case of Lamin A OX, the histogram showed a right-skewed distribution, indicating a substantial contribution of the lamin A protein to global cell stiffness. We hypothesize that overexpression of wild-type lamin A increases the stiffness by reinforcing the pre-existing lamina meshwork [77]. Conversely, progerin fails to integrate into a functional network; instead, it accumulates at the nuclear envelope, leading to an altered stiffness profile. These observations align well with the results of previous micropipette aspiration studies, which reported nuclear stiffness values of ~4 kPa for normal HeLa cells versus ~9 kPa for progerin-expressing cells [43]. Consequently, we interpret the lower peak (2–4 kPa) in Progerin OX cells as representing the baseline contribution of native lamin A, whereas the higher peak (6–8 kPa) reflects progerin accumulation. This suggests that once progerin expression surpasses a specific threshold, its stiffening effect on the nuclear envelope overrides the mechanical properties of the endogenous network. These findings demonstrate that the microhand system, equipped with planar end-effectors, is highly effective in characterizing the mechanical properties and identifying variations associated with internal

cellular structures. The ability of the system to resolve subtle mechanical shifts resulting from structural alterations provides valuable insights into their mechanobiological impact.

3.6 Viscoelastic Properties of HEK293A Cells at Different Indentation Speeds

To characterize the viscoelastic profile of HEK293A cells, we monitored the mechanical responses while modulating the indentation velocity between 2.5 and 15.0 μm/s (Figure 2-11(a)). We subsequently distinguished the viscoelastic behaviors under two regimes: low compression (targeting the cytoplasm) and high compression (targeting the nucleus). Data analysis was performed using the following power-law rheological model [169]:

$$E(t) = E_0 \left(\frac{t}{t_{ref}} \right)^{-\beta} \quad (1)$$

Here, E(t) represents the time-dependent elastic modulus, E_0 denotes the initial elastic modulus, t_{ref} is the reference time (fixed at 1 s), t is the indentation duration, and β is the power-law exponent. Physically, a β value of 0 indicates a purely elastic solid with modulus E_0, whereas a β value of 1 describes a Newtonian viscous fluid. We fitted this equation to our experimental data to derive E_0 and β for each compression state.

The modeling results revealed that HEK293A cells possess a higher constant elastic modulus at greater depths (nuclear region) than that at shallower depths (cytoplasmic region). Moreover, the power-law exponent β suggested that the nucleus exhibits a more prominent solid-like (elastic) behavior, whereas the cytoplasm shows more fluid-like (viscous) characteristics (Figure 2-11(b)). This divergence highlights the distinct mechanical contributions of the nuclear and cytoplasmic compartments to the global cellular response. These findings confirm that the microhand system is capable of effectively discriminating between the mechanical properties of the nucleus and cytoplasm.

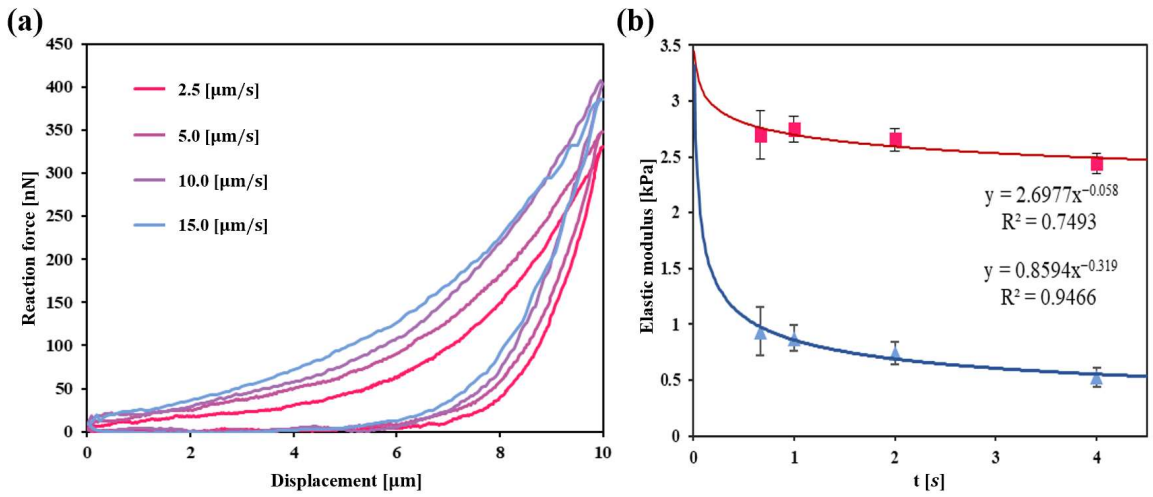

Figure 2-11. (a) Force–displacement profiles recorded at varying indentation speeds. (b) Comparative analysis of elastic moduli derived from the power-law model. Red and blue bars represent high-compression (nucleus) and low-compression (cytoplasm) conditions, respectively. Error bars indicate standard error ($n \geq 16$).

4. Conclusion

In this chapter, we established the foundation of the microhand system for stable and precise measurement of cell stiffness. Our investigation into the end-effector geometries demonstrated that plate-shaped end-effectors significantly outperform needle-shaped ones in terms of measurement stability and accuracy. This setup allowed for the separate evaluations of the cytoplasmic and nuclear mechanical properties by controlling the indentation depth and speed. The biological applicability of the system was successfully validated through experiments with cytoskeleton-modulating agents and by detecting the distinct stiffness alterations in the HGPS model cells overexpressing progerin. In terms of measurement efficiency, the proposed method achieved a throughput of approximately 60 cells/h, owing to the rapid grasping and measurement capabilities of the microhand. This represents a 5- to 10-fold increase compared to conventional contact-based methods, which are typically limited to a few to a dozen cells per hour [144]. This high temporal efficiency suggests a significant advantage for analyzing clinical samples that require rapid profiling of large cell populations, such as CTCs.

However, despite the capability of this system to capture disease-derived mechanical

changes with high sensitivity and throughput, the current manual operation imposes a significant burden on the experimenter to sustain this performance. The dependence on operator skill for cell handling and positioning remains a bottleneck for large-scale analysis. Therefore, an automated manipulation system must be developed to overcome these limitations and enhance the robustness of data collection. This challenge of automating the microhand system to eliminate operator dependence and improve the throughput is addressed in the subsequent chapter.

Some parts of this thesis, including the text and figures, have been previously published in the journal article “Microhand Platform Equipped with Plate-Shaped End-Effectors Enables Precise Probing of Intracellular Structure Contribution to Whole-Cell Mechanical Properties” by Kawakami et al., in *Micromachines*, 2025, 16, 11, (Reference No. 137). These sections are reproduced here with permission from MDPI.

Chapter III

Automated Microhand System for Whole-Cell Stiffness Measurement

1. Introduction

As discussed in Chapter I, quantifying the mechanical properties of single cells is crucial for understanding physiological phenomena such as differentiation, disease progression, and cancer metastasis. Although various methods such as AFM and microfluidic cytometry have been developed [143, 156, 170], achieving both "whole-cell" deformation and precise "manipulation" remains a challenge. Previously, we demonstrated the capability of the microhand system to grasp, carry, and rotate micro-objects [126, 128]. Furthermore, we reported that plate-shaped end-effectors are superior to needle-shaped ones for evaluating the global cell stiffness, as they enable the uniform compression and stable application of large strains [129, 171].

However, accurate stiffness measurement using plate-shaped end-effectors presents significant technical challenges when performed manually. First, precise alignment is critical; the two plates must be perfectly parallel, and the cell must be captured exactly at the center of the end-effectors. Second, manual operation is operator-dependent and time-consuming. Slight misalignment or manual jitter can cause the cell to slip or result in uneven stress distribution, leading to measurement artifacts and low reproducibility. To obtain reliable statistical data, a system that eliminates these human errors and ensures consistent measurement conditions is indispensable.

In this chapter, we present an automated microhand system designed to overcome these

limitations [151]. We established a comprehensive automation algorithm that integrates real-time image recognition and is capable of robustly detecting both end-effectors and cells, with feedback control to precisely align the plate-shaped end-effectors with the measurement target. Furthermore, an automated process to induce large deformations in single cells was implemented to enable consistent stiffness data acquisition without human intervention. Through evaluation experiments, we demonstrated that the system achieves speed and precision comparable to that of a skilled operator. Crucially, by eliminating mental fatigue and concentration limits associated with manual manipulation, the system enables sustained, long-term operation, thereby facilitating large-scale data acquisition that would be difficult to achieve manually.

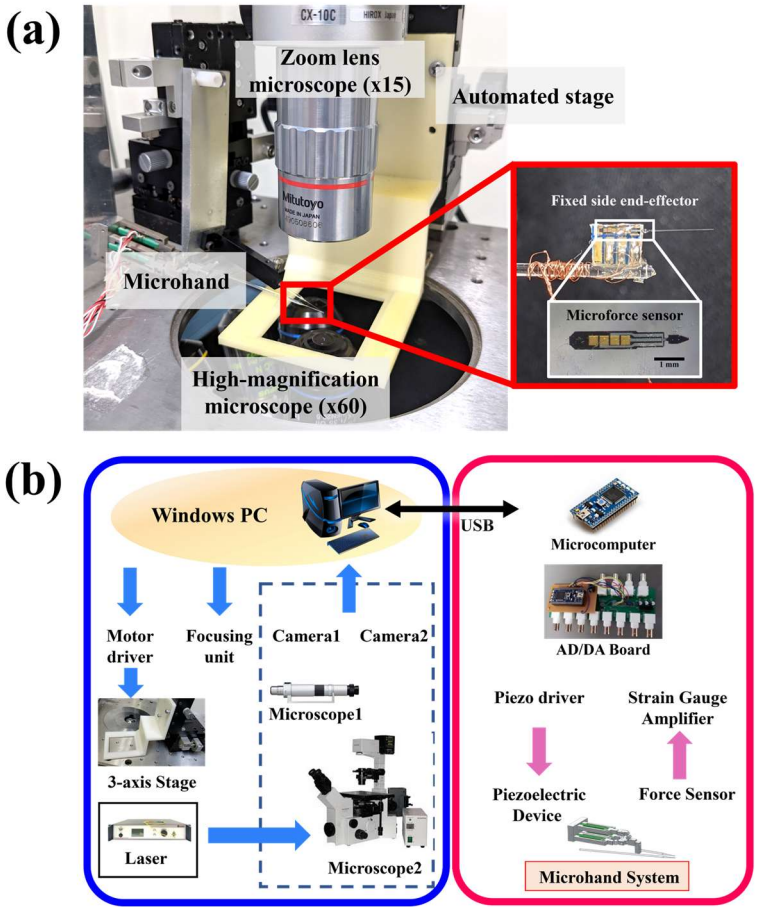

Figure 3-1. Configuration of the automated microhand system. (a) System overview. (b) Detailed schematic of the control architecture.

2. System Configuration

Figure 3-1 illustrates the schematic of the entire system. The configuration of the microhand is identical to that described in Chapter 2. The system was controlled by a Windows PC (Intel Core i7 CPU at 3.50 GHz with 8 GB of RAM) and an mbed LPC1768 microcontroller (NXP Semiconductors). Specifically, the microcontroller processed target displacement commands received from the PC and transmitted the signals to an AD/DA converter board. These control signals were amplified using a piezo driver (HJPZ-0.15Px3, Matsuda Precision) and applied to the three piezoelectric elements of the microhand. For signal monitoring and feedback control, a strain amplifier (MCD-8A, Kyowa Electronic Instruments) was used to amplify the outputs from both the microforce sensor and strain gauges attached to the piezoelectric elements. These amplified signals were returned to the microcontroller via the AD/DA board. Notably, displacement feedback from the strain gauges enabled closed-loop proportional-integral control, ensuring high-precision positioning by compensating for the inherent hysteresis of the piezoelectric elements.

2.1 Fabrication of End-Effectors for Automated Microhand System

The microhand system employed three stacked piezoelectric actuators (AE0203D16, Tokin Corp., Sendai, Japan) to enable 3-DoF translational manipulation [130, 172], achieving a maximum end-effector speed of approximately 70 μm/s. Glass end-effectors were fabricated from 1 mm diameter glass rods using a pipette puller (PC-10, Narishige Co., Ltd., Tokyo, Japan). The tips were first processed into a spherical shape using a microforge (MF2, Narishige) and subsequently ground using a microgrinder (EG-402, Narishige) to create a flat, plate-shaped surface for stable grasping (Figure 3-2). These end-effectors were then mounted onto the microhand. To enable the stiffness measurement of micro-objects, a force sensor was integrated into one of the end-effectors (Figure 3-2(a)).

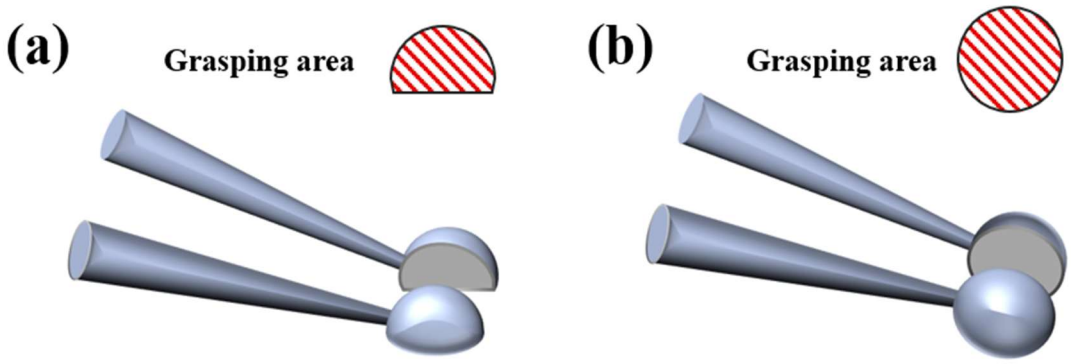

Figure 3-2. Comparison of end-effector geometries. (a) Needle-shaped end-effectors (Previous system). (b) Plate-shaped end-effectors (Proposed system).

2.2 Microforce Sensor

The microforce sensor, based on the design by Tanikawa et al. [122], employed two strain gauges (R_h and R_v) in its sensing section. The force applied to the sensor caused a resistance change in the gauges, which was converted into a voltage signal via a Wheatstone bridge circuit. In this dual-gauge configuration, R_v functioned as a dummy gauge for temperature compensation, ensuring measurement stability against thermal drift.

2.3 Target Cell Trapping via Optical Tweezers

Optical tweezers are a technique for trapping microscopic objects in three dimensions by focusing a single laser beam [173]. In this study, an optical tweezers unit (Laser Optical Tweezers mini2, OptoSigma Corp., Tokyo, Japan) was integrated into the rear port of an inverted microscope (IX83, Olympus Corp., Tokyo, Japan). The system utilized a laser source (1064 nm High Stability Laser Source, Connet Laser Technology Co., Ltd., Shanghai, China) and a 60× oil-immersion objective lens (UPlanSApo 60×, Olympus). A wavelength of 1064 nm (near-infrared) was selected because it minimizes the photodamage to cells and biomolecules [90].

2.4 Simultaneous Observation System

A wide-field microscope and high-magnification microscope were aligned coaxially to facilitate simultaneous observations. A high-magnification microscope (IX83, Olympus Corp.,

Tokyo, Japan) was equipped with a 60× oil-immersion objective lens (UPlanSApo 60×, Olympus Corp., Tokyo, Japan). The wide-field microscope comprised a zoom lens unit (CX10C, Hirox Co., Ltd., Tokyo, Japan) fitted with a 5× objective lens (M Plan Apo 5×, Mitutoyo Corp., Kawasaki, Japan). Hereinafter, the wide-field microscope and high-magnification microscope are referred to as “Microscope 1” and “Microscope 2,” respectively. The images from Microscope 1 and Microscope 2 were acquired by Camera 1 (FL2-03S2C, Point Grey Research Inc., Richmond, BC, Canada) and Camera 2 (DFK 23UM021, The Imaging Source, Bremen, Germany), respectively, as shown in Figure 3-1(b).

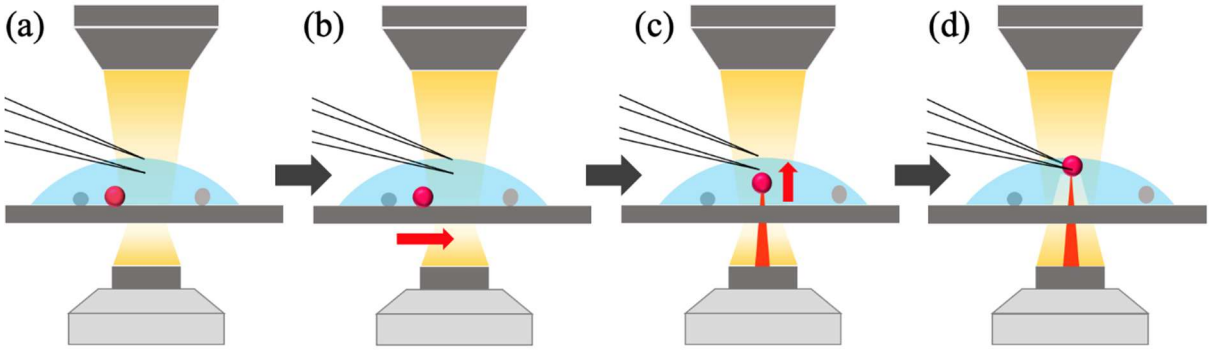

Figure 3-3. Schematic of the stiffness measurement procedure. (a) Initial state. (b) Alignment of the target object to the laser focal point using the automated stage. (c) Levitation of the target object to the height of the end-effectors using optical tweezers. (d) Grasping of the target object by the end-effectors.

3. Automated Stiffness Measurement Using Extended Microhand System

3.1 Comparison Between Manual and Automated Systems

In our previous manual system [174], micro-objects on a glass slide were grasped directly using the microhand near the substrate surface. This configuration imposed constraints on the end-effector geometry, as it required two planar surfaces: one for grasping the cell and another parallel to the glass slide to prevent interference (Figure 3-2(a)). Consequently, precise alignment was required not only between the two end-effectors but also between the end-effectors and glass substrate. Insufficient alignment often resulted in the cell being compressed against the substrate, causing measurement artifacts and instability.

To address these limitations, we developed an automated system that integrates three key features: optical tweezers, an automated stage, and simultaneous observation system employing both wide-field and high-magnification microscopes. The introduction of optical tweezers allows the target object to be levitated prior to grasping. Lifting the target eliminates the need for bottom clearance relative to the glass slide, thereby simplifying the end-effector geometry and securing a larger contact area for stable grasping (Figure 3-2(b)). Furthermore, although optical trapping requires a high-magnification objective lens, which significantly limits the field of view, the integration of a wide-field microscope and an automated stage facilitates the robust detection and efficient transport of target objects.

The resulting stiffness measurement procedure is illustrated in Figure 3-3. The automated process consists of the following steps:

(1) Micro-objects on the glass substrate are detected using the images acquired from the wide-field microscope (Microscope 1) (Figure 3-3(a)).

(2) The target object is identified and translated to the focal point of the optical tweezers using the automated stage (Figure 3-3(a)→(b)).

(3) The target object is trapped and levitated to the same height as that of the end-effectors using optical tweezers (Figure 3-3(c)).

(4) The relative position between the target object and end-effectors is calculated based on the image acquired by the high-magnification microscope (Microscope 2) (Figure 3-3(d)).

(5) The target object is grasped by the microhand, and the optical trap is subsequently deactivated.

(6) The reaction force is recorded during the compression (loading) and release (unloading) cycles of the end-effectors.

Through this established workflow, the system achieves stable and reproducible mechanical characterization. The performance of the proposed system was evaluated through experiments,

mainly with HeLa cells.

3.2 Detection and Transport of Micro-objects

As described in Section 2.4, the high-magnification and wide-field microscopes were aligned coaxially. This configuration enabled simultaneous detailed imaging and wide-area screening. The automated sequence for detecting and transporting micro-objects is described below:

(1) An image of the glass substrate surface is acquired via Microscope 1. The target objects are recognized based on their pixel area after binarizing the image using an adaptive thresholding method [175] (Figure 3-4(a)).

(2) The object closest to the optical center of the field of view of Microscope 1 is selected as the primary target, and the automated stage translates the object to the focal point of the optical tweezers.

(3) Fine alignment is subsequently performed using high-resolution images from Microscope 2 (Figure 3-4(b)) by employing the same image processing algorithm as used in step (1).

This coarse-to-fine search strategy, utilizing both wide-field and high-magnification microscopes, facilitates efficient wide-area screening and achieves positioning accuracy on the order of 1 μm. Crucially, this resolution is sufficient for the stable trapping and levitation of the target cell using optical tweezers.

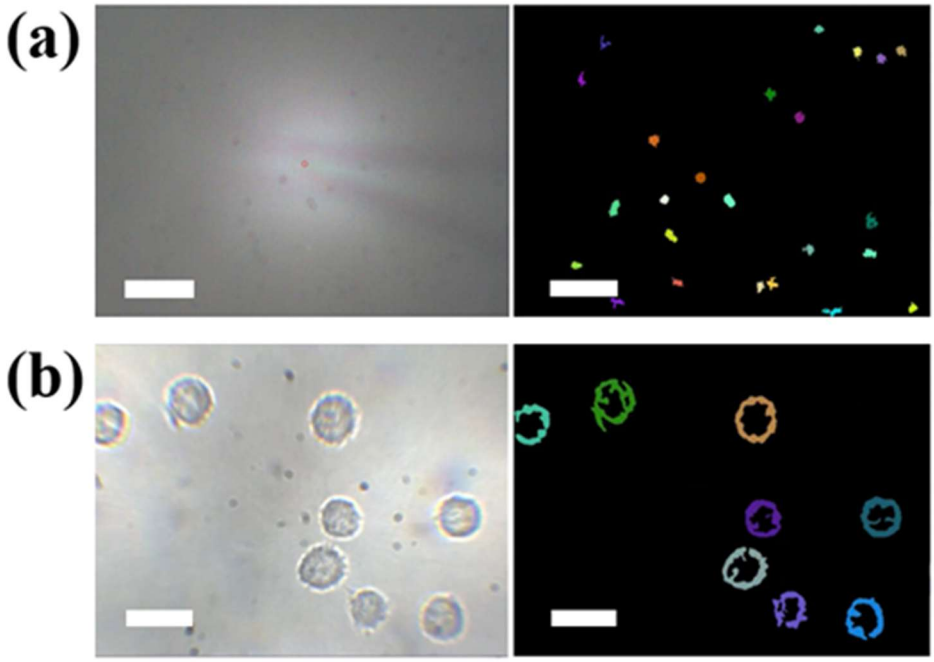

Figure 3-4. Cell detection results. (a) Wide-field image (Microscope 1). Scale bar: 100 μm. (b) High-magnification image (Microscope 2). Scale bar: 20 μm.

3.3 Stable Grasping Using Optical Tweezers

To improve the stability of the stiffness measurement process, the target object is levitated using optical tweezers prior to grasping. However, precise open-loop positioning is challenging because the absolute vertical position of the end-effectors varies slightly between experiments owing to mounting variability and manual adjustments. Therefore, we adopted a relative positioning strategy based on image-based focus evaluation. Because the optical trap is generated at the focal plane of the objective lens, controlling the vertical position (z-position) of the objective lens directly dictates the height of the trapped cell. The alignment of the target object with the grasping height is achieved as follows:

(1) The image obtained from Microscope 2 is converted to grayscale.

(2) A Laplacian filter is applied to the image to extract the edge features [176].

(3) A focus score (degree of focus) is calculated from the pixel values of the filtered image [177].

(4) The target object is levitated from the glass substrate (Figure 3-5(a)) to a position

sufficiently above the end-effectors using optical tweezers (Figure 3-5(b)).

(5) The objective lens is scanned along the z-axis. During this scan, the variance in the pixel values within the end-effector region is monitored as the focus score.

(6) The lens height yielding the maximum variance is identified as the vertical position of the end-effectors. By positioning the objective lens at this height, the trapped cell is automatically aligned with the end-effectors (Figure 3-5(c)).

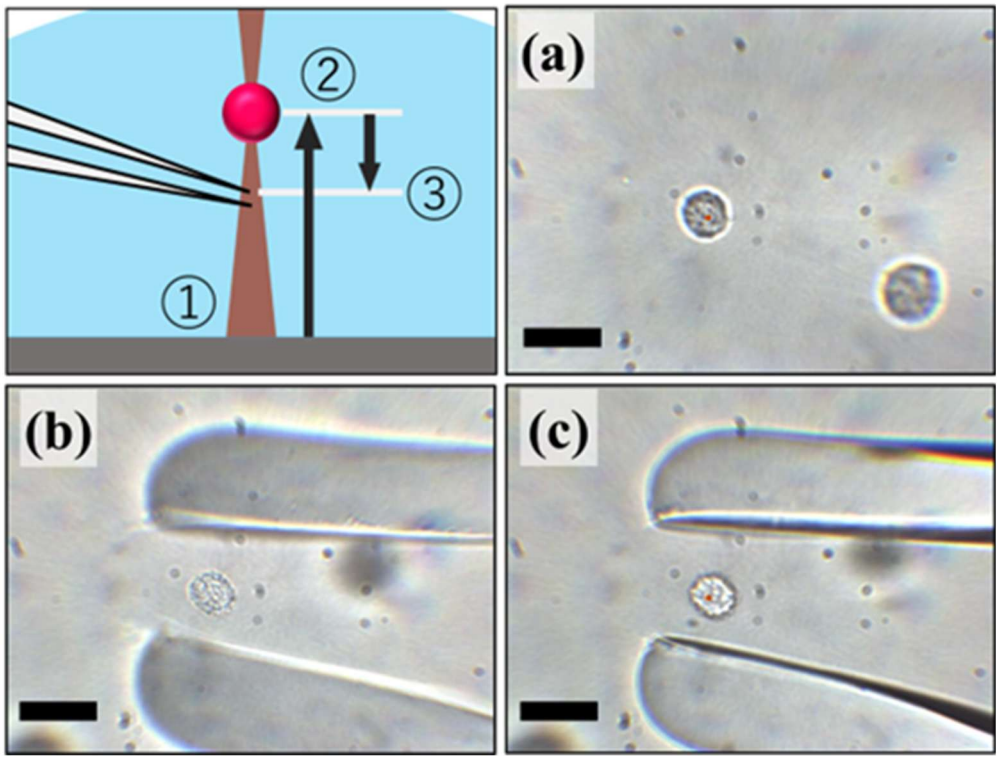

Figure 3-5. Schematic and micrographs of the cell lifting procedure. (a) A cell trapped on the glass slide. (b) The target object lifted slightly above the end-effectors. (c) The target object lowered to the same height as that of the end-effectors for alignment. Scale bar: 20 μm.

3.4 Stable Grasping of Single Cells and Stiffness Measurement Process

Once the target object was levitated to the same height as that of the end-effectors using the optical tweezers, the grasping sequence was initiated based on visual feedback from Microscope 2. The same adaptive thresholding method [175] used for initial screening was employed to recognize the end-effectors and cell (Figure 3-6). Specifically, the two extracted regions with the largest pixel areas were identified as the end-effectors, whereas the object

located near the laser focal point was identified as the target cell (Figure 3-6 Right). The distance between the end-effectors and target object was calculated based on the centroids of these recognized features. The end-effectors were then actuated to close this gap, thereby grasping the target.

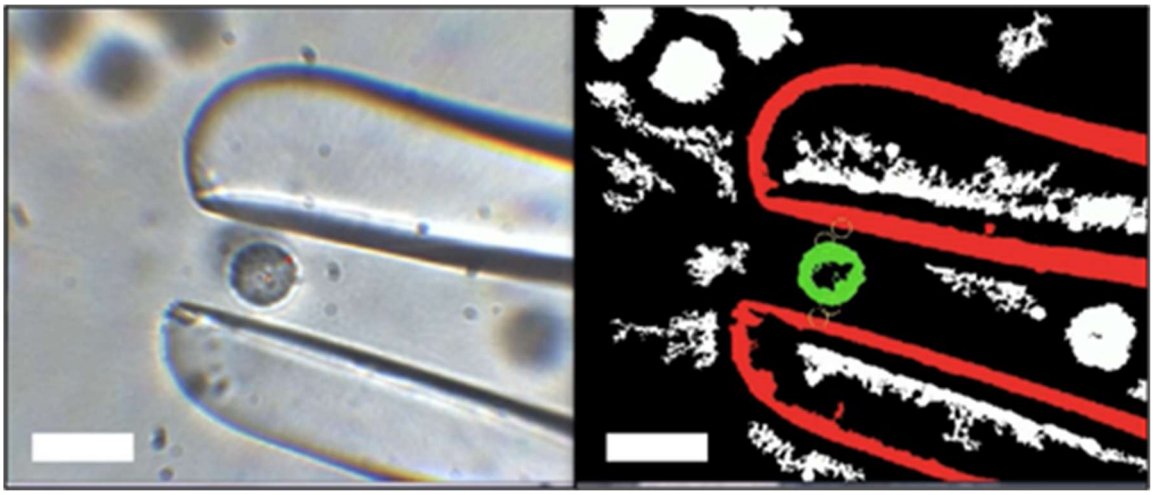

Figure 3-6. Estimation of the distance between the target object and end-effectors. (Left) Raw microscopic image before grasping. (Right) Processed image showing the recognized positions of the end-effectors and cell. Scale bar: 20 μm.

However, a critical challenge in this process is the potential for the target object to slip or fall upon deactivation of the optical trap. To address this, we implemented an automated verification algorithm to confirm whether the target object was successfully retained.

We employed top-hat transformation [178] to process the images captured immediately upon grasping (t = 0 s) and 4 s later (t = 4 s) (Figure 3-7). In a successful grasp, the difference between these sequential images is negligible (Figure 3-8(a,b)). Conversely, if the cell falls or slips, a significant difference is detected (Figure 3-8(c,d)). This detection mechanism allows the system to automatically distinguish between success and failure, enabling appropriate error handling or process retries.

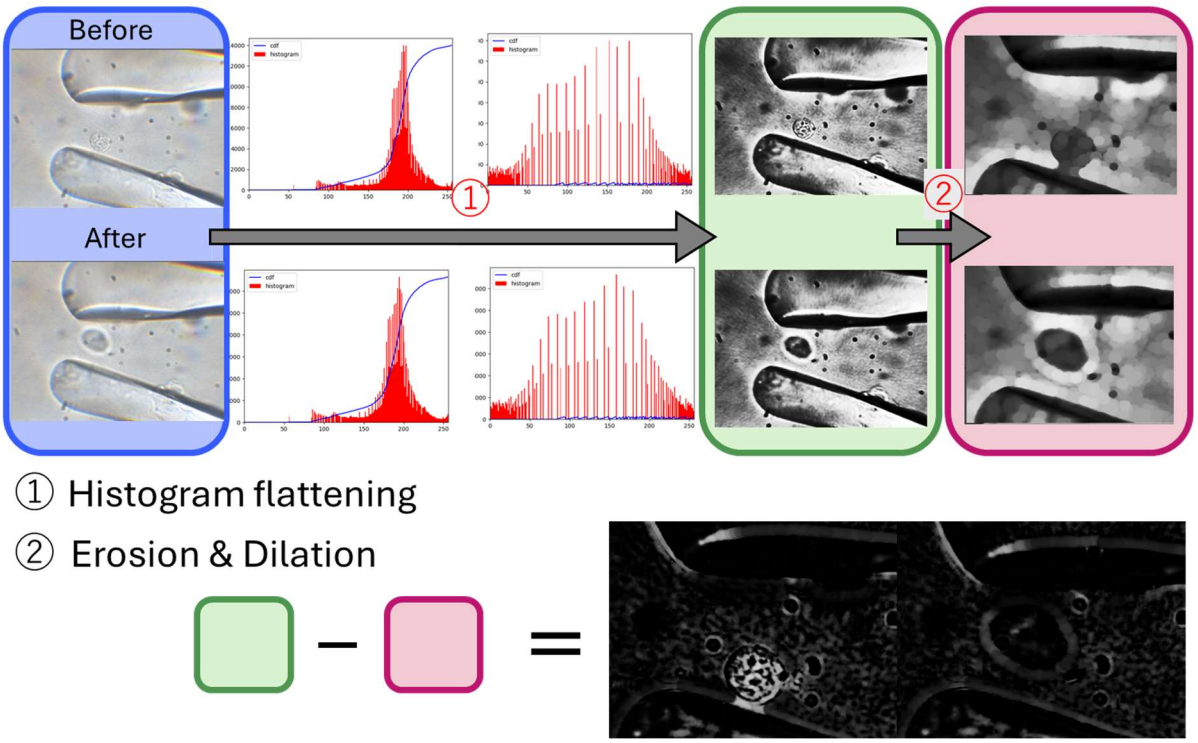

Figure 3-7. Flowchart of the target cell recognition algorithm. First, the histograms of the images before and after grasping are flattened. Then, both images are Gaussian blurred, and the difference image is calculated.

Finally, the reaction force was measured. The automated stiffness measurement was performed by applying compressive loads (loading) and releasing them (unloading) at a programmable speed while monitoring the reaction force via the micro-force sensor.

The accuracy of this processwas verified through a cyclic compression test (displacement: 7 μm, duration: 5 s, two cycles). The force response demonstrated a characteristic increase during loading and decrease during unloading, confirming the successful acquisition of mechanical data (Figure 3-9). This result demonstrates that the reaction force measurement was performed precisely in the automated microhand system. The stiffness can be derived from these measured force data combined with the displacement calculated from the acquired images.

Furthermore, the versatility of the recognition algorithm was tested using various cell lines (C2C12, HEK293A, and HepG2). All cell types were successfully detected and recognized (Figure 3-10). These results indicate that the proposed automated microhand system is robust and applicable to the mechanical characterization of a wide range of cell types.

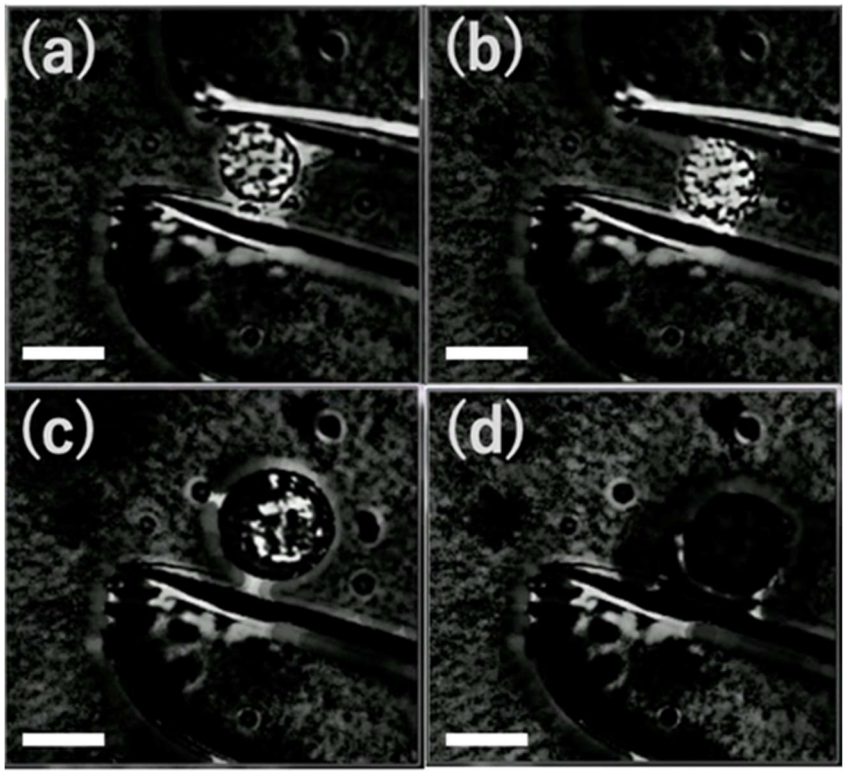

Figure 3-8. Evaluation of grasping stability. Images were taken immediately after grasping (t = 0 s) and 4 s later (t = 4 s). (a, b) A successful grasping case. (c, d) A failed case where the cell slips from the end-effectors. Scale bar: 5 μm.

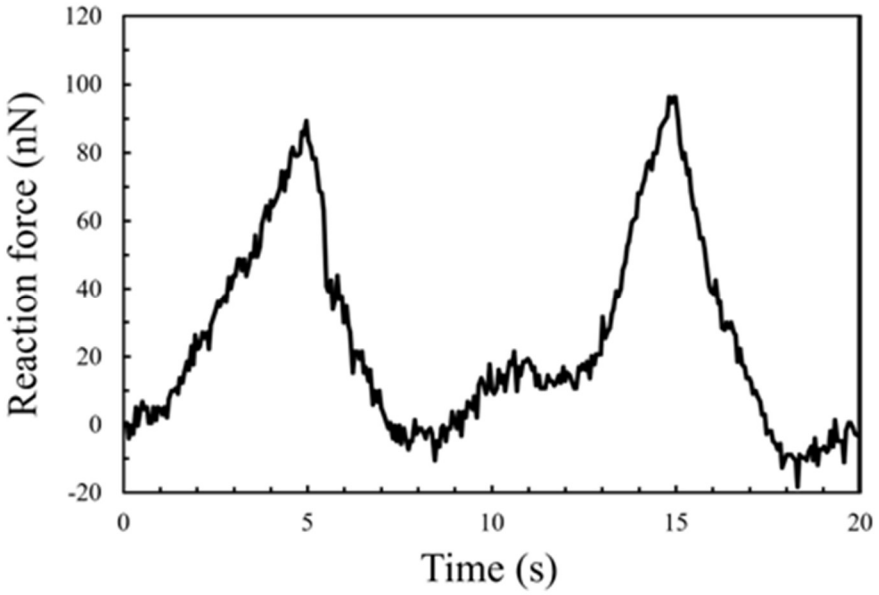

Figure 3-9. Time history of the measured reaction force. The cell was subjected to two compression cycles (pushing and releasing) resulting in a deformation of 7 μm over 10 s.

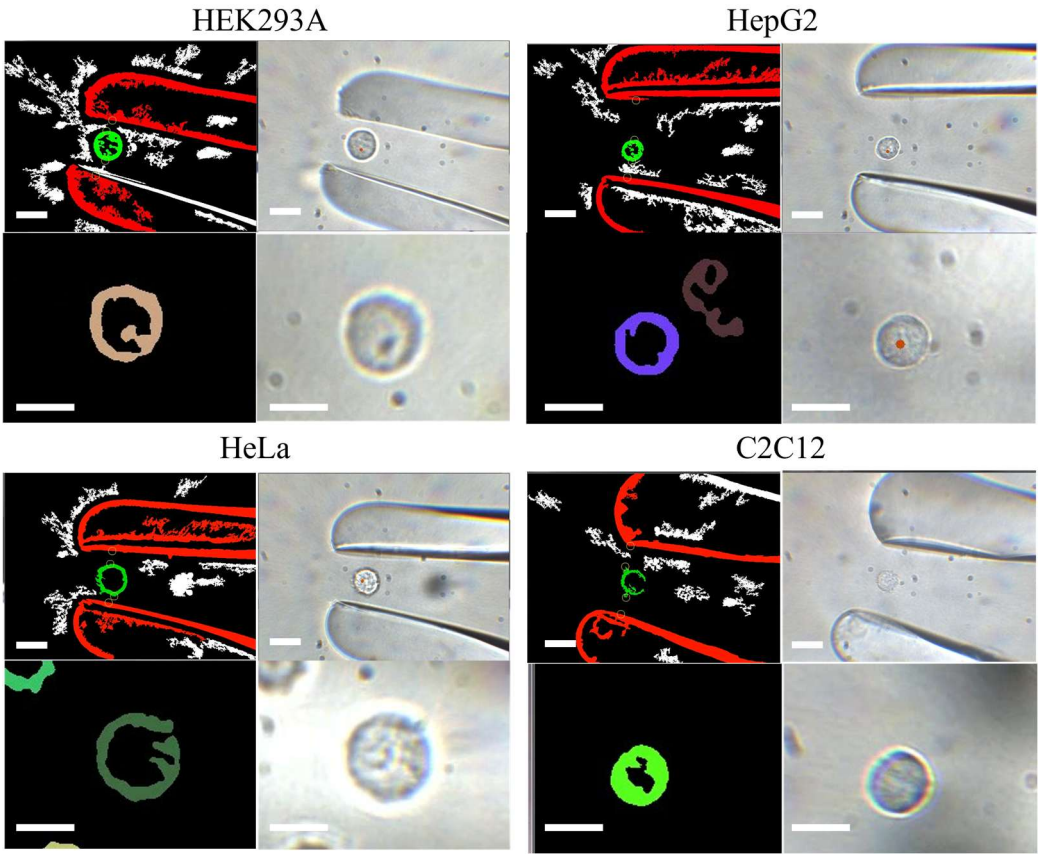

Figure 3-10. Image recognition results. (Top) Recognition of the cell and end-effectors during the grasping procedure. (Bottom) Recognition of various cell lines (HEK293A, HepG2, HeLa, C2C12) on the glass substrate.

4. Evaluation Experiment for Automated Stiffness Measurement System

To evaluate the performance of the extended microhand system described above, we assessed the success rate of the automated measurement process. Additionally, the efficiency of the system was evaluated by comparing the measurement time of the automated system against that of a manual operation performed by a highly skilled operator.

4.1 Evaluation of the Success Rate of Each Process

The success rates were evaluated for the following three sequential procedures in the automated system: (1) Search and Centering: The target object is detected using Microscopes 1 and 2 and translated to the center of the field of view (Figure3-3(a) → (b)). (2) Levitation: The trapped cell is levitated to the appropriate height using optical tweezers (Figure 3-3(b) → (c)). (3) Grasping: The distance between the end-effectors and cell is determined, and the cell

is grasped (Figure 3-3(c) → (d)).

The success and failure rates were calculated by performing each of the above steps 20 times. A potential issue was that the optical tweezers might fail to lift cells that are strongly adhered to the glass substrate. Because it is difficult to visually distinguish the adhered cells from non-adhered ones solely from static images, we applied vibration to the substrate beforehand to identify and select only the non-adhered cells for this experiment.

As summarized in Table 3-1, processes (1) and (2) achieved a 100% success rate, transitioning smoothly to the next step in every trial. However, the success rate of process (3) (Grasping) was 65%. The primary cause of failure in this step was the cell slipping or falling from the end-effectors. In addition to the physical success rate, we evaluated the accuracy of the "cell fall recognition" algorithm (described in Section 3.4). The system correctly identified whether a cell had fallen with an accuracy of 75% (9/12 cases). Although the grasping step remains challenging owing to the physical properties of the cells, the implemented fall recognition algorithm successfully identified failures in most cases. This capability allows the system to automatically trigger error recovery or retry protocols, thereby establishing a robust workflow that enables continuous data acquisition, even under occasional grasping failures.

Table 3-1. Success rates of individual processes in the automated microhand system.

Process	**(a)→(b)** **Stage movement**	**(b) →(c)** **Object uplift**	**(c) →(d)** **Grasping**
Success rate	20/20 (100%)	20/20 (100%)	13/20 (65%)

4.2 Comparison Between Manual Operation by a Skilled Operator and the Automated System

To evaluate the efficiency of the automated system, we measured the total time required for a single stiffness measurement cycle, defined as the duration from searching for a target object to successfully grasping it. We compared the time taken by the automated system with that of

a manual operation performed by a skilled operator. Table 3-2 lists the average time calculated from five measurement trials. The results showed no significant difference in the average time between the manual and automated methods. Although the speed was comparable to that of a skilled expert, it is important to note that the automated system maintains this speed without fatigue or concentration loss. These results suggest that the automated microhand system is capable of grasping, manipulating, and measuring the reaction forces of micro-objects efficiently and reproducibly.

Table 3-2. Comparison of operation time between the automated system and a skilled operator.

	1st	2nd	3rd	4th	5th	Average
Automated system	67 s	67 s	70 s	72 s	69 s	69.0 ± 2.1 s
Skilled operator	68 s	62 s	65 s	59 s	60 s	62.8 ± 3.7 s

4. Conclusion

In this chapter, we discussed the development of an automated microhand system to address the operational challenges associated with plate-shaped end-effectors. By implementing a comprehensive algorithm that integrates real-time image recognition with feedback control, we successfully achieved precise automated alignment and resolved the issues of operator dependence found in the previous manual system. Evaluation experiments confirmed that the system maintains measurement stability and processing speed equivalent to that of a skilled expert. Significantly, this automation eliminates the requirement for advanced manipulation skills while overcoming the constraints of human concentration and fatigue. Consequently, the proposed system enables sustained and long-term operation. We believe that this platform has significant potential to accelerate large-scale data acquisition in single-cell mechanics, paving the way for high-throughput mechanical phenotyping.

Chapter IV

Photocontrollable and Reversible Cell Adhesion via Host–Guest Interaction between Azobenzene-PEG-Lipid and Cyclodextrin

1. Introduction

In this chapter, we present a foundational technology for the future advancement of the microhand system: a non-invasive, photocontrollable cell adhesion method. As demonstrated in Chapters 2 and 3, the microhand system enables precise physical manipulation of single cells. However, physical grasping inherently carries the risk of mechanical stress and faces challenges in stably holding non-adherent cells without excessive compression. To overcome these limitations and expand the versatility of the system, we propose a chemical approach that utilizes light-responsive molecular interactions to control cell capture and release. In this chapter, as a proof of concept for future implementation on end-effectors, we introduce a photocontrollable adhesion system developed on a glass substrate [179].

In the broader context of cell biology, beyond the specific scope of micromanipulation, the precise regulation of cell adhesion remains a pivotal challenge. Cellular phenotypes and behaviors often diverge significantly depending on whether cells exist in isolation or form collective groups [138, 180]. Unraveling the relationship between individual cellular behavior and intercellular interactions is fundamental to understanding complex biological processes, including tissue repair [181, 182], cancer progression [183, 184], and immunological responses [185-187]. Consequently, the development of cell patterning technologies has been vigorously pursued over the past two decades to facilitate the precise positioning of cells for the observation of their dynamic behaviors.

The methods for the spatial arrangement of cells are generally classified into physical and

chemical methods. Physical techniques, which employ tools such as microfluidic devices [188] or topographical surface features [189], are effective in confining the cell attachment to designated regions. However, these static physical barriers often suffer from a lack of flexibility, making it difficult to perform dynamic manipulations—such as modifying the patterns during observation or selectively arranging the heterogeneous cell populations.

To address the rigidity of physical methods, chemical strategies enabling molecular-level regulation have garnered significant attention [190-195]. These approaches typically integrate surface chemistry with microfabrication to spatially dictate cell adhesion. Prominent examples include the direct deposition of biomolecules using inkjet systems [190] and generation of chemical patterns via photolithography utilizing photosensitive materials or cleavable linkers [191]. Additionally, soft lithography techniques, such as microcontact printing, allow for the transfer of specific chemical functionalities onto the substrate [192, 193]. These techniques have achieved remarkable precision, enabling patterning down to single-cell resolution [193, 194].

Among chemical approaches, stimuli-responsive molecular systems—particularly those activated by light—are invaluable for studying intercellular communication and drug efficacy owing to their capacity for spatiotemporal on/off regulation [195]. For instance, the UV-cleavable 2-nitrobenzyl group has been extensively utilized to track cell migration [181, 182] and to modulate the substrate properties for observing the heterogeneous cytotoxic interactions between immune and cancer cells [185]. Despite their utility, photocleavage-based methods generally suffer from a major drawback: their irreversible nature limits their application in dynamic, repetitive manipulations.

To enable reversibility, dynamic systems based on azobenzene photoisomerization have been developed. This mechanism has been applied to modulate cell adhesion by reversibly masking adhesion peptides such as Arg-Gly-Asp (RGD) [196-199]. Moreover, azobenzene

forms a specific, photo-tunable host–guest complex with cyclodextrin, a cyclic oligosaccharide [200]. Owing to its biocompatibility and simplicity, this interaction has found applications in drug delivery [201], intercellular adhesion control [202, 203], and dynamic hydrogels [204]. However, existing reversible systems utilizing this interaction predominantly depend on receptor-specific ligands, such as RGD peptides [186, 205] or aptamers [206]. This reliance restricts their application to adherent cells, effectively excluding non-adherent populations such as immune cells, hematological malignancies, and circulating tumor cells [207]. Given the growing necessity to analyze interactions involving these cell types, expanding the azobenzene-based strategy to non-adherent cells is essential for establishing a truly versatile adhesion control platform.

Although PEG-azobenzene conjugates have been widely investigated for self-assembly and hydrogel applications [208-211], their potential for regulating adhesion via direct cell membrane engineering remains unexplored. To bridge this gap, this chapter introduces a molecular system designed for the photocontrol of reversible cell adhesion in a cell-type-independent manner. We synthesized an azobenzene-BAM conjugate (AzoBAM) by linking azobenzene to a Biocompatible Anchor for Cell Membrane (BAM), which features an oleyl chain for direct insertion into the lipid bilayer without the need for specific receptors [212]. Concurrently, β-cyclodextrin (β-CD) was immobilized on glass substrates to serve as the docking surface. In this system, adhesion is driven by host–guest complexation between the *trans*-azobenzene on the cell membrane and β-CD on the substrate. Herein, we report the synthesis and characterization of these components. Crucially, by using human chronic myelogenous leukemia (K562) cells as a model for non-adherent cells, we successfully demonstrated the fully reversible photocontrol of cell–substrate interactions, achieving not only initial adhesion and light-induced detachment but also subsequent re-adhesion. Furthermore, the relationship between adhesion efficiency and adhesion force was

quantitatively analyzed to optimize the molecular design. This study offers a novel strategy for manipulating non-adherent cells by targeting the ubiquitous lipid bilayer, providing a distinct approach when compared with conventional receptor-based methods.

2. Materials and Methods

2.1 General Procedure and Materials

The heterobifunctional PEG derivatives used in this study, specifically SUNBRIGHT® OE-020CS, OE-040CS, and OE-080CS (corresponding to BAM-NHS 2k, 4k, and 8k with molecular weights of 2144, 4237, and 8235, respectively), were acquired from NOF Corporation (Tokyo, Japan). The following key chemical reagents were sourced: 3-glycidyloxypropyltrimethoxysilane (GPS) from Sigma-Aldrich (St. Louis, MO, USA); 4-(phenylazo)benzoic acid and p-toluenesulfonyl chloride (TsCl) from Tokyo Chemical Industry (Tokyo, Japan); and β-cyclodextrin (β-CD) from Junsei Chemical (Tokyo, Japan). FUJIFILM Wako Pure Chemical (Osaka, Japan) supplied fatty acid-free bovine serum albumin (BSA) as well as reagent-grade ethylenediamine (EDA), *N*-hydroxysuccinimide (NHS), and *N,N'*-dicyclohexylcarbodiimide (DCC).

K562 cells provided by RIKEN BioResource Research Center (Tsukuba, Japan) were used. Culture media components, including RPMI 1640 medium and fetal bovine serum (FBS), were obtained from Nissui Pharmaceutical (Tokyo, Japan) and Gibco (Grand Island, NY, USA), respectively. Calcein-AM and propidium iodide (PI) were purchased from Nacalai Tesque (Kyoto, Japan). All chemicals were used as received without further purification.

2.2 General Measurements

Proton nuclear magnetic resonance (^{1}H NMR) spectra were acquired at 20 °C using a JNM-ECS400 spectrometer (400 MHz, JEOL Ltd., Tokyo, Japan). The optical properties were evaluated by recording the UV-vis absorption spectra with a Shimadzu UV-2600 spectrometer (Kyoto, Japan). To characterize the surface properties of the modified substrates, the zeta

potentials were determined at room temperature using an ELSZ-2000 analyzer (Otsuka Electronics, Osaka, Japan). Surface wettability was assessed using a contact angle meter (LSE-ME3; Nick Corporation, Saitama, Japan) by gently depositing a 1 μL droplet of deionized (DI) water onto the sample surface at room temperature and immediately recording the contact angle.

Photoisomerization experiments were conducted using LED light sources from Optocode Corporation (Tokyo, Japan): a UV-LED (EX-365/L) with an intensity of 16.6 W/m^2 and visible LED (EX-450) with an intensity of 157 W/m^2. The irradiance levels were verified using a CL-70F illuminance meter (Konica Minolta Japan Inc., Tokyo, Japan) and USR-45 spectroradiometer (Ushio Inc., Tokyo, Japan). Although a quantitative purity analysis was not performed, careful purification protocols were employed for all synthesized compounds. ^{1}H NMR spectroscopy was used to confirm the structural identity and absence of significant impurities within the detection limits.

2.3 Preparation of CD-functionalized Glass Substrate

The cyclodextrin-modified glass (CD-glass) was prepared via a two-step process. First, β-CD was tosylated and subsequently reacted with ethylenediamine to synthesize an amine-terminated β-CD (β-CD-EDA) according to the reported procedure [213] (Figure4-1(a)). The resulting β-CD-EDA was then reacted with an epoxy-functionalized glass slide to yield the final CD-glass (Figure 4-2(a)).

2.3.1 Synthesis of Mono-6-tosyl-β-cyclodextrin (β-CD-OTs)

β-CD (10.1 g, 8.90 mmol) was dissolved in DI water (80 mL) in a flask. A solution of NaOH (4 M, 6.84 mL) was added dropwise to the β-CD solution over 10 min while stirring in an ice-water bath. Subsequently, a solution of TsCl (1.99 g, 10.4 mmol) was added dropwise in acetonitrile (5.0 mL) over 1 h at the same temperature. The reaction mixture was stirred at room temperature for 4 h. The resulting precipitate was removed by vacuum filtration, and the pH was adjusted to ~6.0, using 1 M HCl. The solution was stored at 4 °C overnight to induce

recrystallization. The white crystalline product was collected via vacuum filtration, washed three times with cold acetone, and dried under vacuum to yield the title compound (1.70 g, 15%). ^{1}H NMR (400 MHz, DMSO-d_6): δ 7.75 (d, J = 7.3 Hz, 2H, Ar-H), 7.43 (d, J = 7.7 Hz, 2H, Ar-H), 5.71–5.64 (m, 14H, OH-2,3), 4.83 (d, J = 3.5 Hz, 7H, H-1), 4.52–4.38 (m, 6H, OH-6 and H-6'), 3.64–3.40 (m, 28H, H-3,5,6), 3.40–3.30 (m, 14H, H-2,4 overlapped with HDO), 2.43 (s, 2.5H, Tosyl-CH_3) ppm (Figure 4-1(b)). The degree of substitution (DS) was calculated to be 0.80 based on the integral ratio of the tosyl aromatic signals to the anomeric signal (H-1), confirming the successful synthesis of mono-tosylated β-CD.

2.3.2 Synthesis of Mono-6-(2-aminoethyl)amino-6-deoxy-β-cyclodextrin

β-CD-OTs (1.0 g, 0.79 mmol) were dissolved in EDA (10 mL), and the solution was stirred at 80 °C for 4 h under a nitrogen atmosphere. After the reaction was complete, excess EDA was removed by rotary evaporation. The crude residue was dissolved in a minimum amount of methanol/water mixture (1:1, v/v) and precipitated by adding the solution dropwise to a large volume of cold acetone with vigorous stirring. This dissolution–precipitation cycle was repeated three more times for purification. The final white product was collected via filtration and dried under vacuum (889.4 mg, 96%). ^{1}H NMR (400 MHz, D_2O): δ 5.09 (d, J = 3.5 Hz, 7H, H-1), 4.82 (HDO), 3.99–3.86 (m, 28H, H-3,5,6), 3.68–3.58 (m, 14H, H-2,4), 2.91 (m, 4H, EDA-CH_2) ppm (Figure 4-1(c)). The DS of the amino group was determined to be 0.9 based on the ^{1}H NMR integration ratios. Because unreacted β-CD lacks the amino group and does not participate in the subsequent conjugation reaction, the mixture was used without further separation of the mono-substituted product.

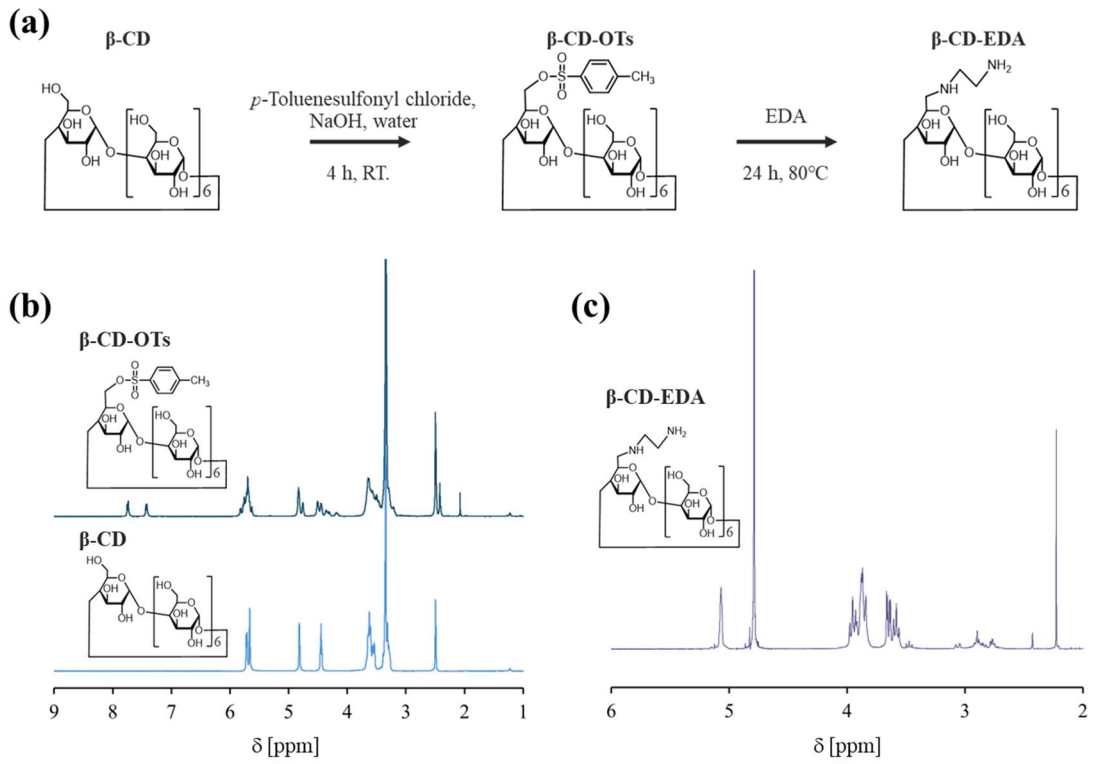

Figure 4-1. Synthesis and NMR characterization of β-cyclodextrin (β-CD) derivatives. (a) Synthetic scheme of mono-6-(2-aminoethyl)amino-6-deoxy-β-CD (β-CD-EDA). (b) ^{1}H NMR spectra of β-CD and mono-6-tosyl-β-CD (β-CD-OTs) in DMSO-d_6. (c) ^{1}H NMR spectrum of β-CD-EDA in D_2O.

2.3.3 Cyclodextrin Modification on Glass Substrate

The borosilicate glass substrates were cleaned by sonication in water and ethanol. The substrates were immersed in a 1 M aqueous KOH solution for 4 h. After rinsing with DI water and drying under vacuum at room temperature, the substrates were reacted with a GPS solution in anhydrous toluene (2.0% v/v) for 2 h at room temperature. The substrates were subsequently washed with toluene and ethanol and cured for 15 min at 120 °C. Finally, the GPS-modified glass substrates were immersed in a solution of β-CD-EDA (10 mM in DMF) and incubated overnight at 60 °C to obtain the final CD glass (Figure 4-4(a)).

2.4 Synthesis of AzoBAM

2.4.1 Synthesis of *N*-succinimidyl-4-(phenylazo)benzoate

We synthesized the target NHS ester based on the method reported in literature [214], with a modified purification procedure. NHS (368.8 mg, 3.20 mmol) was added to a solution of 4-

(phenylazo) benzoic acid (601 mg, 2 mmol) in THF (20 mL), and the mixture was stirred. Subsequently, DCC (659.9 mg, 3.20 mmol) was added, and the mixture was stirred overnight at room temperature. After the reaction, dichloromethane (DCM, 20 mL) was added, and the solution was washed sequentially with DI water (40 mL), saturated aqueous $NaHCO_3$, and saturated aqueous NaCl (brine). The organic phase was dried over anhydrous Na_2SO_4, filtered, and concentrated under vacuum.

The crude product was purified through column chromatography using ethyl acetate and hexane as the solvents. After chromatography, the solvent was evaporated, and the resulting orange powder was dissolved in ethyl acetate (100 mL) and stored at 4 °C overnight. The white precipitate formed was removed by filtration. Finally, the solvent was evaporated from the filtrate to obtain *N*-succinimidyl-4-(phenylazo)benzoate as an orange powder (653.3 mg, 76%). ^{1}H NMR (400 MHz, DMSO-d_6): δ 8.33 (d, J = 8.8 Hz, 2H, Ar-H *ortho* to CO), 8.10 (d, J = 8.8 Hz, 2H, Ar-H *ortho* to N=N), 7.99 (d, J = 7.6 Hz, 2H, Ar-H *ortho* to N=N), 7.68–7.65 (m, 3H, Ar-H *meta/para*), 2.93 (s, 4H, NHS-CH_2) ppm (Figure 4-2).

2.4.2 Synthesis of *N*-(2-aminoethyl)-4-(2-phenyldiazenyl)benzamide

Although a previous study reported the synthesis of this compound via a pentafluorophenyl ester intermediate [215], the following procedure was adopted here. A solution prepared by dissolving *N*-succinimidyl-4-(phenylazo)benzoate (200 mg, 0.62 mmol) in anhydrous THF (10 mL) was introduced dropwise into a solution of EDA (2 mL) in anhydrous THF (20 mL). The reaction mixture was agitated overnight at ambient temperature. Subsequently, the mixture was diluted with DCM (20 mL) and washed twice with an aqueous NaOH solution (30 mL, adjusted to pH 12). The solvent was evaporated under reduced pressure, and the residue was dried in vacuo overnight to yield the final product (136.1 mg, 82% yield). ^{1}H NMR (400 MHz, DMSO-d_6): δ 8.60 (t, J = 5.6 Hz, 1H, CONH), 8.07 (d, J = 8.5 Hz, 2H, Ar-H *ortho* to amide), 7.96 (d, J = 8.5 Hz, 4H, Ar-H *ortho* to N=N), 7.64–7.61 (m, 3H, Ar-H *meta/para*), 3.31 (q, J = 6.0 Hz,

2H, -CH_2-NHCO-), 2.71 (t, J = 6.5 Hz, 2H, -CH_2-NH_2) ppm (Figure 4-2).

2.4.3 Synthesis of AzoBAM-2k, 4k, 8k

The synthetic pathway for AzoBAM is depicted in Scheme 1; the comprehensive procedures are detailed in the Supplementary Materials. The solutions were prepared by dissolving BAM-NHS (200.8 mg for 2k, 203.3 mg for 4k, and 202.3 mg for 8k) in 10 mL of anhydrous THF. To these solutions, 1.2 equivalents of *N*-(2-aminoethyl)-4-(2-phenyldiazenyl)benzamide (30.3 mg, 15.5 mg, and 8.1 mg for the 2k, 4k, and 8k variants, respectively) were introduced. The reaction mixtures were agitated overnight at ambient temperature. Afterward, each mixture was diluted with DCM (10 mL) and subjected to sequential washing with saturated aqueous $NaHCO_3$ and brine. The organic layers were dried over anhydrous Na_2SO_4, filtered, and concentrated in vacuo. For purification, the crude solids were re-dissolved in anhydrous DCM (2 mL) and precipitated into cold diethyl ether (50 mL, maintained at 0 °C). The final orange solids were collected via filtration and dried under vacuum (Yields: AzoBAM-2k: 136.4 mg, 63%; 4k: 129.2 mg, 61%; 8k: 135.4 mg, 65%).

AzoBAM-2k

^{1}H NMR (400 MHz, DMSO-d_6): δ 8.66 (br s, 1H, CONH), 8.06 (d, J = 8.8 Hz, 2H, Ar-H), 7.95 (d, J = 8.8 Hz, 2H, Ar-H), 7.65–7.60 (m, 3H, Ar-H), 5.33–5.30 (m, 2H, Oleyl -CH=CH-), 4.10 (t, J = 5.2 Hz, 2H, -CH_2-OCO-), 3.51 (br s, 171H, PEG -CH_2-), 2.37 (t, J = 7.2 Hz, 2H, -CH_2-CONH-), 1.98 (m, 4H, Oleyl allylic), 1.46–1.23 (m, 22H, Oleyl -CH_2-), 0.85 (t, J = 6.8 Hz, 3H, -CH_3).

AzoBAM-4k

^{1}H NMR (400 MHz, DMSO-d_6): δ 8.66 (t, 1H, CONH), 8.05 (d, J = 8.8 Hz, 2H, Ar-H), 7.96 (d, J = 8.8 Hz, 2H, Ar-H), 7.63–7.61 (m, 3H, Ar-H), 5.33–5.31 (m, 2H, Oleyl -CH=CH-), 4.10 (t, J = 4.8 Hz, 2H, -CH_2-OCO-), 3.51 (br s, 358H, PEG -CH_2-), 2.37 (t, J = 7.0 Hz, 2H, -CH_2-CONH-), 1.99–1.97 (m, 4H, Oleyl allylic), 1.47–1.23 (m, 26H, Oleyl -CH_2-), 0.85 (t, J =

6.9 Hz, 3H, -CH_3).

AzoBAM-8k

^{1}H NMR (400 MHz, DMSO-d_6): δ 8.66 (t, 1H, CONH), 8.05 (d, J = 8.7 Hz, 2H, Ar-H), 7.96 (d, J = 8.8 Hz, 2H, Ar-H), 7.65–7.61 (m, 3H, Ar-H), 5.33–5.31 (m, 2H, Oleyl -CH=CH-), 4.10 (t, J = 4.8 Hz, 2H, -CH_2-OCO-), 3.51 (br s, 746H, PEG -CH_2-), 2.37 (t, J = 7.0 Hz, 2H, -CH_2-CONH-), 1.99–1.97 (m, 4H, Oleyl allylic), 1.47–1.24 (m, 26H, Oleyl -CH_2-), 0.85 (t, J = 6.9 Hz, 3H, -CH_3).

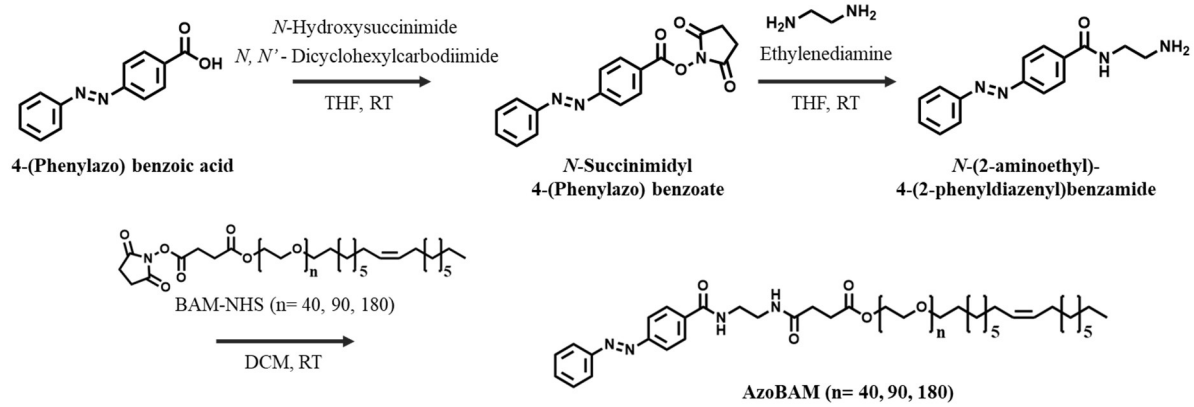

Scheme 1. Synthesis of AzoBAM.

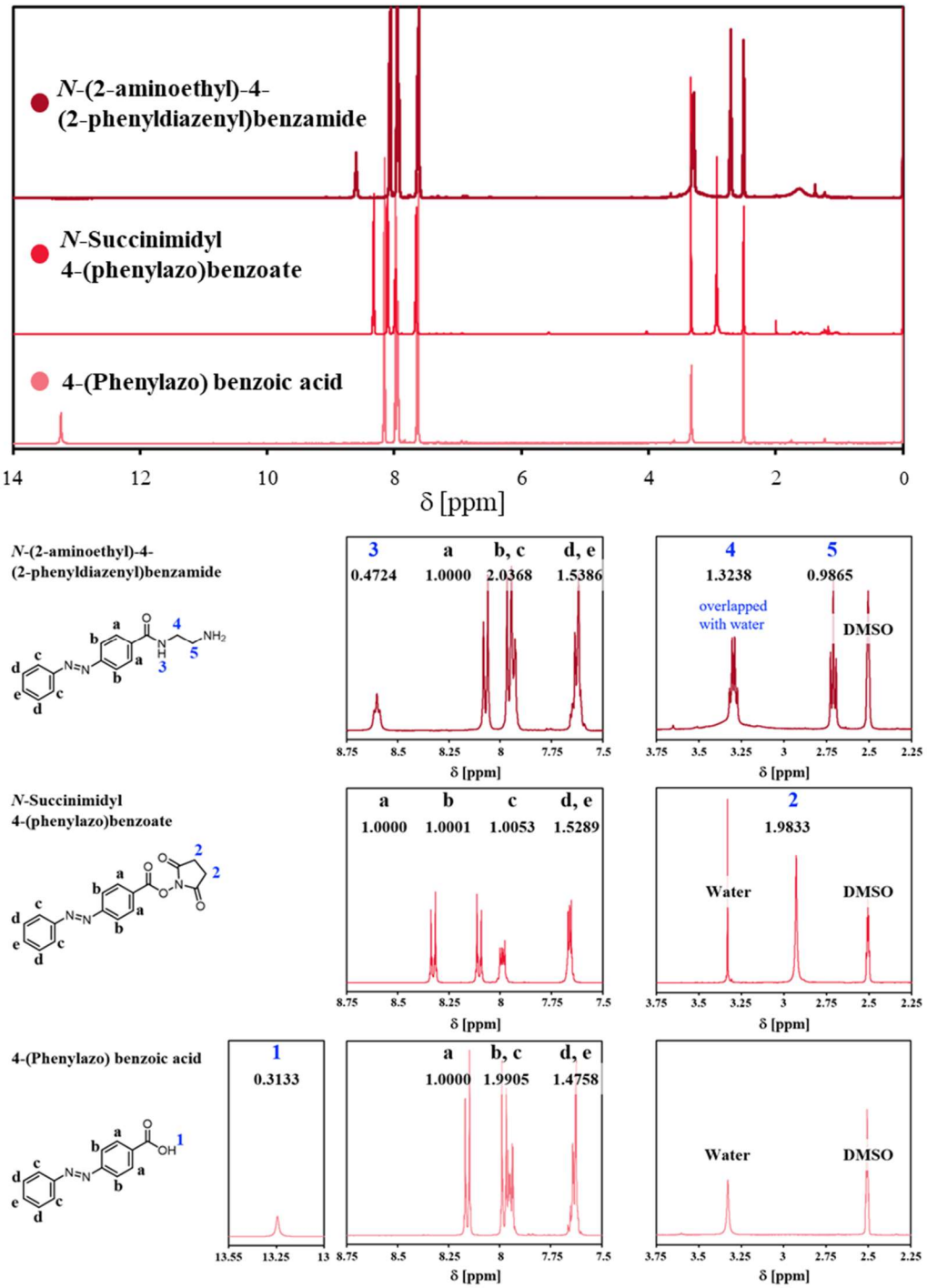

Figure 4-2. Expanded ^{1}H NMR spectra of 4-(phenylazo)benzoic acid, *N*-succinimidyl 4-(phenylazo)benzoate, and *N*-(2-aminoethyl)-4-(2-phenyldiazenyl)benzamide. Integration values are shown in the graphs.

2.5 Photoisomerization of AzoBAM Molecules

AzoBAM variants (2k, 4k, and 8k) were diluted from a 10 mM DMSO stock solution by adding PBS to reach a final concentration of 100 μM. In the photoisomerization experiments,

200 μL aliquots were utilized. Initially, we determined the irradiation time needed for full *trans*-to-*cis* (365 nm) and *cis*-to-*trans* (450 nm) conversions by tracking the absorbance spectral changes (Figure 4-3(a)). To test the reversibility and stability of this switching, the samples were subjected to alternating cycles of 365 nm and 450 nm light, with each exposure lasting 90 s to ensure complete isomerization (Figure 4-3(b)).

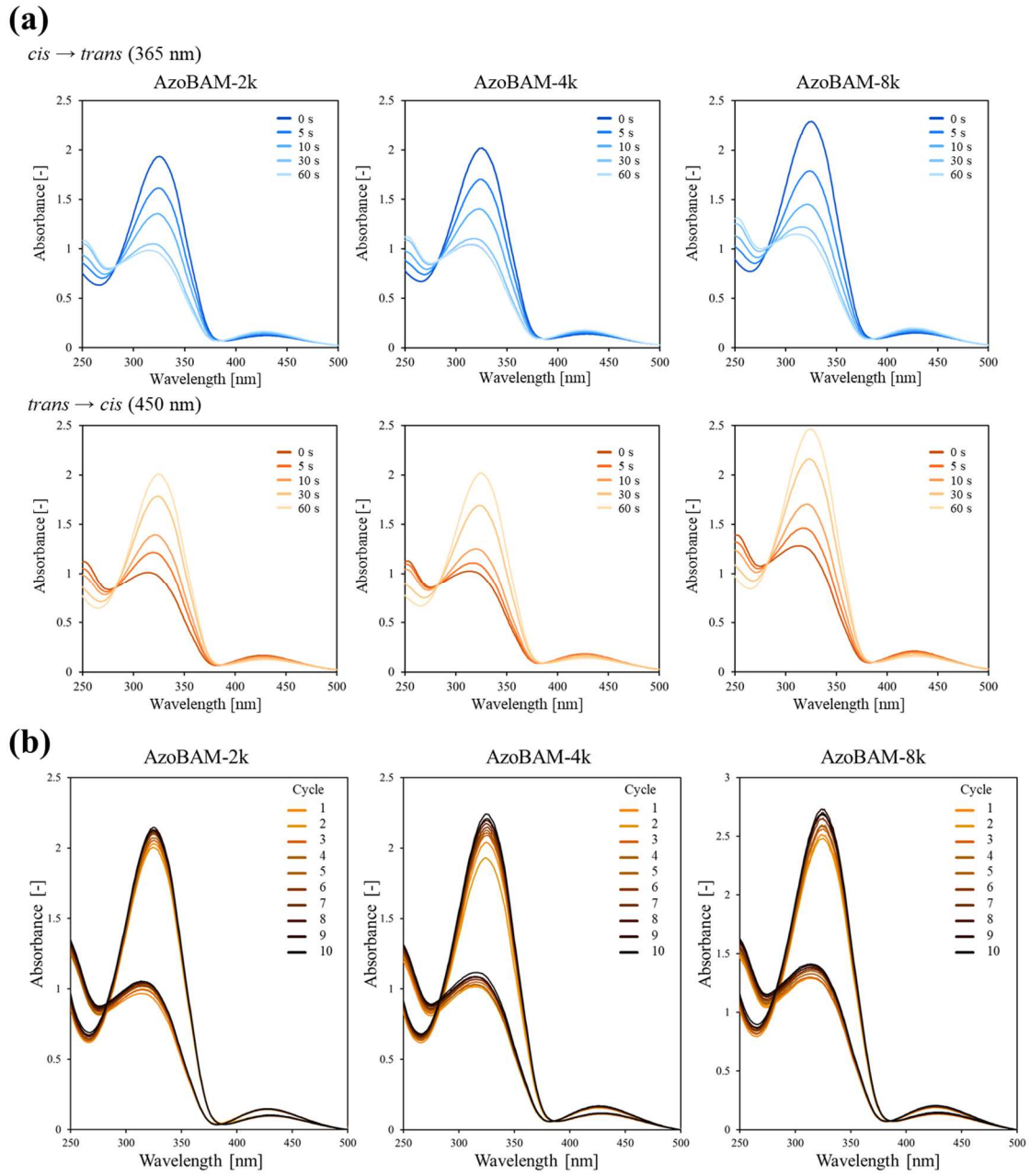

Figure 4-3. (a) UV-vis absorption spectra monitoring the photoisomerization of AzoBAM. The upper and lower panels display the *trans*-to-*cis* and *cis*-to-*trans* conversions, respectively. Measurements were taken following irradiation intervals of 0, 5, 10, 30, and 60 s. (b)

Reversibility of the photoisomerization process demonstrated over 20 consecutive cycles for AzoBAM-2k, 4k, and 8k (arranged from left to right). Isomerization from *trans* to *cis* was driven by 365 nm light (16.6 W/m²), whereas the reverse *cis*-to-*trans* reaction was triggered by 450 nm light (157 W/m²). The absorbance data were acquired after 60 s of exposure for each state.

2.6 Cell Culture and AzoBAM Modification

K562 cells were cultured in RPMI 1640 medium containing 10% FBS, 2 mM L-glutamine, and 100 U/mL streptomycin under a humidified atmosphere of 5% CO_2 at 37 °C. To modify the cell surface, the cells were collected and resuspended in PBS. AzoBAM was then added from a 10 mM DMSO stock solution to attain the final concentrations of 5, 10, 20, or 50 μM. The suspension was incubated at 37 °C for 5 min to facilitate membrane insertion. Finally, the cells were washed twice with PBS to eliminate any unbound AzoBAM.

2.7 Single-Cell Adhesion Force Measurements

Cell adhesion forces were quantified using a microhand micromanipulation system by following previously established protocols [137]. To minimize nonspecific interaction with the tool, the end-effector tips were coated with a 1.0% (w/v) BSA solution for 1 h prior to use. During the experiment, the needle-shaped tips were inserted into a single substrate-adhered cell. The cell was then pulled vertically away from the surface (Figure 4-10(a)), and the adhesion force was defined as the peak reaction force observed during the detachment (Figure 4-10(b)).

2.8 Evaluation of Photocontrolled Cell Adhesion

K562 cells were collected by centrifugation (1800 rpm, 2 min) using an Eppendorf Himac Technologies centrifuge (CT15RE T15A61) and rinsed three times with PBS. For fluorescent labeling, the cells were incubated with Calcein-AM (diluted 1:500 in PBS from a 1 mg/mL DMSO stock) at 37 °C for 30 min. After removing the dye with a PBS wash, surface modification with AzoBAM was performed as outlined in Section 2.6. The modified cells were washed twice, resuspended to a density of 5.0×10^5 cells/mL, and seeded onto CD-glass

substrates. Following a 30 min incubation at 37 °C and three PBS washes, the cells were imaged using a fluorescence microscope (BZ-X800L, Keyence Co.). To trigger detachment, the substrate was exposed to 365 nm light for 1 min, followed by three additional washes. The remaining adherent cells were visualized using a 10× objective, and the cell density was quantified by manually counting the cells in five separate fields using ImageJ software.

2.9 Preparation of BAM-Functionalized Substrates

The glass substrates were initially immersed in a 1.0% (w/v) BSA solution overnight at room temperature to form a blocking layer. For surface functionalization, the working solutions of the BAM-NHS variants (2k, 4k, and 8k) were prepared at 100 μM by diluting 10 mM DMSO stocks with PBS. The BSA-coated substrates were rinsed with PBS and incubated with the BAM-NHS solution for 1 h at 37 °C. This process facilitates the covalent attachment of lipid anchors to the BSA layer via the reaction between NHS esters and amino groups. Following five PBS washes to eliminate unreacted reagents. K562 cells, suspended in PBS, were seeded onto the modified surface and allowed to adhere for 20 min at room temperature. Finally, single-cell adhesion forces were quantified as detailed in Section 2.7.

2.10 Isothermal Titration Calorimetry

Isothermal titration calorimetry (ITC) measurements were conducted using a MicroCal PEAQ-ITC system (Malvern Panalytical) at a temperature of 25 °C. Samples of the AzoBAM variants (2k, 4k, and 8k) prepared in PBS were loaded into the calorimetric cell, and a 5 mM solution of β-CD in the same buffer was placed in the titration syringe. The injection sequence involved a preliminary injection of 0.4 μL, followed by 18 successive injections of 2.0 μL. An interval of 150 s was applied between the injection to ensure thermal equilibrium along with a constant stirring speed of 750 rpm. Data analysis and integration were executed using the MicroCal PEAQ-ITC Analysis Software. Quantitative fitting to a standard binding model was omitted because the AzoBAM-4k variant exhibited complex thermal profiles and AzoBAM-2k

showed negligible heat evolution; instead, a qualitative analysis of the integrated enthalpy trends was conducted.

2.11 Cytotoxicity Test

A suspension of K562 cells was dispensed into a 24-well plate at a volume of 800 μL per well. The samples were subjected to UV irradiation (365 nm; 16.6 W/m²) for periods of 0, 1, and 5 min. The cell viability and proliferation were assessed immediately (0 h) and 24 h post-exposure. For the analysis, the cells were washed twice with PBS and subsequently stained using a 1:500 dilution of Calcein-AM and PI in PBS. Live and dead cells were identified by green and red fluorescence, respectively, allowing for the quantification of cell viability and density.

3. Results and Discussion

3.1 Surface Modification and Characterization

The surface modification protocol for CD-glass substrates is illustrated in Figure 4-4(a). We confirmed the stepwise functionalization using water contact angle measurements and surface zeta potential analysis. As depicted in Figure 4-4(b), treating the bare glass with 3-glycidyloxypropyltrimethoxysilane (GPS) caused a significant rise in the water contact angle, reflecting a loss of hydrophilicity owing to the introduction of epoxy groups. The subsequent immobilization of the hydrophilic β-CD moieties, selected to prevent nonspecific inclusion of the PEG linker owing to cavity size mismatch [216], restores the wettability, resulting in a reduced contact angle. In terms of surface charge, the zeta potential showed a progressive shift toward neutrality with each step (Figure 4-4(c)). Bare glass initially displayed a strong negative potential attributed to deprotonated silanol groups (–Si–O$^-$). The GPS layer masked these charges with neutral epoxide groups, resulting in a positive shift. Grafting electrically neutral β-CD further shifted the potential toward 0 mV. This suggests that β-CD molecules effectively shield residual silanol groups not covered by the GPS layer. Together, these physicochemical

data validate the successful fabrication of the CD-glass substrates.

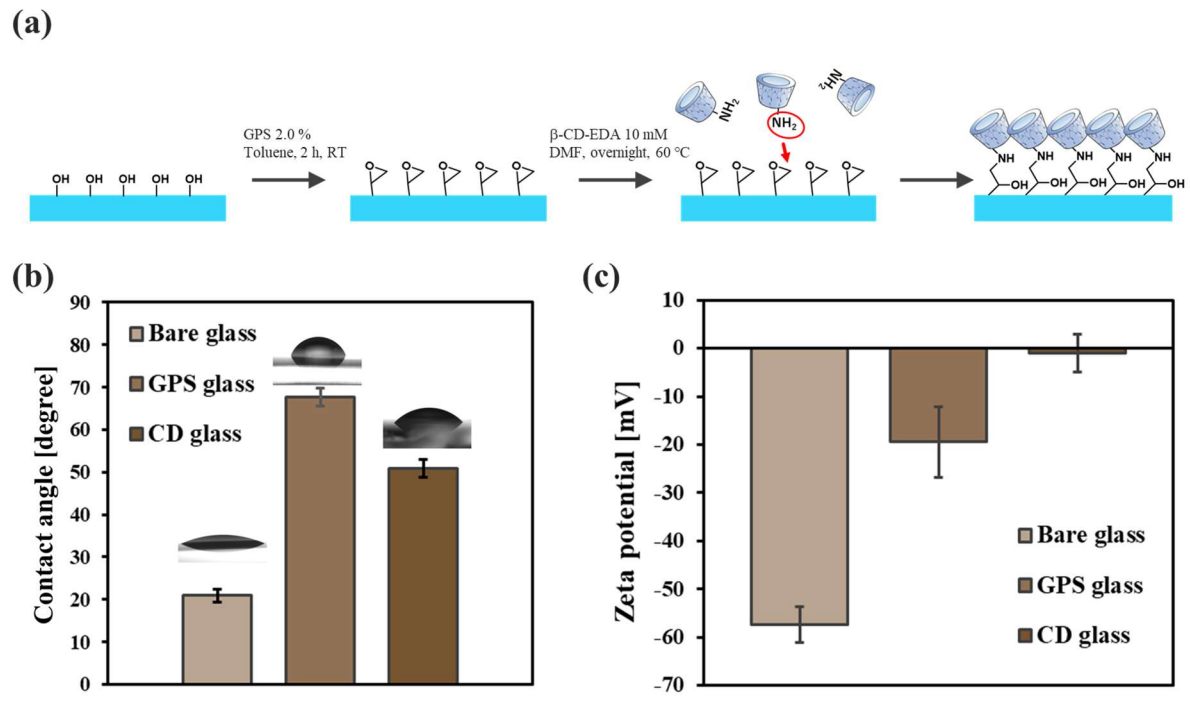

Figure 4-4. (a) Schematic of the glass surface modification process. The red arrow indicates the nucleophilic attack of the amino group of the β-cyclodextrin (β-CD) derivative on the epoxy group of 3-glycidyloxypropyltrimethoxysilane (GPS). (b) Water contact angles of bare glass, GPS modified glass, and β-CD modified glass (CD-glass). (c) Surface zeta potentials of bare glass, GPS modified glass, and CD-glass. Error bars represent standard error (n = 3).

3.2 Synthesis and Photoresponsive Properties of AzoBAM

AzoBAM linkers were prepared via a two-step conjugation protocol (Scheme 1). Initially, 4-(phenylazo)benzoic acid was reacted with ethylenediamine to generate an amine-reactive intermediate. This precursor was then coupled with BAM-NHS to produce the AzoBAM variants (2k, 4k, and 8k). Structural confirmation was obtained using ^{1}H NMR spectroscopy, where characteristic aromatic proton signals in the 7.6–8.1 ppm range validated the successful conjugation (Figure 4-5(a)). The photochromic properties were subsequently analyzed using UV-vis spectroscopy. Exposure to 365 nm light caused a marked reduction in the *trans*-isomer absorption peak at 325 nm, concurrent with the emergence of a *cis*-isomer band at 429 nm. This transition achieved a photostationary state within 60 s (Figure 4-5(b)). The process proved

to be fully reversible; irradiation with 450 nm light restored the *trans* state within the same timeframe. Furthermore, cyclic irradiation experiments (alternating 365/450 nm) demonstrated excellent fatigue resistance, with the absorbance at 325 nm showing consistent reversible switching without degradation (Figure 4-5(c)). Although a slight increase in the absorbance intensity was observed over the cycles, this was attributed to an increase in concentration caused by solvent evaporation during prolonged measurements, as the spectral shape remained unchanged (Figure 4-3(b)).

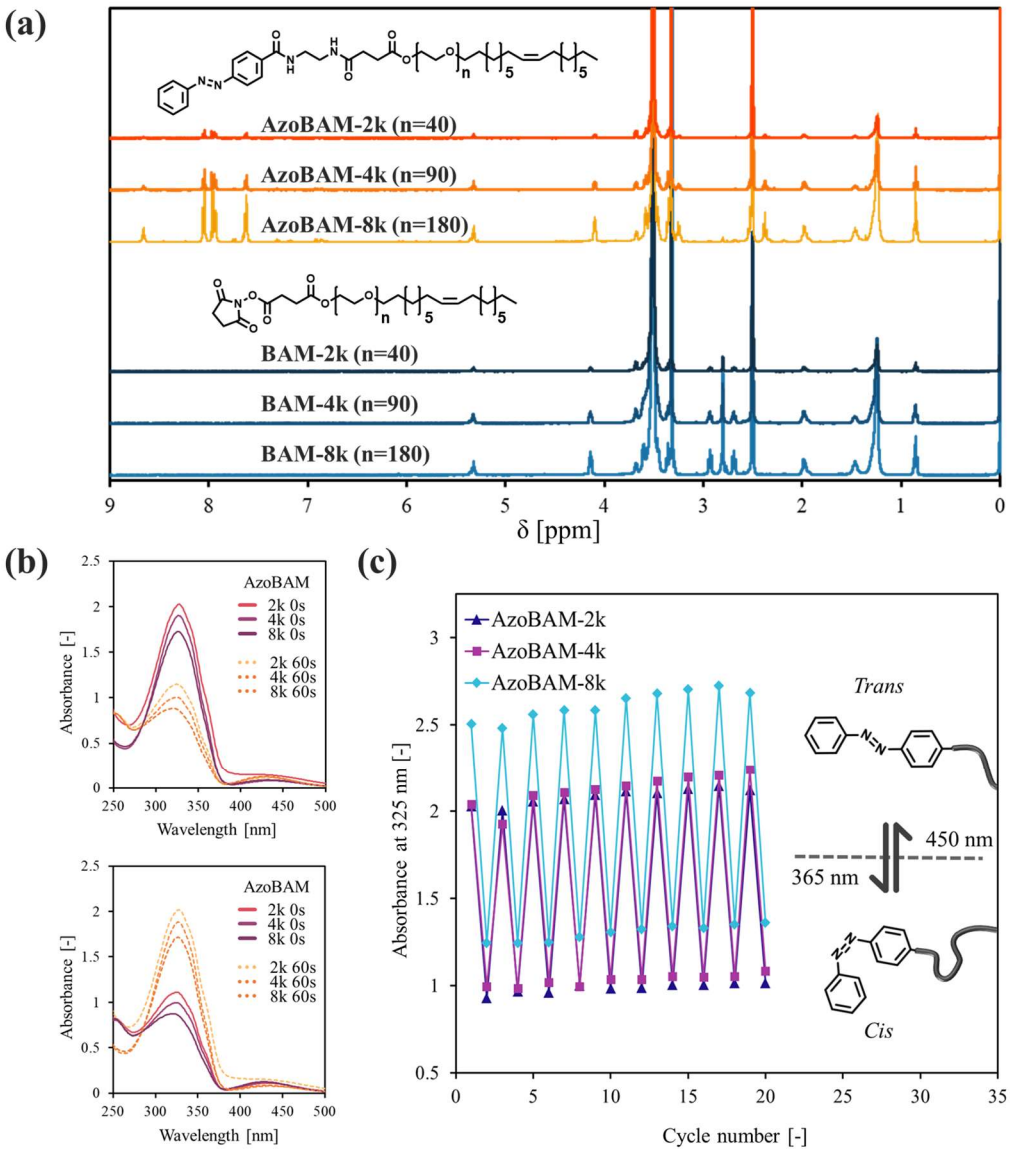

Figure 4-5. (a) ^{1}H NMR spectra of BAM and AzoBAM variants (2k, 4k, and 8k). (b) UV-vis absorbance spectra showing the photoisomerization of AzoBAM. The top graph shows the

trans-to-*cis* transition under 365-nm irradiation (16.6 W/m²), and the bottom graph shows the *cis*-to-*trans* transition under 450-nm irradiation (157 W/m²). In both panels, solid and dashed lines indicate the spectra before (0 s) and after (60 s) irradiation, respectively. (c) Cyclic photoisomerization monitored by changes in absorbance at 325 nm during alternating irradiation with 365- and 450-nm light.

3.3 Cell Adhesion Control via Host–Guest Interaction

Initially, we examined the interaction between unmodified cells and CD-glass to establish a negative control. Contrary to expectations, significant nonspecific adhesion was observed. This is likely attributable to the host-guest complexation capabilities of CD with endogenous cell surface molecules, such as lipids and proteins [217, 218]. We further assessed whether UV irradiation influenced this background binding (Figure 4-8(a)). The results showed that cell retention was 92.4% without irradiation and 88.2% with 365 nm exposure (Figure 4-8(b)). The marginal difference confirms that UV light by itself does not trigger significant detachment. We also confirmed that the applied irradiation (1 min) had no significant effect on the cell viability and proliferation rate after 24 h (Figure 4-6(a,b)).

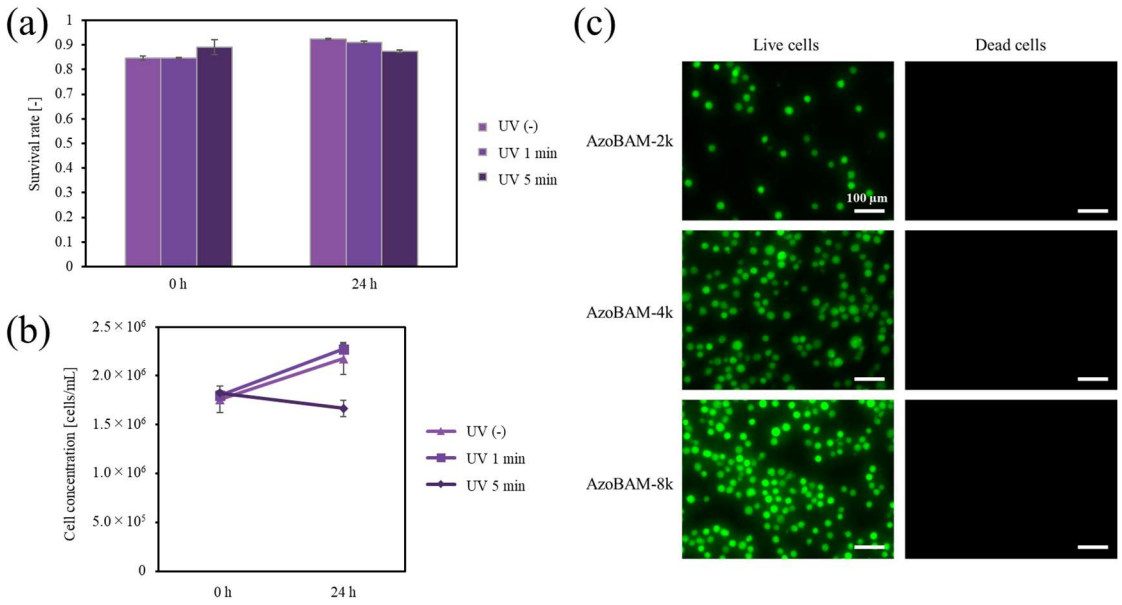

Figure 4-6. Assessment of cytotoxicity induced by UV exposure. (a) Cell viability and (b) cell density quantified at 0 and 24 h post-irradiation. Survival rates were equivalent across all exposure durations (0, 1, and 5 min). In contrast, although the 1 min irradiation group exhibited growth comparable to that of the non-irradiated control (0 min), the 5 min group displayed suppressed proliferation after 24 h. (c) Investigation of acute membrane integrity in preliminary

trials. Fluorescence micrographs of cells post-AzoBAM treatment are shown. Left: Viable cells stained with Calcein-AM (green). Right: Non-viable cells stained with propidium iodide (PI) (red). The lack of prominent PI fluorescence suggests minimal acute membrane damage under the experimental conditions. Scale bars: 100 μm.

This study confirmed that short-term UV exposure is cytocompatible. However, transitioning to visible or near-infrared (NIR) light would significantly expand the biological applicability of the system. These longer wavelengths provide superior tissue penetration and present an even lower risk of phototoxicity than that of UV radiation. Given that recent literature has demonstrated effective photocontrol using azobenzene derivatives responsive to visible and NIR light [219-222], integrating such moieties into the AzoBAM architecture constitutes a promising avenue for future development.

Next, we analyzed the specific adhesion of cells modified with the AzoBAM variants (Figure 4-7). For AzoBAM-2k, adhesion peaked at a 10 μM modification concentration, allowing for effective UV-induced detachment. However, at 5 μM, the cells adhered but could not be detached, suggesting that the short chain and sparse coverage were insufficient to override nonspecific forces. AzoBAM-4k and -8k achieved maximal adhesion at 10 and 20 μM, respectively (with successful detachment at all concentrations), but the 4k variant consistently exhibited the lowest overall adhesion efficiency. To assess the reversible nature of the platform, a cyclic experiment comprising attachment, detachment, and subsequent re-attachment was conducted using the optimized AzoBAM concentration of 10 μM. The data presented in Figure 4-8(c) reveal a substantial re-adhesion efficiency, confirming that AzoBAM-driven cell adhesion can be regulated in a fully reversible manner.

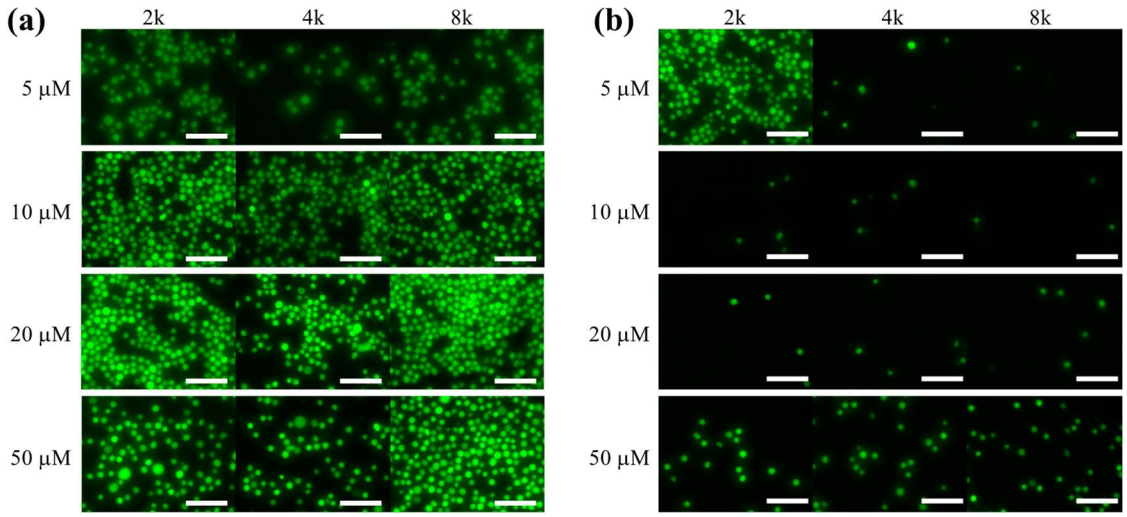

Figure 4-7. Fluorescence microscopy images of cell adhesion for all AzoBAM variants (2k, 4k, 8k) at various concentrations (5, 10, 20, and 50 μM). (a) Adhered cells before UV irradiation. (b) Remaining cells after irradiation with 365 nm light for 1 min, followed by washing. Green fluorescence indicates live cells stained with Calcein-AM. Scale bars represent 50 μm.

We attribute this counterintuitive finding to polymer chain conformation. Adhesion depends on the probability of the tethered polymer extending to bridge the gap to the substrate [223]. A collapsed conformation reduces this probability. Based on prior research on BAM-modified nanoparticles, which showed a non-monotonic size trend (8k > 2k > 4k) [224], we hypothesize that AzoBAM-4k adopts the most compact equilibrium conformation. Corroborating this perspective, our ITC data revealed that the 4k variant possesses a greater propensity for aggregation or molecular compaction in solution relative to the 8k variant (Figure 4-9). This observation is consistent with the trends described in previous literature [224], lending weight to the hypothesis that AzoBAM-4k assumes a collapsed conformation on the cell membrane. Such structural compactness likely hinders the spontaneous chain extension necessary to bridge the cell–substrate interface. As a result, the diminished likelihood of the terminal azobenzene moiety contacting the substrate leads to the minimal adhesion efficiency recorded for AzoBAM-4k (Figure 4-8(d)).

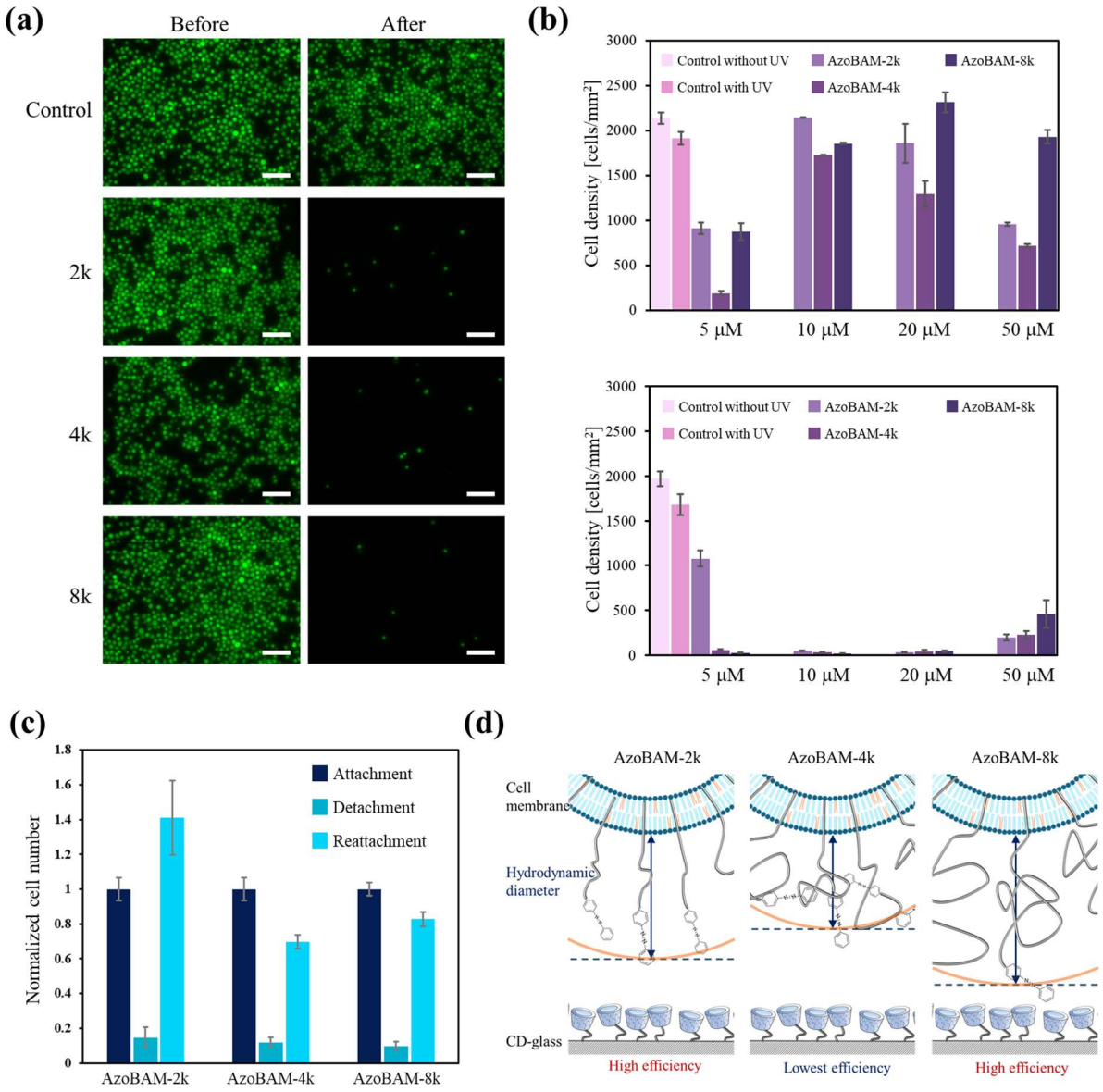

Figure 4-8. (a) Fluorescence images demonstrating photocontrolled cell adhesion. Representative images of unmodified control cells and cells modified with AzoBAM (10 μM). Scale bars represent 100 μm. (b) Cell adhesion efficiency at various AzoBAM concentrations. Top and bottom panels show the cell densities before and after UV irradiation (365 nm), respectively. (c) Quantification of adhered cells in each stage of the attachment, detachment, and re-attachment sequence. Measurements were conducted using 10 μM AzoBAM, with cell counts normalized relative to the initial attachment level. Error bars represent the standard error (n = 5). (d) Schematic of the molecular spreading of AzoBAM variants on the cell membrane. The highly compact 4k variant exhibits the lowest adhesion efficiency because of its limited physical reach to the substrate. The arrow indicates the hydrodynamic diameter.

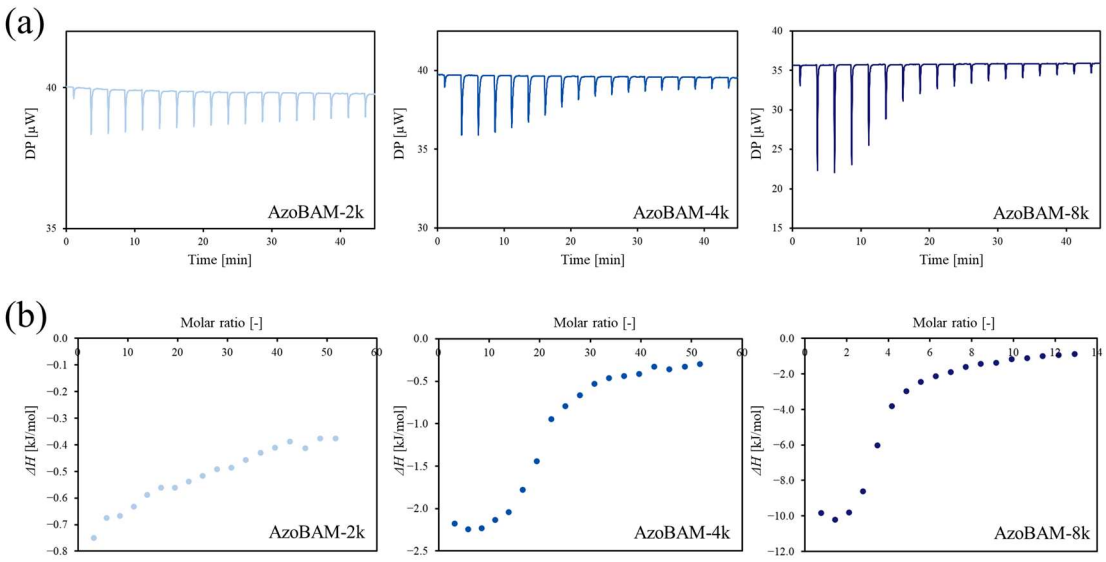

Figure 4-9. Isothermal titration calorimetry (ITC) analysis of the interaction between β-CD and AzoBAM variants. Panels display (a) raw thermograms (differential power vs. time) and (b) integrated enthalpy plots (heat change vs. molar ratio) obtained by titrating β-CD into the AzoBAM variant (2k, 4k, 8k) solution at 25°C. Notably, AzoBAM-2k exhibited minimal heat evolution, suggesting an absence of specific binding attributable to stable micelle formation. Conversely, AzoBAM-8k demonstrated distinct exothermic peaks, indicative of the unhindered binding of free polymer chains. The AzoBAM-4k variant showed lower exothermic heat relative to the 8k variant, implying an energetic cost associated with the competition between host–guest binding and de-aggregation. Curve fitting was omitted owing to the complexity of the thermal profiles.

3.4 Single-Cell Adhesion Force Measurement

We employed a microhand system to quantify the adhesion forces in two distinct configurations (Figures 4-10(a,b)): the photocontrollable AzoBAM system (AzoBAM-modified cells on CD-glass) and BAM control system (unmodified cells on BAM-functionalized glass, mediated by hydrophobic insertion; Figure 4-10(c)). To validate our setup, we first tested the BAM-2k variant. The obtained force (59.5 ± 5.4 nN, n = 15) aligned well with the reported literature values (~60–80 nN) [64]. Profiling the full control series revealed a specific trend: BAM-4k (133.8 ± 15.9 nN, n = 12) > BAM-8k (117.2 ± 19.6 nN, n = 17) > BAM-2k.

Subsequently, the AzoBAM variants (10 μM) were evaluated. AzoBAM-4k yielded the highest force (93.5 ± 18.2 nN, n = 5) similar to that of the control. However, unlike the trend shown by the control, AzoBAM-8k exhibited the weakest adhesion (28.7 ± 2.4 nN, n = 6),

lower than the intermediate AzoBAM-2k value (52.9 ± 13.2 nN, n = 7). A comparison with the BAM controls offered key insights into the effect of the PEG linker.

We observed a molecular weight-dependent reduction in force retention, most notably in the 8k variant. This suggests that steric hindrance from the bulky polymer chain is likely the primary limiting factor for longer chains. Regarding the shorter AzoBAM-2k, we hypothesize that its reduced adhesion is due to the dense topography of the cell surface. Specifically, we postulate that the azobenzene moiety in AzoBAM-2k may be shielded by the glycocalyx layer. Given that the thickness of the K562 glycocalyx is likely comparable to the length of the 2k PEG chain[218], the terminal functional group might fail to effectively penetrate this crowded surface layer to reach the substrate. Consequently, we infer that AzoBAM-4k represents the optimal balance, possessing sufficient length to extend beyond the glycocalyx while minimizing the steric interference observed in the 8k variant.

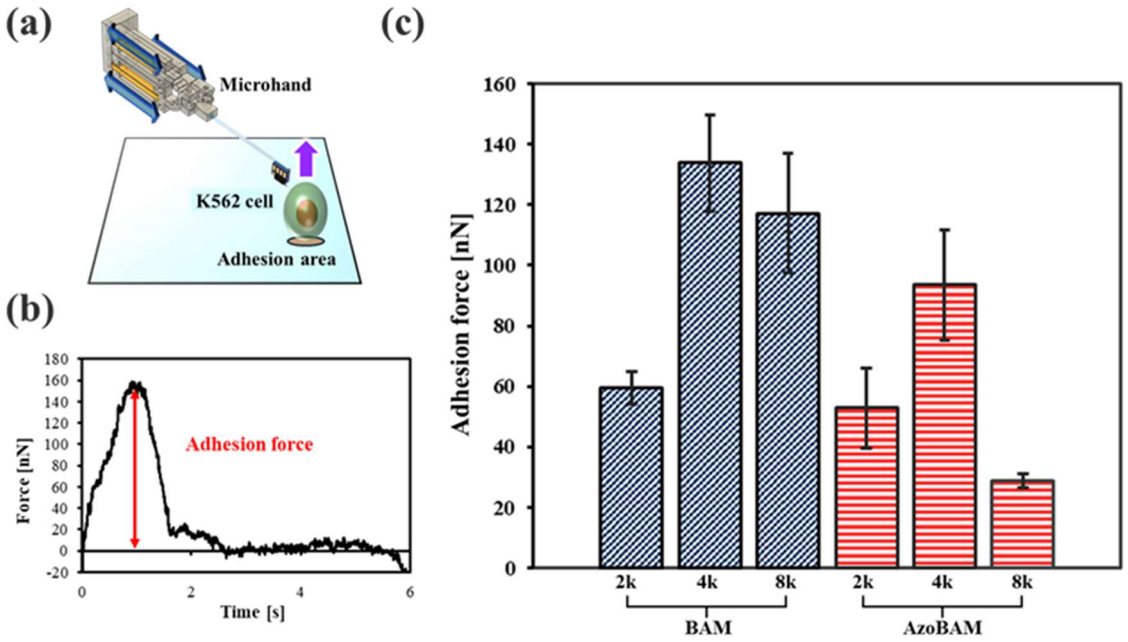

Figure 4-10. (a) Schematic of single-cell adhesion force measurement using a microhand system. The needle-shaped end-effector was inserted into the cell and retracted vertically. (b) Representative force-time curve obtained from the measurements. The maximum peak indicates the adhesion force. (c) Adhesion forces for K562 cells in the BAM control system (2k, 4k, 8k; left, $n \geq 12$) and AzoBAM system (10 μM modification with AzoBAM 2k, 4k, 8k; right, $n \geq 5$). Error bars represent standard error.

Integrating the data on adhesion efficiency (Figure 4-8(b)) and adhesion force (Figure 4-10(c)) exposes a distinct inverse correlation across the AzoBAM variants. The 4k variant presents a paradox: although its compact conformation restricts initial reach—resulting in the lowest capture efficiency—it ultimately generates the highest adhesion force by striking an optimal balance between extension and steric constraints. Conversely, the 2k and 8k variants achieve high initial attachment rates but fail to maintain strong adhesive interfaces. This discrepancy highlights a fundamental trade-off governed by the PEG linker length: the conflict between the molecular extension required for contact and the steric hindrance that weakens the bond.

4. Conclusion

In this chapter, we constructed a light-responsive cell adhesion interface by integrating a β-cyclodextrin-modified substrate with AzoBAM, a novel lipid-anchored conjugate synthesized with distinct PEG linker lengths (2k, 4k, and 8k). Using non-adherent K562 cells, we successfully demonstrated not only efficient cell capture and UV-induced detachment but also the capability for reversible adhesion control. These findings validate the effectiveness of targeting the lipid bilayer to achieve dynamic manipulation of non-adherent cell types.

Furthermore, our systematic analysis of the PEG linker design uncovered a pivotal trade-off. We identified the 4k linker as the optimal configuration, achieving a balance between stable membrane retention and reduced steric interference. Significantly, we discovered that the macroscopic adhesion efficiency does not necessarily correspond to the microscopic adhesion force. This insight provides a critical design criterion for future cell surface engineering. Although validated here on planar substrates, the chemical framework established in this study lays a solid foundation for functionalizing micro-manipulation tools, enabling advanced, non-invasive single-cell handling.

Some parts of this thesis, including the text and figures, have been previously published in the journal article “Photocontrol of Non-Adherent Cell Adhesion via Azobenzene–PEG–Lipid/Cyclodextrin Host–Guest Interactions” by Kawakami et al., submitted in the *International Journal of Molecular Sciences*, 2025, 27, 2, (Reference No. 179). These sections are reproduced here with permission from MDPI.

Chapter V

General Conclusions

This dissertation described the development of elemental technologies based on the microhand system for the precise measurement of whole-cell stiffness and manipulation of single cells. Chapter II of the dissertation described the establishment of precise measurement using plate-shaped end-effectors and its biological validation using disease model cells. Chapter III described the construction of an automated system to overcome the limitations of manual manipulation and enhance the throughput. Chapter IV described the development of a photocontrollable reversible cell adhesion system as a fundamental technology for future non-invasive manipulation. The following results were obtained.

In Chapter II, the foundation of the microhand system for stable cell stiffness measurement was established. Through a comparative analysis, the superiority of plate-shaped end-effectors over conventional needle-shaped ones was demonstrated in terms of controllable deformation and measurement stability. By applying this system to HGPS model cells, a distinct high-stiffness cell population was identified in progerin-overexpressing cells, successfully capturing disease-derived mechanical alterations. Furthermore, the viscoelastic properties of the cytoplasm and nucleus were separately evaluated by controlling the indentation conditions. These findings underscore the importance of the end-effector geometry in mechanical studies and confirm the usefulness of the system in detecting pathological mechanical changes. Notably, the system achieved a high measurement throughput of approximately 60 cells/h under skilled operation, significantly surpassing that of conventional contact-based methods.

In Chapter III, the automation of the microhand system to overcome the dependence on operator skill and limited throughput inherent in manual manipulation is discussed. An

automated system integrating simultaneous observations with microscopes of different magnifications was introduced to facilitate cell handling. Evaluation experiments confirmed that the automated system maintains a speed and measurement accuracy equivalent to those of a skilled operator. This result implies that the system eliminates the need for advanced manipulation skills, enabling robust and efficient data collection. This advancement is expected to accelerate the comprehensive analysis of the relationship between cellular mechanical properties and intracellular structures.

In Chapter IV, a cell-type independent photocontrollable adhesion system was developed to address the challenges in physical grasping, such as mechanical stress. Using an azobenzene-conjugated lipid and a cyclodextrin-functionalized substrate, the efficient capture and UV-induced detachment of non-adherent K562 cells were demonstrated. A critical tradeoff was identified in the PEG linker design, where the optimal 4k linker length balanced stable membrane anchorage with minimal steric hindrance. The revealed inverse correlation between adhesion efficiency and adhesion force provides critical design guidelines. These findings could be useful for the future implementation of chemical grasping mechanisms on microhand end-effectors to achieve non-invasive manipulation.

In summary, the objective of this study was achieved through the development and validation of key elemental technologies required for a next-generation single-cell analysis platform. These investigations—ranging from the geometrical optimization of end-effectors and system automation to the establishment of photocontrollable adhesion—collectively provide a robust technological foundation. The findings are expected to contribute to the future realization of a fully integrated, low-invasive microhand system, facilitating the advancement of cellular mechanobiology and study of diseases such as HGPS.

Suggestions for Future Works

Based on the findings of this study, the elemental technologies developed herein—precise manipulation, automation, and photocontrollable adhesion—can be integrated and extended to the following advanced studies.

Development of a Non-invasive "Chemical Grasping" Microhand System

One of the remaining challenges in single-cell manipulation is the mechanical stress induced by physical grasping, particularly in fragile or non-adherent cells. Although the automated system developed in Chapter III improved the throughput, it continues to rely on physical compression. To address this, the integration of the photocontrollable adhesion system established in Chapter IV into the microhand end-effectors is proposed. By functionalizing the surface of the plate-shaped end-effectors (Chapter II) with β-cyclodextrin and introducing AzoBAM to the cell membrane, a "chemical grasping" mechanism can be realized. This approach would allow the microhand to capture and release cells solely through light irradiation, eliminating the need for an excessive compressive force. Such a system would enable the stress-free manipulation of sensitive cells, such as stem cells or floating cancer cells, and facilitate long-term monitoring of the cell behavior without mechanical perturbation. The design guidelines for the PEG linker length identified in Chapter IV will be critical for optimizing the adhesion force on the microhand tips.

Real-time Mechanical Screening and Dynamic Profiling

The automation achieved in Chapter III opens the door not only to high-throughput data collection but also to real-time mechanical analysis. In the current study, post-experiment data processing was performed. Future development should focus on implementing algorithms capable of calculating mechanical parameters, such as Young's modulus and viscoelasticity, instantaneously during the manipulation process.

By establishing such a real-time feedback system, the microhand can function as a

"mechanical cell sorter." For example, based on the stiffness threshold identified in Chapter II (e.g., distinguishing stiff HGPS cells from normal ones), the system can automatically identify, separate, and collect specific cell populations on the spot. Furthermore, extending this platform to perform dynamic mechanical analysis will allow for the acquisition of comprehensive "mechanical fingerprints." Integrating this real-time mechanical profiling with molecular imaging will enable a rapid and precise diagnosis system that links physical cellular states directly to their biological functions.

References

[1] C. Ji, Y. Huang, Durotaxis and negative durotaxis: where should cells go?, Communications Biology 6(1) (2023) 1169.
[2] P.U. Shirke, H. Goswami, V. Kumar, D. Shah, S. Beri, S. Das, J. Bellare, S. Mayor, K.V. Venkatesh, J.R. Seth, "Viscotaxis"-directed migration of mesenchymal stem cells in response to loss modulus gradient, Acta biomaterialia 135 (2021) 356-367.
[3] L. Pieuchot, J. Marteau, A. Guignandon, T. Dos Santos, I. Brigaud, P.-F. Chauvy, T. Cloatre, A. Ponche, T. Petithory, P. Rougerie, Curvotaxis directs cell migration through cell-scale curvature landscapes, Nature communications 9(1) (2018) 3995.
[4] R.K. Sadhu, M. Luciano, W. Xi, C. Martinez-Torres, M. Schröder, C. Blum, M. Tarantola, S. Villa, S. Penič, A. Iglič, A minimal physical model for curvotaxis driven by curved protein complexes at the cell's leading edge, Proceedings of the National Academy of Sciences 121(12) (2024) e2306818121.
[5] J. Park, D.-H. Kim, A. Levchenko, Topotaxis: a new mechanism of directed cell migration in topographic ECM gradients, Biophysical journal 114(6) (2018) 1257-1263.
[6] P.B. Lücker, S. Javaherian, J.P. Soleas, D. Halverson, P.W. Zandstra, A.P. McGuigan, A microgroove patterned multiwell cell culture plate for high‐throughput studies of cell alignment, Biotechnology and bioengineering 111(12) (2014) 2537-2548.
[7] R. Steward Jr, D. Tambe, C.C. Hardin, R. Krishnan, J.J. Fredberg, Fluid shear, intercellular stress, and endothelial cell alignment, American Journal of Physiology-Cell Physiology 308(8) (2015) C657-C664.
[8] C.S. Janota, F.J. Calero-Cuenca, E.R. Gomes, The role of the cell nucleus in mechanotransduction, Current opinion in cell biology 63 (2020) 204-211.
[9] O. Chaudhuri, J. Cooper-White, P.A. Janmey, D.J. Mooney, V.B. Shenoy, Effects of extracellular matrix viscoelasticity on cellular behaviour, Nature 584(7822) (2020) 535-546.
[10] A.J. Engler, S. Sen, H.L. Sweeney, D.E. Discher, Matrix Elasticity Directs Stem Cell Lineage Specification, Cell 126(4) (2006) 677-689.
[11] X. Di, X. Gao, L. Peng, J. Ai, X. Jin, S. Qi, H. Li, K. Wang, D. Luo, Cellular mechanotransduction in health and diseases: from molecular mechanism to therapeutic targets, Signal Transduction and Targeted Therapy 8(1) (2023) 282.
[12] D.E. Ingber, Tensegrity-based mechanosensing from macro to micro, Progress in biophysics and molecular biology 97(2-3) (2008) 163-179.
[13] D.E. Ingber, N. Wang, D. Stamenović, Tensegrity, cellular biophysics, and the mechanics of living systems, Reports on Progress in Physics 77(4) (2014) 046603.
[14] A.D. Bershadsky, C. Ballestrem, L. Carramusa, Y. Zilberman, B. Gilquin, S. Khochbin, A.Y. Alexandrova, A.B. Verkhovsky, T. Shemesh, M.M. Kozlov, Assembly and mechanosensory function of focal adhesions: experiments and models, European Journal of Cell Biology 85(3) (2006) 165-173.
[15] X. Wang, H. Liu, M. Zhu, C. Cao, Z. Xu, Y. Tsatskis, K. Lau, C. Kuok, T. Filleter, H. McNeill, Mechanical stability of the cell nucleus–roles played by the cytoskeleton in nuclear deformation and strain recovery, Journal of cell science 131(13) (2018) jcs209627.
[16] M. Schaks, G. Giannone, K. Rottner, Actin dynamics in cell migration, Essays in biochemistry 63(5) (2019) 483-495.
[17] S.Y. Khaitlina, Intracellular transport based on actin polymerization, Biochemistry (Moscow) 79(9) (2014) 917-927.
[18] D.E. Ingber, Tensegrity: the architectural basis of cellular mechanotransduction, Annual review of physiology 59(1) (1997) 575-599.
[19] P.A. Janmey, U. Euteneuer, P. Traub, M. Schliwa, Viscoelastic properties of vimentin

compared with other filamentous biopolymer networks, Journal of Cell Biology 113(1) (1991) 155-160.
[20] K.E. Kasza, A.C. Rowat, J. Liu, T.E. Angelini, C.P. Brangwynne, G.H. Koenderink, D.A. Weitz, The cell as a material, Current Opinion in Cell Biology 19(1) (2007) 101-107.
[21] K.N. Dahl, A.J.S. Ribeiro, J. Lammerding, Nuclear shape, mechanics, and mechanotransduction, Circulation research 102(11) (2008) 1307-1318.
[22] H. Strickfaden, T.O. Tolsma, A. Sharma, D.A. Underhill, J.C. Hansen, M.J. Hendzel, Condensed Chromatin Behaves like a Solid on the Mesoscale *In Vitro* and in Living Cells, Cell 183(7) (2020) 1772-1784.e13.
[23] V.I.P. Keizer, S. Grosse-Holz, M. Woringer, L. Zambon, K. Aizel, M. Bongaerts, F. Delille, L. Kolar-Znika, V.F. Scolari, S. Hoffmann, Live-cell micromanipulation of a genomic locus reveals interphase chromatin mechanics, Science 377(6605) (2022) 489-495.
[24] F. Rashid, S.A. Kabbo, N. Wang, Mechanomemory of nucleoplasm and RNA polymerase II after chromatin stretching by a microinjected magnetic nanoparticle force, Cell Reports 43(7) (2024) 114462.
[25] J.D. Pajerowski, K.N. Dahl, F.L. Zhong, P.J. Sammak, D.E. Discher, Physical plasticity of the nucleus in stem cell differentiation, Proceedings of the National Academy of Sciences 104(40) (2007) 15619-15624.
[26] M.M. Nava, Y.A. Miroshnikova, L.C. Biggs, D.B. Whitefield, F. Metge, J. Boucas, H. Vihinen, E. Jokitalo, X. Li, J.M. García Arcos, B. Hoffmann, R. Merkel, C.M. Niessen, K.N. Dahl, S.A. Wickström, Heterochromatin-Driven Nuclear Softening Protects the Genome against Mechanical Stress-Induced Damage, Cell 181(4) (2020) 800-817.e22.
[27] M. Crisp, Q. Liu, K. Roux, J.B. Rattner, C. Shanahan, B. Burke, P.D. Stahl, D. Hodzic, Coupling of the nucleus and cytoplasm: Role of the LINC complex, Journal of Cell Biology 172(1) (2005) 41-53.
[28] L.M. Hoffman, M.A. Smith, C.C. Jensen, M. Yoshigi, E. Blankman, K.S. Ullman, M.C. Beckerle, Mechanical stress triggers nuclear remodeling and the formation of transmembrane actin nuclear lines with associated nuclear pore complexes, Molecular biology of the cell 31(16) (2020) 1774-1787.
[29] B. Seelbinder, S. Ghosh, S.E. Schneider, A.K. Scott, A.G. Berman, C.J. Goergen, K.B. Margulies, K.C. Bedi, E. Casas, A.R. Swearingen, J. Brumbaugh, S. Calve, C.P. Neu, Nuclear deformation guides chromatin reorganization in cardiac development and disease, Nature Biomedical Engineering 5(12) (2021) 1500-1516.
[30] Y. Shimamoto, S. Tamura, H. Masumoto, K. Maeshima, Nucleosome–nucleosome interactions via histone tails and linker DNA regulate nuclear rigidity, Molecular biology of the cell 28(11) (2017) 1580-1589.
[31] J. Hatami, M. Tafazzoli-Shadpour, N. Haghighipour, M.A. Shokrgozar, M. Janmaleki, Influence of cyclic stretch on mechanical properties of endothelial cells, Experimental Mechanics 53(8) (2013) 1291-1298.
[32] A. Schoenit, S. Monfared, L. Anger, C. Rosse, V. Venkatesh, L. Balasubramaniam, E. Marangoni, P. Chavrier, R.-M. Mège, A. Doostmohammadi, Force transmission is a master regulator of mechanical cell competition, Nature Materials (2025) 1-11.
[33] V. Swaminathan, K. Mythreye, E.T. O'Brien, A. Berchuck, G.C. Blobe, R. Superfine, Mechanical stiffness grades metastatic potential in patient tumor cells and in cancer cell lines, Cancer research 71(15) (2011) 5075-5080.
[34] S. Kwon, W. Yang, D. Moon, K.S. Kim, Comparison of cancer cell elasticity by cell type, Journal of Cancer 11(18) (2020) 5403.
[35] F.-S. Quan, K.S. Kim, Medical applications of the intrinsic mechanical properties of single cells, Acta Biochimica et Biophysica Sinica 48(10) (2016) 865-871.
[36] S.E. Cross, Y.-S. Jin, J. Rao, J.K. Gimzewski, Nanomechanical analysis of cells from

cancer patients, Nano-enabled medical applications, Jenny Stanford Publishing2020, pp. 547-566.
[37] A.M. Gajda, R. Rodríguez-López, E.E. Er, Targeting cancer cell stiffness and metastasis with clinical therapeutics, Clinical & Experimental Metastasis 42(4) (2025) 34.
[38] K. Tsujita, R. Satow, S. Asada, Y. Nakamura, L. Arnes, K. Sako, Y. Fujita, K. Fukami, T. Itoh, Homeostatic membrane tension constrains cancer cell dissemination by counteracting BAR protein assembly, Nature Communications 12(1) (2021) 5930.
[39] K. Tang, Y. Xin, K. Li, X. Chen, Y. Tan, Cell cytoskeleton and stiffness are mechanical indicators of organotropism in breast cancer, Biology 10(4) (2021) 259.
[40] M. Islam, R. Mezencev, B. McFarland, H. Brink, B. Campbell, B. Tasadduq, E.K. Waller, W. Lam, A. Alexeev, T. Sulchek, Microfluidic cell sorting by stiffness to examine heterogenic responses of cancer cells to chemotherapy, Cell Death & Disease 9(2) (2018) 239.
[41] W.A. Lam, M.J. Rosenbluth, D.A. Fletcher, Chemotherapy exposure increases leukemia cell stiffness, Blood 109(8) (2007) 3505-3508.
[42] X. Mu, C. Tseng, W.S. Hambright, P. Matre, C.Y. Lin, P. Chanda, W. Chen, J. Gu, S. Ravuri, Y. Cui, Cytoskeleton stiffness regulates cellular senescence and innate immune response in Hutchinson–Gilford Progeria Syndrome, Aging Cell 19(8) (2020) e13152.
[43] E.A. Booth, S.T. Spagnol, T.A. Alcoser, K.N. Dahl, Nuclear stiffening and chromatin softening with progerin expression leads to an attenuated nuclear response to force, Soft Matter 11(32) (2015) 6412-6418.
[44] H.D. Kim, M.G. Luthra, R.P. Watts, L.Z. Stern, Factors influencing osmotic fragility of red blood cells in Duchenne muscular dystrophy, Neurology 30(7) (1980) 726-726.
[45] P. Ravishankar, I. Tandon, K. Balachandran, Effect of cyclic uniaxial mechanical strain on endothelial progenitor cell differentiation, Cardiovascular Engineering and Technology 13(6) (2022) 872-885.
[46] S. Ghazanfari, M. Tafazzoli-Shadpour, M.A. Shokrgozar, Effects of cyclic stretch on proliferation of mesenchymal stem cells and their differentiation to smooth muscle cells, Biochemical and biophysical research communications 388(3) (2009) 601-605.
[47] J. Yan, W.-B. Wang, Y.-J. Fan, H. Bao, N. Li, Q.-P. Yao, Y.-L. Huo, Z.-L. Jiang, Y.-X. Qi, Y. Han, Cyclic stretch induces vascular smooth muscle cells to secrete connective tissue growth factor and promote endothelial progenitor cell differentiation and angiogenesis, Frontiers in cell and developmental biology 8 (2020) 606989.
[48] A. Singam, C. Bhattacharya, S. Park, Aging-related changes in the mechanical properties of single cells, Heliyon 10(12) (2024).
[49] B.K. Walther, A.P. Sears, A. Mojiri, R. Avazmohammadi, J. Gu, O.V. Chumakova, N.K.R. Pandian, A. Dominic, J.-L. Martiel, S.K. Yazdani, Disrupted stiffness ratio alters nuclear mechanosensing, Matter 6(10) (2023) 3608-3630.
[50] M. Huse, Mechanical forces in the immune system, Nature Reviews Immunology 17(11) (2017) 679-690.
[51] N. Bufi, M. Saitakis, S. Dogniaux, O. Buschinger, A. Bohineust, A. Richert, M. Maurin, C. Hivroz, A. Asnacios, Human primary immune cells exhibit distinct mechanical properties that are modified by inflammation, Biophysical journal 108(9) (2015) 2181-2190.
[52] T.J. Thauland, K.H. Hu, M.A. Bruce, M.J. Butte, Cytoskeletal adaptivity regulates T cell receptor signaling, Science signaling 10(469) (2017) eaah3737.
[53] R.M. Hochmuth, Micropipette aspiration of living cells, Journal of Biomechanics 33(1) (2000) 15-22.
[54] A.C. Rowat, Physical Properties of the Nucleus Studied by Micropipette Aspiration, in: R. Hancock (Ed.), The Nucleus: Volume 2: Chromatin, Transcription, Envelope, Proteins, Dynamics, and Imaging, Humana Press, Totowa, NJ, 2008, pp. 3-12.
[55] T. Portet, Sharona E. Gordon, Sarah L. Keller, Increasing Membrane Tension Decreases

Miscibility Temperatures; an Experimental Demonstration via Micropipette Aspiration, Biophysical Journal 103(8) (2012) L35-L37.
[56] B. Hogan, A. Babataheri, Y. Hwang, Abdul I. Barakat, J. Husson, Characterizing Cell Adhesion by Using Micropipette Aspiration, Biophysical Journal 109(2) (2015) 209-219.
[57] H. Miyazaki, Y. Hasegawa, K. Hayashi, A newly designed tensile tester for cells and its application to fibroblasts, Journal of Biomechanics 33(1) (2000) 97-104.
[58] H. Miyazaki, Y. Hasegawa, K. Hayashi, Tensile Properties of Contractile and Synthetic Vascular Smooth Muscle Cells, JSME International Journal Series C Mechanical Systems, Machine Elements and Manufacturing 45(4) (2002) 870-879.
[59] Y.-W. Chiou, H.-K. Lin, M.-J. Tang, H.-H. Lin, M.-L. Yeh, The Influence of Physical and Physiological Cues on Atomic Force Microscopy-Based Cell Stiffness Assessment, PLOS ONE 8(10) (2013) e77384.
[60] G. Lamour, M. Malo, R. Crépin, J. Pelta, S. Labdi, C. Campillo, Dynamically Mapping the Topography and Stiffness of the Leading Edge of Migrating Cells Using AFM in Fast-QI Mode, ACS Biomaterials Science & Engineering 10(3) (2024) 1364-1378.
[61] T. Ichikawa, Y. Kono, M. Kudo, T. Shimi, N. Miyashita, T. Maesaka, K. Ishibashi, K. Sivashanmugan, T. Yoshida, K. Miyazawa, R. Hanayama, E. Hirata, K. Miyata, H. Kimura, T. Fukuma, Probing Nanomechanics by Direct Indentation Using Nanoendoscopy-AFM Reveals the Nuclear Elasticity Transition in Cancer Cells, ACS Applied Nano Materials 8(42) (2025) 20239-20249.
[62] G. Weder, N. Blondiaux, M. Giazzon, N. Matthey, M. Klein, R. Pugin, H. Heinzelmann, M. Liley, Use of force spectroscopy to investigate the adhesion of living adherent cells, Langmuir 26(11) (2010) 8180-8186.
[63] G. Weder, O. Guillaume-Gentil, N. Matthey, F. Montagne, H. Heinzelmann, J. Vörös, M. Liley, The quantification of single cell adhesion on functionalized surfaces for cell sheet engineering, Biomaterials 31(25) (2010) 6436-6443.
[64] R. Kawamura, M. Mishima, S. Ryu, Y. Arai, M. Okose, Y.R. Silberberg, S.R. Rao, C. Nakamura, Controlled cell adhesion using a biocompatible anchor for membrane-conjugated bovine serum albumin/bovine serum albumin mixed layer, Langmuir 29(21) (2013) 6429-6433.
[65] H. Kim, A. Yamagishi, M. Imaizumi, Y. Onomura, A. Nagasaki, Y. Miyagi, T. Okada, C. Nakamura, Quantitative measurements of intercellular adhesion between a macrophage and cancer cells using a cup-attached AFM chip, Colloids and Surfaces B: Biointerfaces 155 (2017) 366-372.
[66] A. Yamagishi, M. Mizusawa, K. Uchida, M. Iijima, S.i. Kuroda, K. Fukazawa, K. Ishihara, C. Nakamura, Mechanical detection of interactions between proteins related to intermediate filament and transcriptional regulation in living cells, Biosensors and Bioelectronics 216 (2022) 114603.
[67] S. Ryu, Y. Hashizume, M. Mishima, R. Kawamura, M. Tamura, H. Matsui, M. Matsusaki, M. Akashi, C. Nakamura, Measurement of cell adhesion force by vertical forcible detachment using an arrowhead nanoneedle and atomic force microscopy, Biochemical and Biophysical Research Communications 451(1) (2014) 107-111.
[68] C. Gonnermann, C. Huang, S.F. Becker, D.R. Stamov, D. Wedlich, J. Kashef, C.M. Franz, Quantitating membrane bleb stiffness using AFM force spectroscopy and an optical sideview setup, Integrative biology 7(3) (2015) 356-363.
[69] Y. Yang, M. Li, Side-view optical microscopy-assisted atomic force microscopy for thickness-dependent nanobiomechanics, Nanoscale Advances 6(13) (2024) 3306-3319.
[70] C.M. Hobson, M. Kern, E.T. O'Brien Iii, A.D. Stephens, M.R. Falvo, R. Superfine, Correlating nuclear morphology and external force with combined atomic force microscopy and light sheet imaging separates roles of chromatin and lamin A/C in nuclear mechanics, Molecular biology of the cell 31(16) (2020) 1788-1801.

[71] V. Binyukov, E. Mil, L. Matienko, A. Albantova, A. Goloshchapov, Methodic Approach of Atomic-Force Microscopy (AFM) to Study Morphological Changes of Cells and Model Systems, Micro, 2023, pp. 382-390.
[72] S.M. Haghparast, T. Kihara, J. Miyake, Distinct mechanical behavior of HEK293 cells in adherent and suspended states, PeerJ 3 (2015) e1131.
[73] A. Meister, M. Gabi, P. Behr, P. Studer, J.n. Vörös, P. Niedermann, J. Bitterli, J. Polesel-Maris, M. Liley, H. Heinzelmann, FluidFM: combining atomic force microscopy and nanofluidics in a universal liquid delivery system for single cell applications and beyond, Nano letters 9(6) (2009) 2501-2507.
[74] A.G. Nagy, I. Szekacs, A. Bonyar, R. Horvath, Cell-substratum and cell-cell adhesion forces and single-cell mechanical properties in mono-and multilayer assemblies from robotic fluidic force microscopy, European Journal of Cell Biology 101(4) (2022) 151273.
[75] Á.G. Nagy, N. Kanyó, A. Vörös, I. Székács, A. Bonyár, R. Horvath, Population distributions of single-cell adhesion parameters during the cell cycle from high-throughput robotic fluidic force microscopy, Scientific reports 12(1) (2022) 7747.
[76] X. Xu, J. Jia, M. Guo, The most recent advances in the application of nano-structures/nano-materials for single-cell sampling, Frontiers in Chemistry 8 (2020) 718.
[77] Janina R. Lange, J. Steinwachs, T. Kolb, Lena A. Lautscham, I. Harder, G. Whyte, B. Fabry, Microconstriction Arrays for High-Throughput Quantitative Measurements of Cell Mechanical Properties, Biophysical Journal 109(1) (2015) 26-34.
[78] M. Urbanska, H.E. Muñoz, J. Shaw Bagnall, O. Otto, S.R. Manalis, D. Di Carlo, J. Guck, A comparison of microfluidic methods for high-throughput cell deformability measurements, Nature Methods 17(6) (2020) 587-593.
[79] A. Mietke, O. Otto, S. Girardo, P. Rosendahl, A. Taubenberger, S. Golfier, E. Ulbricht, S. Aland, J. Guck, E. Fischer-Friedrich, Extracting cell stiffness from real-time deformability cytometry: theory and experiment, Biophysical journal 109(10) (2015) 2023-2036.
[80] K.D. Nyberg, K.H. Hu, S.H. Kleinman, D.B. Khismatullin, M.J. Butte, A.C. Rowat, Quantitative Deformability Cytometry: Rapid, Calibrated Measurements of Cell Mechanical Properties, Biophysical Journal 113(7) (2017) 1574-1584.
[81] O. Otto, P. Rosendahl, A. Mietke, S. Golfier, C. Herold, D. Klaue, S. Girardo, S. Pagliara, A. Ekpenyong, A. Jacobi, M. Wobus, N. Töpfner, U.F. Keyser, J. Mansfeld, E. Fischer-Friedrich, J. Guck, Real-time deformability cytometry: on-the-fly cell mechanical phenotyping, Nature Methods 12(3) (2015) 199-202.
[82] D.R. Gossett, H.T.K. Tse, S.A. Lee, Y. Ying, A.G. Lindgren, O.O. Yang, J. Rao, A.T. Clark, D. Di Carlo, Hydrodynamic stretching of single cells for large population mechanical phenotyping, Proceedings of the National Academy of Sciences 109(20) (2012) 7630-7635.
[83] N. Asmare, A.K.M. Arifuzzman, N. Wang, M. Boya, R. Liu, A.F. Sarioglu, High throughput cell stiffness measurement via multiplexed impedance sensors, Biosensors and Bioelectronics 273 (2025) 117158.
[84] J. Chen, X. Zou, D.C. Spencer, H. Morgan, Single-cell electro-mechanical shear flow deformability cytometry, Microsystems & Nanoengineering 10(1) (2024) 173.
[85] A. Ashkin, J.M. Dziedzic, J.E. Bjorkholm, S. Chu, Observation of a single-beam gradient force optical trap for dielectric particles, Optics Letters 11(5) (1986) 288-290.
[86] M.P. Nicholas, L. Rao, A. Gennerich, An Improved Optical Tweezers Assay for Measuring the Force Generation of Single Kinesin Molecules, in: D.J. Sharp (Ed.), Mitosis: Methods and Protocols, Springer New York, New York, NY, 2014, pp. 171-246.
[87] C. Veigel, J.E. Molloy, S. Schmitz, J. Kendrick-Jones, Load-dependent kinetics of force production by smooth muscle myosin measured with optical tweezers, Nature Cell Biology 5(11) (2003) 980-986.
[88] H.M. Nussenzveig, Cell membrane biophysics with optical tweezers, European

Biophysics Journal 47(5) (2018) 499-514.
[89] D. Wang, T. Zhang, J. Shi, Y. Wang, B. Liu, L. Ding, C. Chen, W. Zhang, J. Zheng, J. Chen, Z. Li, R. Deng, X. Shan, F. Wang, Intracellular Manipulation by Particle Swarm Optimized Optical Tweezers, Laser & Photonics Reviews n/a(n/a) (2025) e02473.
[90] A. Blázquez-Castro, Optical Tweezers: Phototoxicity and Thermal Stress in Cells and Biomolecules, Micromachines, 2019, p. 507.
[91] B. del Rosal, P. Haro-González, W.T. Ramsay, L.M. Maestro, K. Santacruz-Gómez, M.C. Iglesias-De La Cruz, F. Sanz-Rodríguez, J.Y. Chooi, P. Rodríguez-Sevilla, D. Choudhury, Heat in optical tweezers, SPIE, pp. 289-296.
[92] J. Guck, R. Ananthakrishnan, H. Mahmood, T.J. Moon, C.C. Cunningham, J. Käs, The Optical Stretcher: A Novel Laser Tool to Micromanipulate Cells, Biophysical Journal 81(2) (2001) 767-784.
[93] C.T. Mierke, The role of the optical stretcher is crucial in the investigation of cell mechanics regulating cell adhesion and motility, Frontiers in cell and developmental biology 7 (2019) 184.
[94] L. Huang, F. Liang, Y. Feng, P. Zhao, W. Wang, On-chip integrated optical stretching and electrorotation enabling single-cell biophysical analysis, Microsystems & Nanoengineering 6(1) (2020) 57.
[95] M. Kreysing, D. Ott, M.J. Schmidberger, O. Otto, M. Schürmann, E. Martín-Badosa, G. Whyte, J. Guck, Dynamic operation of optical fibres beyond the single-mode regime facilitates the orientation of biological cells, Nature communications 5(1) (2014) 5481.
[96] J.H. Kang, T.P. Miettinen, L. Chen, S. Olcum, G. Katsikis, P.S. Doyle, S.R. Manalis, Noninvasive monitoring of single-cell mechanics by acoustic scattering, Nature Methods 16(3) (2019) 263-269.
[97] Y. Yang, W. Pang, H. Zhang, W. Cui, K. Jin, C. Sun, Y. Wang, L. Zhang, X. Ren, X. Duan, Manipulation of single cells via a stereo acoustic streaming tunnel (SteAST), Microsystems & Nanoengineering 8(1) (2022) 88.
[98] Y. Yang, K. Jin, H. Qi, W. Wei, Y. Zhou, C. Sun, X. Chen, Y. Wang, L.P. Lee, X. Duan, Acoustic streaming microgripper for programmable three-dimensional manipulation of single cells, npj Acoustics 1(1) (2025) 19.
[99] X. Liu, Y. Li, F. Liu, Q. Shi, L. Dong, Q. Huang, T. Arai, T. Fukuda, μSonic-hand: Biomedical micromanipulation driven by acoustic gas-liquid-solid interactions, Science advances 11(13) (2025) eads8167.
[100] Y. Wu, A.G. Stewart, P.V.S. Lee, On-chip cell mechanophenotyping using phase modulated surface acoustic wave, Biomicrofluidics 13(2) (2019).
[101] J.Y. Hwang, J. Kim, J.M. Park, C. Lee, H. Jung, J. Lee, K.K. Shung, Cell Deformation by Single-beam Acoustic Trapping: A Promising Tool for Measurements of Cell Mechanics, Scientific Reports 6(1) (2016) 27238.
[102] E.C. Weiss, P. Anastasiadis, G. Pilarczyk, R.M. Lemor, P.V. Zinin, Mechanical Properties of Single Cells by High-Frequency Time-Resolved Acoustic Microscopy, IEEE Transactions on Ultrasonics, Ferroelectrics, and Frequency Control 54(11) (2007) 2257-2271.
[103] F.H.C. Crick, A.F.W. Hughes, The physical properties of cytoplasm: A study by means of the magnetic particle method Part I. Experimental, Experimental Cell Research 1(1) (1950) 37-80.
[104] Y. Zhang, F. Wei, Y.-C. Poh, Q. Jia, J. Chen, J. Chen, J. Luo, W. Yao, W. Zhou, W. Huang, F. Yang, Y. Zhang, N. Wang, Interfacing 3D magnetic twisting cytometry with confocal fluorescence microscopy to image force responses in living cells, Nature Protocols 12(7) (2017) 1437-1450.
[105] J.F. Berret, Local viscoelasticity of living cells measured by rotational magnetic spectroscopy, Nature Communications 7(1) (2016) 10134.

[106] I. De Vlaminck, C. Dekker, Recent advances in magnetic tweezers, Annual review of biophysics 41 (2012) 453-472.
[107] S. Deguchi, T. Ohashi, M. Sato, Tensile properties of single stress fibers isolated from cultured vascular smooth muscle cells, Journal of biomechanics 39(14) (2006) 2603-2610.
[108] N. Desprat, A. Guiroy, A. Asnacios, Microplates-based rheometer for a single living cell, Review of Scientific Instruments 77(5) (2006) 055111.
[109] K. Nagayama, T. Matsumoto, Contribution of actin filaments and microtubules to quasi-in situ tensile properties and internal force balance of cultured smooth muscle cells on a substrate, American Journal of Physiology-Cell Physiology 295(6) (2008) C1569-C1578.
[110] A.D. Stephens, E.J. Banigan, S.A. Adam, R.D. Goldman, J.F. Marko, Chromatin and lamin A determine two different mechanical response regimes of the cell nucleus, Molecular biology of the cell 28(14) (2017) 1984-1996.
[111] N. Desprat, A. Richert, J. Simeon, A. Asnacios, Creep function of a single living cell, Biophysical journal 88(3) (2005) 2224-2233.
[112] C. Alibert, D. Pereira, N. Lardier, S. Etienne-Manneville, B. Goud, A. Asnacios, J.-B. Manneville, Multiscale rheology of glioma cells, Biomaterials 275 (2021) 120903.
[113] T. Fischer, A. Hayn, C.T. Mierke, Effect of nuclear stiffness on cell mechanics and migration of human breast cancer cells, Frontiers in cell and developmental biology 8 (2020) 393.
[114] P.-H. Wu, D.R.-B. Aroush, A. Asnacios, W.-C. Chen, M.E. Dokukin, B.L. Doss, P. Durand-Smet, A. Ekpenyong, J. Guck, N.V. Guz, A comparison of methods to assess cell mechanical properties, Nature methods 15(7) (2018) 491-498.
[115] J.P. Shelby, J. White, K. Ganesan, P.K. Rathod, D.T. Chiu, A microfluidic model for single-cell capillary obstruction by Plasmodium falciparum-infected erythrocytes, Proceedings of the National Academy of Sciences 100(25) (2003) 14618-14622.
[116] M. Lofroth, E. Avci, Development of a novel modular compliant gripper for manipulation of micro objects, Micromachines 10(5) (2019) 313.
[117] H. Xie, X. Meng, H. Zhang, L. Sun, Development of a magnetically driven microgripper for piconewton force-controlled microscale manipulation and characterization, IEEE Transactions on Industrial Electronics 67(3) (2019) 2065-2075.
[118] A. Ichikawa, S. Sakuma, M. Sugita, T. Shoda, T. Tamakoshi, S. Akagi, F. Arai, On-chip enucleation of an oocyte by untethered microrobots, Journal of Micromechanics and Microengineering 24(9) (2014) 095004.
[119] M. Power, A.J. Thompson, S. Anastasova, G.Z. Yang, A monolithic force‐sensitive 3D microgripper fabricated on the tip of an optical fiber using 2‐photon polymerization, Small 14(16) (2018) 1703964.
[120] T. Tanikawa, T. Arai, T. Masuda, Development of micro manipulation system with two-finger micro hand, IEEE, pp. 850-855.
[121] T. Arai, R. Stoughton, Y.M. Jaya, Micro hand module using parallel link mechanism.
[122] T. Tanikawa, M. Kawai, N. Koyachi, T. Arai, T. Ide, S. Kaneko, R. Ohta, T. Hirose, Force control system for autonomous micro-manipulation, IEEE, pp. 610-615.
[123] D. Kawakami, K. Ohara, T. Takubo, Y. Mae, A. Ichikawa, T. Tanikawa, T. Arai, Cell stiffness measurement using two-fingered microhand, IEEE, pp. 1019-1024.
[124] K. Ohara, D. Kawakami, T. Takubo, Y. Mae, T. Tanikawa, A. Honda, T. Arai, Dextrous cell diagnosis using two-fingered microhand with micro force sensor, Journal of Micro-Nano Mechatronics 7(1) (2012) 13-20.
[125] I. Hatta, K. Ohara, T. Arai, Y. Mae, T. Takubo, Automated initial setup method for two-fingered micro hand system, IEEE, pp. 3271-3276.
[126] C.-N. Nguyen, K. Ohara, E. Avci, T. Takubo, Y. Mae, T. Arai, Automated

micromanipulation for a microhand with all-in-focus imaging system, IEEE, pp. 427-432.
[127] C.-N. Nguyen, K. Ohara, E. Avci, T. Takubo, Y. Mae, T. Arai, Real-time precise 3D measurement of micro transparent objects using All-In-Focus imaging system, Journal of Micro-Nano Mechatronics 7(1) (2012) 21-31.
[128] H. Yabugaki, K. Ohara, M. Kojima, Y. Mae, T. Tanikawa, T. Arai, Automated stable grasping with two-fingered microhand using micro force sensor, IEEE, pp. 2771-2776.
[129] N. Khangai, M. Kojima, M. Horade, K. Kamiyama, S. Sakai, Y. Mae, T. Arai, Cell stiffness measurement using two-fingered micro-hand equipped with plate-shaped end effector, IEEE, pp. 517-521.
[130] E. Avci, T. Hattori, K. Kamiyama, M. Kojima, M. Horade, Y. Mae, T. Arai, Piezo-actuated parallel mechanism for biological cell release at high speed, Biomedical Microdevices 17(5) (2015) 98.
[131] E. Kim, M. Kojima, K. Kamiyama, M. Horade, Y. Mae, T. Arai, High-speed active release end-effector motions for precise positioning of adhered micro-objects, World Journal of Engineering and Technology 6(1) (2017) 81-103.
[132] Y. Zhao, Y. Deng, J. Chen, M. Kojima, Q. Huang, T. Arai, X. Liu, High-Speed Cell Assembly with Piezo-Driven Two-Finger Microhand, Applied Sciences 14(2) (2024) 617.
[133] E. Kim, M. Kojima, Y. Mae, T. Arai, High-Speed Manipulation of Microobjects Using an Automated Two-Fingered Microhand for 3D Microassembly, Micromachines, 2020, p. 534.
[134] D. Liu, X. Liu, P. Li, X. Tang, M. Kojima, Q. Huang, T. Arai, Magnetic driven two-finger micro-hand with soft magnetic end-effector for force-controlled stable manipulation in microscale, Micromachines 12(4) (2021) 410.
[135] H. Saijo, M. Kojima, M. Horade, K. Kamiyama, Y. Mae, T. Arai, Development of thermos responsive gel coated end effector for micro manipulation, IEEE, pp. 189-194.
[136] Y. Zhao, X. Liu, R. Wang, D. Liu, M. Kojima, Q. Huang, T. Arai, Automated Assembly by Two-Fingered Microhand for Fabrication of Soft Magnetic Microrobots, IEEE, pp. 13433-13438.
[137] M. Kawakami, M. Kojima, T. Ogura, A. Kubo, T. Arai, S. Sakai, Microhand Platform Equipped with Plate-Shaped End-Effectors Enables Precise Probing of Intracellular Structure Contribution to Whole-Cell Mechanical Properties, Micromachines 16(11) (2025) 1272.
[138] B. Orzechowska, J. Pabijan, J. Wiltowska-Zuber, J. Zemła, M. Lekka, Fibroblasts change spreading capability and mechanical properties in a direct interaction with keratinocytes in conditions mimicking wound healing, Journal of Biomechanics 74 (2018) 134-142.
[139] Q. Luo, D. Kuang, B. Zhang, G. Song, Cell stiffness determined by atomic force microscopy and its correlation with cell motility, Biochimica et Biophysica Acta (BBA) - General Subjects 1860(9) (2016) 1953-1960.
[140] M. Li, L. Peng, Z. Wang, L. Liu, M. Cao, J. Cui, F. Wu, J. Yang, Roles of the cytoskeleton in human diseases, Molecular Biology Reports 50(3) (2023) 2847-2856.
[141] K. Apte, R. Stick, M. Radmacher, Mechanics in human fibroblasts and progeria: Lamin A mutation E145K results in stiffening of nuclei, Journal of Molecular Recognition 30(2) (2017) e2580.
[142] V.L.R.M. Verstraeten, J.Y. Ji, K.S. Cummings, R.T. Lee, J. Lammerding, Increased mechanosensitivity and nuclear stiffness in Hutchinson–Gilford progeria cells: effects of farnesyltransferase inhibitors, Aging Cell 7(3) (2008) 383-393.
[143] P.-H. Wu, D.R.-B. Aroush, A. Asnacios, W.-C. Chen, M.E. Dokukin, B.L. Doss, P. Durand-Smet, A. Ekpenyong, J. Guck, N.V. Guz, P.A. Janmey, J.S.H. Lee, N.M. Moore, A. Ott, Y.-C. Poh, R. Ros, M. Sander, I. Sokolov, J.R. Staunton, N. Wang, G. Whyte, D. Wirtz, A comparison of methods to assess cell mechanical properties, Nature Methods 15(7) (2018) 491-498.
[144] Y. Hao, S. Cheng, Y. Tanaka, Y. Hosokawa, Y. Yalikun, M. Li, Mechanical properties of

single cells: Measurement methods and applications, Biotechnology Advances 45 (2020) 107648.
[145] M. Hu, J. Wang, H. Zhao, S. Dong, J. Cai, Nanostructure and nanomechanics analysis of lymphocyte using AFM: From resting, activated to apoptosis, Journal of Biomechanics 42(10) (2009) 1513-1519.
[146] S.Y. Muhammad, C. Giovanna, M. Alberto, N. Fatou, A. Ladan, N. Joseph, B. Serena, S. Giacinto, C. Dan, Effect of neighboring cells on cell stiffness measured by optical tweezers indentation, Journal of Biomedical Optics 21(5) (2016) 057004.
[147] D. Chang, S. Sakuma, K. Kera, N. Uozumi, F. Arai, Measurement of the mechanical properties of single Synechocystis sp. strain PCC6803 cells in different osmotic concentrations using a robot-integrated microfluidic chip, Lab on a Chip 18(8) (2018) 1241-1249.
[148] M. Hagiwara, T. Kawahara, Y. Yamanishi, T. Masuda, L. Feng, F. Arai, On-chip magnetically actuated robot with ultrasonic vibration for single cell manipulations, Lab on a Chip 11(12) (2011) 2049-2054.
[149] J. Étienne, J. Fouchard, D. Mitrossilis, N. Bufi, P. Durand-Smet, A. Asnacios, Cells as liquid motors: Mechanosensitivity emerges from collective dynamics of actomyosin cortex, Proceedings of the National Academy of Sciences 112(9) (2015) 2740-2745.
[150] T. Arai, R. Stoughton, Y.M. Jaya, Micro hand module using parallel link mechanism, Proceedings of the 1992 Japan-USA Symposium on Flexible Automation, IEEE, 1992.
[151] M. Kawakami, M. Kojima, Y. Masuda, Y. Mae, T. Horii, T. Nagai, M. Nakahata, S. Sakai, T. Arai, Automated Microhand System for Measuring Cell Stiffness By Using Two Plate End-Effectors, IEEE Robotics and Automation Letters 7(2) (2022) 2385-2390.
[152] K. Inoue, T. Tanikawa, T. Arai, Micro-manipulation system with a two-fingered micro-hand and its potential application in bioscience, Journal of Biotechnology 133(2) (2008) 219-224.
[153] J. Chen, J. Irianto, S. Inamdar, P. Pravincumar, D.A. Lee, D.L. Bader, M.M. Knight, Cell Mechanics, Structure, and Function Are Regulated by the Stiffness of the Three-Dimensional Microenvironment, Biophysical Journal 103(6) (2012) 1188-1197.
[154] N. Caille, O. Thoumine, Y. Tardy, J.-J. Meister, Contribution of the nucleus to the mechanical properties of endothelial cells, Journal of Biomechanics 35(2) (2002) 177-187.
[155] M. Li, L. Liu, X. Xiao, N. Xi, Y. Wang, Effects of methotrexate on the viscoelastic properties of single cells probed by atomic force microscopy, Journal of Biological Physics 42(4) (2016) 551-569.
[156] K. Hayashi, M. Iwata, Stiffness of cancer cells measured with an AFM indentation method, Journal of the Mechanical Behavior of Biomedical Materials 49 (2015) 105-111.
[157] S.-y. Saito, M. Hori, H. Ozaki, H. Karaki, Cytochalasin D Inhibits Smooth Muscle Contraction by Directly Inhibiting Contractile Apparatus, Journal of Smooth Muscle Research 32(2) (1996) 51-60.
[158] S.-J. Heo, K.H. Song, S. Thakur, L.M. Miller, X. Cao, A.P. Peredo, B.N. Seiber, F. Qu, T.P. Driscoll, V.B. Shenoy, M. Lakadamyali, J.A. Burdick, R.L. Mauck, Nuclear softening expedites interstitial cell migration in fibrous networks and dense connective tissues, Science Advances 6(25) (2020) eaax5083.
[159] S.-J. Heo, K.H. Song, S. Thakur, L.M. Miller, X. Cao, A.P. Peredo, B.N. Seiber, F. Qu, T.P. Driscoll, V.B. Shenoy, M. Lakadamyali, J.A. Burdick, R.L. Mauck, Nuclear softening expedites interstitial cell migration in fibrous networks and dense connective tissues, Science Advances 6(25) eaax5083.
[160] Y. Kurashina, M. Hirano, C. Imashiro, K. Totani, J. Komotori, K. Takemura, Enzyme-free cell detachment mediated by resonance vibration with temperature modulation, Biotechnology and Bioengineering 114(10) (2017) 2279-2288.
[161] P. Vertegel, P. Milkin, A. Murashko, M. Parker, K. Peranidze, N. Emashova, S. Minko,

V. Reukov, Cell detachment: A review of techniques, challenges, and opportunities for advancing biomedical research and applications, Progress in Biophysics and Molecular Biology 196 (2025) 50-68.
[162] B. Lordon, T. Campion, L. Gibot, G. Gallot, Impact of trypsin on cell cytoplasm during detachment of cells studied by terahertz sensing, Biophysical Journal 123(16) (2024) 2476-2483.
[163] A.E. Rusiñol, M.S. Sinensky, Farnesylated lamins, progeroid syndromes and farnesyl transferase inhibitors, Journal of Cell Science 119(16) (2006) 3265-3272.
[164] H.J. Worman, S. Michaelis, Permanently Farnesylated Prelamin A, Progeria, and Atherosclerosis, Circulation 138(3) (2018) 283-286.
[165] B.E. Danielsson, H.C. Peters, K. Bathula, L.M. Spear, N.A. Noll, K.N. Dahl, D.E. Conway, Progerin-expressing endothelial cells are unable to adapt to shear stress, Biophysical Journal 121(4) (2022) 620-628.
[166] G. Bidault, M. Garcia, J. Capeau, R. Morichon, C. Vigouroux, V. Béréziat, Progerin Expression Induces Inflammation, Oxidative Stress and Senescence in Human Coronary Endothelial Cells, Cells, 2020, p. 1201.
[167] Y. Takahashi, S. Hiratsuka, N. Machida, D. Takahashi, J. Matsushita, P. Hozak, T. Misteli, K. Miyamoto, M. Harata, Impairment of nuclear F-actin formation and its relevance to cellular phenotypes in Hutchinson-Gilford progeria syndrome, Nucleus 11(1) (2020) 250-263.
[168] S. Osmanagic-Myers, A. Kiss, C. Manakanatas, O. Hamza, F. Sedlmayer, P.L. Szabo, I. Fischer, P. Fichtinger, B.K. Podesser, M. Eriksson, R. Foisner, Endothelial progerin expression causes cardiovascular pathology through an impaired mechanoresponse, The Journal of Clinical Investigation 129(2) (2019) 531-545.
[169] I.V.M. Lima, A.V.S. Silva, F.D. Sousa, W.P. Ferreira, R.S. Freire, C.L.N. de Oliveira, J.S. de Sousa, Measuring the viscoelastic relaxation function of cells with a time-dependent interpretation of the Hertz-Sneddon indentation model, Heliyon 10(10) (2024) e30623.
[170] J.R. Lange, C. Metzner, S. Richter, W. Schneider, M. Spermann, T. Kolb, G. Whyte, B. Fabry, Unbiased high-precision cell mechanical measurements with microconstrictions, Biophysical Journal 112(7) (2017) 1472-1480.
[171] M. Veschgini, F. Gebert, N. Khangai, H. Ito, R. Suzuki, T.W. Holstein, Y. Mae, T. Arai, M. Tanaka, Tracking mechanical and morphological dynamics of regenerating Hydra tissue fragments using a two fingered micro-robotic hand, Applied Physics Letters 108(10) (2016).
[172] E. Kim, M. Kojima, L. Xiaoming, T. Hattori, K. Kamiyama, Y. Mae, T. Arai, Analysis of rotational flow generated by circular motion of an end effector for 3D micromanipulation, Robomech Journal 4(1) (2017) 5.
[173] W.D. Phillips, Nobel Lecture: Laser cooling and trapping of neutral atoms, Reviews of Modern Physics 70(3) (1998) 721.
[174] M. Kojima, T. Tanaka, Y. Mae, T. Ogura, T. Arai, Cell stiffness measurement by two-fingered micro-hand system with plate shaped end effector, IEEE, pp. 1-2.
[175] F.H.Y. Chan, F.K. Lam, H. Zhu, Adaptive thresholding by variational method, IEEE Transactions on Image Processing 7(3) (1998) 468-473.
[176] P.J. Burt, E.H. Adelson, The Laplacian pyramid as a compact image code, Readings in computer vision, Elsevier1987, pp. 671-679.
[177] T. Darrell, K. Wohn, Pyramid based depth from focus, IEEE Computer Society, pp. 504-505.
[178] P. Soille, Morphological image analysis: principles and applications, Springer1999.
[179] M. Kawakami, S. Yamahira, M. Kojima, S. Yamaguchi, S. Sakai, Photocontrol of Non-Adherent Cell Adhesion via Azobenzene–PEG–Lipid/Cyclodextrin Host–Guest Interactions, International Journal of Molecular Sciences, 2026, p. 562.
[180] C. De Pascalis, S. Etienne-Manneville, Single and collective cell migration: the

mechanics of adhesions, Molecular biology of the cell 28(14) (2017) 1833-1846.
[181] C.G. Rolli, H. Nakayama, K. Yamaguchi, J.P. Spatz, R. Kemkemer, J. Nakanishi, Switchable adhesive substrates: revealing geometry dependence in collective cell behavior, Biomaterials 33(8) (2012) 2409-2418.
[182] S. Sakakibara, S.A. Abdellatef, S. Yamamoto, M. Kamimura, J. Nakanishi, Photoactivatable surfaces resolve the impact of gravity vector on collective cell migratory characteristics, Science and Technology of Advanced Materials 24(1) (2023) 2206525.
[183] J. Xu, F. Gao, W. Liu, X. Guan, Cell-cell communication characteristics in breast cancer metastasis, Cell Communication and Signaling 22(1) (2024) 55.
[184] M. Lintz, A. Muñoz, C.A. Reinhart-King, The mechanics of single cell and collective migration of tumor cells, Journal of biomechanical engineering 139(2) (2017) 021005.
[185] S. Yamahira, R. Misawa, T. Kosaka, M. Tan, S. Izuta, H. Yamashita, Y. Heike, A. Okamoto, T. Nagamune, S. Yamaguchi, Photoactivatable materials for versatile single-cell patterning based on the photocaging of cell-anchoring moieties through lipid self-assembly, Journal of the American Chemical Society 144(29) (2022) 13154-13162.
[186] Y. Luo, X. Zheng, P. Yuan, X. Ye, L. Ma, Light-induced dynamic RGD pattern for sequential modulation of macrophage phenotypes, Bioactive Materials 6(11) (2021) 4065-4072.
[187] A. Jin, T. Ozawa, K. Tajiri, T. Obata, S. Kondo, K. Kinoshita, S. Kadowaki, K. Takahashi, T. Sugiyama, H. Kishi, A rapid and efficient single-cell manipulation method for screening antigen-specific antibody–secreting cells from human peripheral blood, Nature medicine 15(9) (2009) 1088-1092.
[188] Y. Deng, Y. Guo, B. Xu, Recent development of microfluidic technology for cell trapping in single cell analysis: A review, Processes 8(10) (2020) 1253.
[189] A.M. Ross, Z. Jiang, M. Bastmeyer, J. Lahann, Physical aspects of cell culture substrates: topography, roughness, and elasticity, Small 8(3) (2012) 336-355.
[190] P. Kumar, S. Ebbens, X. Zhao, Inkjet printing of mammalian cells–Theory and applications, Bioprinting 23 (2021) e00157.
[191] D.-L. Versace, G. Moran, M. Belqat, A. Spangenberg, R. Méallet-Renault, S. Abbad-Andaloussi, V. Brezová, J.-P. Malval, Highly virulent bactericidal effects of curcumin-based μ-cages fabricated by two-photon polymerization, ACS Applied Materials & Interfaces 12(4) (2020) 5050-5057.
[192] N. Nagarajan, V. Vyas, B.D. Huey, P. Zorlutuna, Modulation of the contractility of micropatterned myocardial cells with nanoscale forces using atomic force microscopy, Nanobiomedicine 3 (2016) 1849543516675348.
[193] S. Qiu, J. Ji, W. Sun, J. Pei, J. He, Y. Li, J.J. Li, G. Wang, Recent advances in surface manipulation using micro-contact printing for biomedical applications, Smart Materials in Medicine 2 (2021) 65-73.
[194] X. Zhou, H. Wu, H. Wen, B. Zheng, Advances in single-cell printing, Micromachines 13(1) (2022) 80.
[195] V. Cėpla, T. Rakickas, G. Stankevičienė, A. Mazėtytė-Godienė, A.r. Baradokė, Z.i. Ruželė, R.n. Valiokas, Photografting and Patterning of Poly (ethylene glycol) Methacrylate Hydrogel on Glass for Biochip Applications, ACS Applied Materials & Interfaces 12(29) (2020) 32233-32246.
[196] J. Auernheimer, C. Dahmen, U. Hersel, A. Bausch, H. Kessler, Photoswitched cell adhesion on surfaces with RGD peptides, Journal of the American Chemical Society 127(46) (2005) 16107-16110.
[197] L.F. Kadem, K.G. Suana, M. Holz, W. Wang, H. Westerhaus, R. Herges, C. Selhuber‐Unkel, High‐frequency mechanostimulation of cell adhesion, Angewandte Chemie 129(1) (2017) 231-235.

[198] D. Liu, Y. Xie, H. Shao, X. Jiang, Using azobenzene‐embedded self‐assembled monolayers to photochemically control cell adhesion reversibly, Angewandte Chemie International Edition 48(24) (2009) 4406-4408.
[199] Q. Bian, W. Wang, G. Han, Y. Chen, S. Wang, G. Wang, Photoswitched Cell Adhesion on Azobenzene‐Containing Self‐Assembled Films, ChemPhysChem 17(16) (2016) 2503-2508.
[200] D. Wang, W. Zhao, Q. Wei, C. Zhao, Y. Zheng, Photoswitchable Azobenzene/Cyclodextrin Host‐Guest Complexes: From UV‐to Visible/Near‐IR‐Light‐Responsive Systems, ChemPhotoChem 2(5) (2018) 403-415.
[201] J. Zhang, Z.-H. Zhou, L. Li, Y.-L. Luo, F. Xu, Y. Chen, Dual stimuli-responsive supramolecular self-assemblies based on the host–guest interaction between β-cyclodextrin and azobenzene for cellular drug release, Molecular pharmaceutics 17(4) (2020) 1100-1113.
[202] P. Shi, E. Ju, Z. Yan, N. Gao, J. Wang, J. Hou, Y. Zhang, J. Ren, X. Qu, Spatiotemporal control of cell–cell reversible interactions using molecular engineering, Nature communications 7(1) (2016) 13088.
[203] Q. Bian, S. Chen, Y. Xing, D. Yuan, L. Lv, G. Wang, Host-guest self-assembly toward reversible visible-light-responsive switching for bacterial adhesion, Acta Biomaterialia 76 (2018) 39-45.
[204] A.M. Rosales, C.B. Rodell, M.H. Chen, M.G. Morrow, K.S. Anseth, J.A. Burdick, Reversible control of network properties in azobenzene-containing hyaluronic acid-based hydrogels, Bioconjugate chemistry 29(4) (2018) 905-913.
[205] Y.-H. Gong, C. Li, J. Yang, H.-Y. Wang, R.-X. Zhuo, X.-Z. Zhang, Photoresponsive “Smart Template” via host–guest interaction for reversible cell adhesion, Macromolecules 44(19) (2011) 7499-7502.
[206] Q. Bian, W. Wang, S. Wang, G. Wang, Light-triggered specific cancer cell release from cyclodextrin/azobenzene and aptamer-modified substrate, ACS applied materials & interfaces 8(40) (2016) 27360-27367.
[207] K. Maffuid, Y. Cao, Decoding the Complexity of Immune–Cancer Cell Interactions: Empowering the Future of Cancer Immunotherapy, Cancers 15(16) (2023) 4188.
[208] H.-T. Tai, Y.-C. Lin, J.-Y. Ma, C.-T. Lo, Hydrogen Bonding-Induced Assembled Structures and Photoresponsive Behavior of Azobenzene Molecule/Polyethylene Glycol Complexes, Polymers, 2019, p. 1360.
[209] A.M. Rosales, K.M. Mabry, E.M. Nehls, K.S. Anseth, Photoresponsive Elastic Properties of Azobenzene-Containing Poly(ethylene-glycol)-Based Hydrogels, Biomacromolecules 16(3) (2015) 798-806.
[210] S.H. Lee, E. Moroz, B. Castagner, J.-C. Leroux, Activatable Cell Penetrating Peptide–Peptide Nucleic Acid Conjugate via Reduction of Azobenzene PEG Chains, Journal of the American Chemical Society 136(37) (2014) 12868-12871.
[211] S. Yadav, S.R. Deka, G. Verma, A.K. Sharma, P. Kumar, Photoresponsive amphiphilic azobenzene–PEG self-assembles to form supramolecular nanostructures for drug delivery applications, RSC Advances 6(10) (2016) 8103-8117.
[212] K. Kato, K. Umezawa, D.P. Funeriu, M. Miyake, J. Miyake, T. Nagamune, Immobilized culture of nonadherent cells on an oleyl poly (ethylene glycol) ether-modified surface, Biotechniques 35(5) (2003) 1014-1021.
[213] S. Payamifar, A. Poursattar Marjani, A new β-cyclodextrin-based nickel as green and water-soluble supramolecular catalysts for aqueous Suzuki reaction, Scientific Reports 13(1) (2023) 21279.
[214] S. Keiper, J.S. Vyle, Reversible Photocontrol of Deoxyribozyme-Catalyzed RNA

Cleavage under Multiple-Turnover Conditions, Angewandte Chemie International Edition 45(20) (2006) 3306-3309.
[215] F.D. Jochum, P. Theato, Temperature and light sensitive copolymers containing azobenzene moieties prepared via a polymer analogous reaction, Polymer 50(14) (2009) 3079-3085.
[216] A. Harada, M. Kamachi, Complex formation between poly(ethylene glycol) and α-cyclodextrin, Macromolecules 23(10) (1990) 2821-2823.
[217] L. Leclercq, Interactions between cyclodextrins and cellular components: Towards greener medical applications?, Beilstein journal of organic chemistry 12(1) (2016) 2644-2662.
[218] D.S.W. Lee, L.F. Oster, S. Son, D.A. Fletcher, Cell surface crowding is a tunable energetic barrier to cell-cell fusion, Nature Communications 16(1) (2025) 7158.
[219] S. Samanta, A.A. Beharry, O. Sadovski, T.M. McCormick, A. Babalhavaeji, V. Tropepe, G.A. Woolley, Photoswitching Azo Compounds in Vivo with Red Light, Journal of the American Chemical Society 135(26) (2013) 9777-9784.
[220] D. Bléger, J. Schwarz, A.M. Brouwer, S. Hecht, o-Fluoroazobenzenes as Readily Synthesized Photoswitches Offering Nearly Quantitative Two-Way Isomerization with Visible Light, Journal of the American Chemical Society 134(51) (2012) 20597-20600.
[221] Y. Shi, M.A. Gerkman, Q. Qiu, S. Zhang, G.G.D. Han, Sunlight-activated phase change materials for controlled heat storage and triggered release, Journal of Materials Chemistry A 9(15) (2021) 9798-9808.
[222] H. Zhou, J.G. Campos, R. Tennankore, W. Xu, Y. Hu, J. Read de Alaniz, R.C. Hayward, Semicrystalline Poly(azobenzene) with Negative Photochromism for Photochemical Melting of Thick Samples, ACS Macro Letters 14(7) (2025) 910-916.
[223] C. Jeppesen, J.Y. Wong, T.L. Kuhl, J.N. Israelachvili, N. Mullah, S. Zalipsky, C.M. Marques, Impact of polymer tether length on multiple ligand-receptor bond formation, Science 293(5529) (2001) 465-468.
[224] M.M. Yallapu, S.P. Foy, T.K. Jain, V. Labhasetwar, PEG-functionalized magnetic nanoparticles for drug delivery and magnetic resonance imaging applications, Pharmaceutical research 27(11) (2010) 2283-2295.

List of Publications

Papers:

1. **M. Kawakami**, M. Kojima*, Y. Masuda, Y. Mae, T. Horii, T. Nagai, M. Nakahata, S. Sakai and T. Arai, "Automated Microhand System for Measuring Cell Stiffness By Using Two Plate End-Effectors", *IEEE Robotics and Automation Letters*, vol. 7, no. 2, pp. 2385-2390, (2022), DOI: 10.1109/LRA.2022.3143296.
2. **M. Kawakami**, M. Kojima*, T. Ogura, A. Kubo, T. Arai and S. Sakai, “Microhand Platform Equipped with Plate-Shaped End-Effectors Enables Precise Probing of Intracellular Structure Contribution to Whole-Cell Mechanical Properties”, *Micromachines*, vol. 16, no. 11, 1271, (2025), DOI: 10.3390/mi16111272, (Selected as a Feature Paper and Editor's Choice. Featured on the Front Cover of Vol. 16, Issue 11.).
3. **M. Kawakami**, S. Yamahira, M. Kojima*, S. Yamaguchi and S. Sakai, "Photocontrol of Non-Adherent Cell Adhesion via Azobenzene–PEG–Lipid/Cyclodextrin Host–Guest Interactions", *International Journal of Molecular Sciences*, vol. 27, no. 2, 562, (2026), DOI: 10.3390/ijms27020562.

International Conference/Symposium:

4. **M. Kawakami**, M. Kojima, Y. Masuda, Y. Mae, T. Horii, T. Nagai, M. Nakahata, S. Sakai and T. Arai, "Automated Microhand System for Measuring Cell Stiffness By Using Two Plate End-Effectors", *IEEE International Conference on Robotics and Automation (ICRA 2022)*, May 23-27, 2022, Philadelphia, USA.
5. **M. Kawakami**, M. Kojima, I. Horiguchi, T. Ogura, A. Kubo, T. Arai and S. Sakai, "Investigation of pathological diagnostic methods using cell stiffness", *3rd Asian Congress for Alternatives to Animal Experiments (ACAAE 2022)*, Dec. 14-16, 2022, Jeju-do, Republic of Korea.

6. **M. Kawakami**, M. Kojima, S. Yamahira, S. Yamaguchi and S. Sakai, "Reversible Cell Adhesion Control via Host-guest Interactions between AzoBAM and Cyclodextrin", *29th International Conference on Miniaturized Systems for Chemistry and Life Sciences (MicroTAS 2025)*, Nov. 2-6, 2025, Adelaide, Australia.

Domestic Conference/Symposium:

7. **M. Kawakami**, M. Kojima, Y. Mae, T. Horii, T. Nagai, M. Nakahata, S. Sakai and T. Arai, "Improving the Robustness of Stiffness Measurement of Micro-Objects Using Microhand System", *The 22nd SICE System Integration Division Annual Conference (SICE SI2021)*, Dec. 2021, Online, Interactive Presentation.
8. **M. Kawakami**, M. Kojima, A. Kubo, T. Ogura, T. Arai and S. Sakai, "Development of a Micromanipulation System Capable of Applying Large Strain to Individual Cells", *The 47th Annual Meeting of the Molecular Biology Society of Japan (MBSJ2024)*, Dec. 2024, Fukuoka, Japan, Poster Presentation.

Acknowledgments

I would like to thank Prof. Shinji Sakai and Assoc. Prof. Masaru Kojima (Graduate School of Engineering Science, The University of Osaka) for providing the opportunity to conduct this research and for their continuous guidance. I deeply appreciate Prof. Satoshi Yamaguchi and Assist. Prof. Shinya Yamahira (SANKEN, The University of Osaka) for their invaluable advice and insightful discussions, which greatly contributed to this work. I would also like to thank Specially-appointed Assist. Prof. Wildan Mubarok (Graduate School of Engineering Science, The University of Osaka) for his helpful advice on research ideas and academic life, which has been a constant source of support since my undergraduate days.

I would like to extend my sincere appreciation to Prof. Hiroshi Umakoshi (Graduate School of Engineering Science, The University of Osaka) for his valuable advice and constructive comments, which significantly contributed to the improvement of this thesis. I am also deeply indebted to Prof. Shinji Deguchi (Graduate School of Engineering Science, The University of Osaka) for his insightful feedback and stimulating discussions. His inspiring suggestions regarding the future perspectives and potential applications of this research provided invaluable guidance and encouragement.

I wish to express my special appreciation to Dr. Yasuto Todokoro (Graduate School of Science, The University of Osaka). I am particularly grateful for his generous support during the critical revision phase of my paper; he kindly prioritized my urgent ITC measurements by flexibly adjusting the facility schedule and provided valuable technical consultation.

I am grateful to Assist. Prof. Masaki Nakahata (Graduate School of Science, The University of Osaka), Assoc. Prof. Ikki Horiguchi (Graduate School of Engineering Science, Akita University), Ms. Masako Karita, and Ms. Mariko Shibukawa for their extensive support in laboratory management, including supply ordering and budget execution, which ensured a smooth research environment.

I also thank all the members of the Sakai Laboratory for their daily support and for providing a positive and stimulating environment.

I acknowledge the financial support provided by the JST SPRING (Grant Number [JPMJSP2138]) and the JSPS Research Fellowships for Young Scientists (Grant Number [24KJ1609]).

Finally, special thanks are due to Assist. Prof. Ryotaro Kazama (Graduate School of Engineering, Tokyo University of Science). As a colleague and close friend from our master's course through to my doctoral studies, his presence and support were a constant source of motivation, always pushing me to reach higher goals.